

Role of electron-phonon scattering in the relaxation of hot carriers at surfaces

Der Fakultät für Physik,

der

Universität Duisburg-Essen

zur Erlangung des akademischen Grades

eines

Doktors der Naturwissenschaften

(Dr.rer.nat.)

vorgelegte Dissertation

von

Maedeh Zahedifar

aus

Isfahan, Iran

Die vorliegende Arbeit wurde im Zeitraum von May 2015 bis Januar 2019 in der Fakultät für Physik der Universität Duisburg-Essen unter der Leitung von Prof. Dr. rer. net. Peter Kratzer in seiner Arbeitsgruppe angefertigt.

Referent: Prof. Dr. Peter Kratzer
Korreferent: Prof. Dr. Wolf Gero Schmidt
Korreferent: Prof. Dr. Rossitza Pentcheva
Chairmann: apl. Prof. Dr. Hermann Nienhaus

Datum der mündlichen Prüfung 20 May 2019

Erklärung zur Dissertation

Hiermit erkläre ich diese Arbeit selbstständig angefertigt und keine anderen Hilfsmittel und Quellen verwendet zu haben, als die angegebenen. Weiterhin habe ich alle wörtlich oder inhaltlich übernommenen Stellen als solche gekennzeichnet.

Diese Dissertation wurde nur in diesem Promotionsverfahren eingereicht.

Nach §1 Satz 2 der Promotionsordnung der Universität Duisburg-Essen vom 19. Januar 2015 wird **Dr.rer.nat.** als Doktorgrad angestrebt.

Duisburg, January 2019.

Acknowledgements

The research which yielded the results presented in this thesis was carried out at collaborative research centre 1242 (CRC1242) located at the Faculty of Physics in the University of Duisburg-Essen.

At the end of my thesis I would like to thank those people who made this thesis possible. First of all I wish to express my sincere gratitude to Prof. Dr. Peter Kratzer who gave me the chance to work in his group at University of Duisburg-Essen. I would like to thank him for his continuous support, for giving me self-confidence, and the chance to participate in conferences and workshops. I would like to thank him for his courtesy and tolerance for teaching me the way of scientific thinking, for giving me a deep understanding of science, and for guiding this thesis in the correct way.

I would also like to thank Dr. Nora Dörmann and my colleagues and friends Joscha Hekele and PD Dr. Daniel Waltner for their nice and warm help.

My special thanks go to my dear friend Kavimani Ramanujam for his support.

Finally, I would like to express my full gratitude to God and my parents and my sisters; Maryam and Marzieh.

Abstract

On semiconductor substrates, the states induced inside the band gap by an adsorbate layer or by an ultra-thin deposited metal film may host rather long-lived (hundreds of femtoseconds) excitations, but detailed knowledge of their atomic and electronic structure is required to analyze the processes governing their relaxation.

Moreover, ultrafast pump-probe laser spectroscopy experiments have made it possible to explore the state-specific relaxation dynamics of hot carriers at surfaces and interfaces. Our goal is to provide a system-specific theoretical analysis of these data.

As one example, quantum well states (QWS) in thin Pb films offer a suitable probing ground for studying the competition between the relaxation mechanisms of electron-electron and electron-phonon scattering. By comparing *ab initio* theoretical results of the vibrational modes of the $\sqrt{3} \times \sqrt{3}$ reconstructed SIC phase of Pb on Si(111) to experimental Raman data we find that this reconstruction is a good starting point for investigation of multilayer Pb films on Si(111).

We performed first-principles density-functional (DFT) calculations addressing the electronic band structure of few-atomic-layer Pb films on Si(111). In addition, phonon spectra and matrix elements for electron-phonon coupling within deformation potential theory were obtained from the DFT calculations. This enables us to calculate state-specific rate constants for the electron-phonon scattering in particular QWS. The contribution of electronic processes (impact ionization) to the lifetime can be estimated from the imaginary part of the electronic self-energy calculated in the GW approximation. Moreover, by numerically solving the rate equations for the occupation numbers in a prototypical electronic band structure coupled to a phononic heat bath, we are able to follow the dissipation of the electronic excitation energy to the Pb lattice vibrations over long time. The time scales extracted from the simulations are compared to the experimental data from time-resolved pump-probe experiments.

In contrast to relaxation in metallic bands, some surface preparations give rise to an insulating surface with Mott-Hubbard bands inside the substrate band gap. For one such system, an adsorbate layer of Sn on Si(111) with coverage of 1/3, we calculated both the electronic and phononic band structures. The strongly correlated electronic ground state is approximated within our DFT approach by an antiferromagnetic state treated with the HSE hybrid functional. Again, the deformation potentials for electron-phonon scattering have been obtained from our calculations. Since the Mott-Hubbard gap is found to be much larger than typical phononic quanta, the relaxation of hot carriers into the ground state is possible only by a multi-phonon process. This gives rise to a very long lifetime of the excitations which we estimate from our calculations.

Zusammenfassung

In Halbleitersubstraten können Zustände, die durch eine Adsorbatlage oder einen ultradünnen aufgewachsenen Metallfilm in der Bandlücke erzeugt werden, tendenziell zu langlebigen (im Bereich hunderter Femtosekunden) Anregungen führen, jedoch ist detaillierte Kenntnis der atomaren und elektronischen Struktur notwendig, um die Relaxationsmechanismen dieser Anregungen zu analysieren.

Ultraschnelle Pump-Probe Laserspektroskopie-Experimente machen es möglich, die zustands-spezifischen Relaxationsdynamiken heißer Ladungsträger auf Ober- oder Grenzflächen zu charakterisieren. Es ist unsere Zielsetzung, eine systemspezifische theoretische Analyse dieser Daten zu liefern.

Als erstes Beispiel stellen Quantentopf-Zustände in dünnen Pb-Filmen eine passende Basis zur Analyse der konkurrierenden Relaxationsmechanismen der Elektron-Elektron- und der Elektron-Phonon-Streuung dar. Durch den Vergleich theoretischer Ab initio-Resultate der Vibrationsmoden der $\sqrt{3} \times \sqrt{3}$ -rekonstruierten SIC Phase von Pb auf Si(111) mit experimentellen Raman-Spektroskopie-Daten konnten wir herausfinden, dass diese Rekonstruktion ein guter Startpunkt für die Untersuchung von mehrlagigen Pb-Filmen auf Si(111) ist.

Wir führten Ab initio-Dichtefunktionaltheorie-Rechnungen (DFT) durch, um die elektronische Bandstruktur von Pb-Filmen kleiner Lagenanzahl auf Si(111) zu erhalten. Zusätzlich konnten durch diese Rechnungen Phononenspektren und Matrixelemente der Elektron-Phonon-Wechselwirkung im Rahmen der Deformationpotential-Theorie erhalten werden.

Dies ermöglichte es uns, zustandsspezifische Ratenkonstanten der Elektron-Phonon-Streuung in ausgewählten Quantentopf-Zuständen zu berechnen. Der Beitrag elektronischer Prozesse zur Lebensdauer konnte durch den Imaginärteil der Selbstenergie, die mittels der GW-Approximation berechnet wurde, abgeschätzt werden. Durch die numerische Lösung der Ratengleichungen für die Besetzungszahlen in einer prototypischen elektronischen Bandstruktur, die an ein phononisches Wärmebad gekoppelt ist, waren wir zudem in der Lage, die Dissipation elektronischer Anregungen in Pb-Gitterschwingungen über einen langen Zeitraum zu verfolgen. Die Zeitskalen unserer Simulationen wurden mit experimentellen Daten aus zeitaufgelösten Pump-Probe-Experimenten verglichen.

Im Gegensatz zur Relaxation in metallischen Bändern rufen manche Oberflächenpräparationen eine nichtleitende Oberfläche mit Mott-Hubbard-Bändern in der Bandlücke des Substrats hervor. Für eines dieser Systeme, eine Adsorbatlage von Sn auf Si(111) mit einer Bedeckung von $1/3$ Monolagen, berechneten wir sowohl die elektronischen als auch die phononischen Bandstrukturen. Der stark korrelierte elektronische Grundzustand wurde innerhalb unseres DFT-Ansatzes durch einen antiferromagnetischen Zustand approximiert, wobei wir das HSE-Hybridfunktional verwendeten. Auch hier haben wir die Deformationspotentiale der Elektron-Phonon-Streuung durch unsere Rechnungen erhalten. Da die Mott-Hubbard-Bandlücke sich als viel größer herausstellte im Vergleich zu typischen phononischen Quanten, wird die Relaxation heißer Ladungsträger in den Grundzustand nur durch einen Multi-Phonon-Prozess ermöglicht. Dies lässt auf sehr lange Lebensdauern der Anregungen schließen, welche wir durch unsere Rechnungen charakterisierten.

1 Introduction

1.1 Motivation

Modifying the physical properties of condensed matter by external control parameters allow manifold technological applications which have become essential in our daily life. Our understanding of these properties, applications and developments is based on thermodynamics and the derived concepts. In many cases on a microscopic level of the properties, variations correspond to a non-equilibrium situation with complex theoretical treatment which generally requires some concepts beyond thermodynamics. Hence, a thorough understanding about the temporal evolution of non-equilibrium conditions promises innovative impetus and novel concepts for science and applications.

Non-equilibrium situations can be prepared in condensed matter through sufficiently short-timed external stimuli, e. g. light flashes, impulsive pressure change, voltage surge, or particles impact. The strongly excited electronic and phononic degrees of freedom are associated with dynamics in time and space i.e., on characteristic time and length scales in the femtosecond and nanometer range, respectively. Experimental access to such dynamics succeeds specifically in the domain of time. The paramount goal is to develop a general, microscopic understanding of non-equilibrium states and the respective dynamics.

Nowadays exploring the state-specific relaxation dynamic of hot carriers at metals surface and metal interface is an important topic not only as a fundamental point but also regarding technological applications. In the scale of nano and confined systems, in particular, the interaction of hot carriers (like electrons and phonons) and the effect of electron-phonon coupling (EPC), are important for the photovoltaic and nanoscale electronic devices as far as their efficiency due to waste heat generation is considered. One of the most significant technical challenges is the quantum size effects (QSEs) from the confinement and interference of electrons in nanostructures and in various genuine physical properties of these nanomaterials[38, 133] (an example is graphene, that attracts a lot of attention due to reducing the probability for scattering event[81]). In bilayer graphene, extremely low electron-phonon scattering rates are discovered, which sets the fundamental limit on possible charge-carrier mobilities at room temperature. In the last decades, EPC has been studied, both theoretically and experimentally, through a variety of methods. From the experimental standpoint, the availability of pulsed coherent laser light with an fs-period and high intensity at a so-far-unreachable frequency range (THz) has opened new avenues for analysis. Although the technical developments in the past decades were mostly based on photo emission spectroscopy (PES), two-photon photo emission (2PPE) (Fig.(1.1)), time-resolved 2PPE (TR-2PPE) and angular-resolved 2PPE are employed to study the metal surface and the interface of electronic excitation. However, new theoretical approaches are also required to describe the physical properties because both the electronic and optical properties bring about a new regime of description. To experimentally understand photo-induced carrier dynamics in thin (semi-)metal films and in strongly correlated adsorbate systems, two complementary experimental geometries are used in femtosecond time- and angle-resolved linear and non-linear

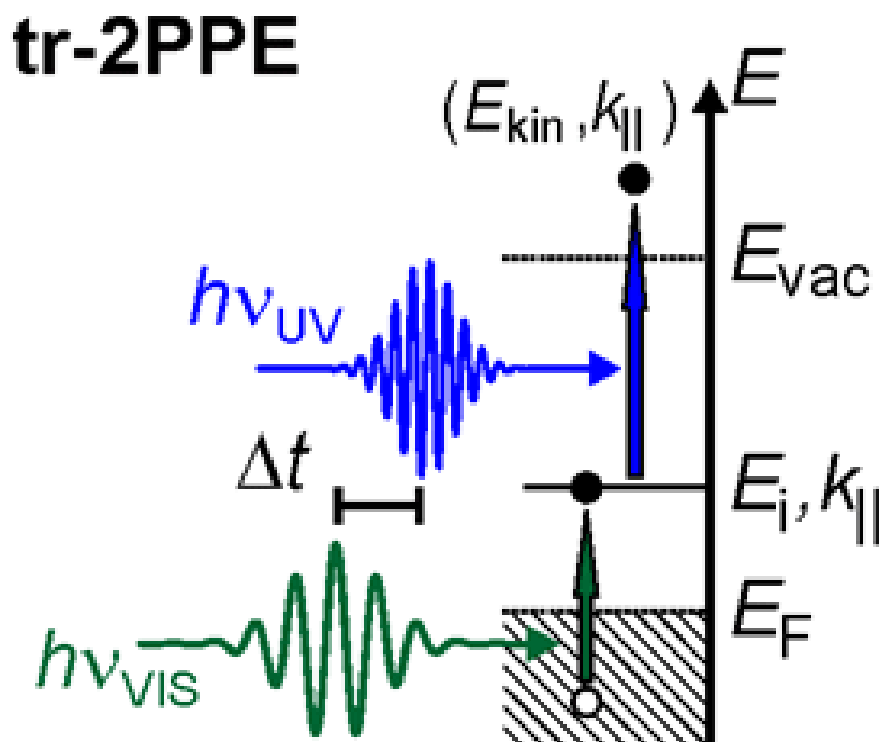


Figure 1.1: Scheme of two photon photoelectron spectroscopy (2PPE). Emission of a photoelectron requires two photons which each have a photon energy below the work function. Thereby unoccupied electronic states can be probed as an intermediate state in the 2PPE process (right panel). If the two laser pulses are delayed in time, a pump-probe experiment is performed and the population dynamics of the probed state are monitored at a well defined energy and momentum parallel to the surface [61].

photo emission to prepare the situation for them to separate local and non-local relaxation processes of primary and secondary excited carriers.

From the theoretical perspective, a great improvement is achieved because of the increased computer power, which allows calculating increasingly complex systems with more and more parameters.

1.2 Aim of this work

The aim is to provide a system-specific theoretical analysis to provide grounds for exploring the state-specific relaxation dynamics of hot carriers at surfaces and interfaces and applying computational methods for material-specific simulations of electronic excitation and relaxation.

We have studied metal layers (Pb) and atoms (Sn) on Si (111) surface within density functional theory using the Vienna Ab initio Simulation Package (VASP) computer program for the electronic structure calculations and phonon dispersion from first principles. The detailed features of the method and computer package which is used in this thesis are described

CHAPTER2 and **CHAPTER3**, which is mostly about the theory of electron-phonon coupling formalism from theory point of view.

In the **CHAPTER4**, the result of Raman spectroscopy for Pb:Si(111) surface and the theoretical study of the vibrational modes of the $(\sqrt{3} \times \sqrt{3})$ reconstructed SIC phase of Pb on Si(111) will be presented and their relation with the atomic surface structure will be discussed. The Raman response of the surface localized vibrational modes, in particular, is identified in the low-frequency spectral range (down to 15cm^{-1}).

In **CHAPTER5**, which is the main part of my thesis, the necessary input data is provided by simulating electronic structure, calculating phonon dispersion and density matrix dynamics required for a theoretical description for pump-probe laser spectroscopy for the QWSs of the Pb on the Si(111), while the Quantum-well states (QWSs) have widely been the focus of academic interest due to the technological impact of the new techniques, access to new investigation techniques in the recent years.

I studied the role of electron-phonon scattering in the relaxation of hot carriers at quantum well states (QWSs) in thin Pb films. Electron-phonon coupling (EPC) has attracted much attention in condensed matter physics; it is also so important regarding thin metallic films on semiconductor substrates because they lend themselves to the study of quantum size effects in metals. In this thesis, it is attempted to develop a sound basis for investigating electronic relaxation processes in atomically thin Pb layers through working with the $\sqrt{3} \times \sqrt{3}$ model for film thicknesses within 3 and 6 ML.

Density functional theory calculations are employed to obtain both the electronic and the phononic two-dimensional band structure of these films. Subsequently, the strength of the electron-phonon coupling is investigated for some representative (either occupied or unoccupied) quantum well states in the four-layer and five-layer Pb films; especially the electrons away from the Fermi energy must also be taken into account. Therefore, the calculations offered in this thesis are required.

The results are compared with the experimental data of the energetic position, dispersion and lifetime broadening of quantum well states in **CHAPTER5**. From the theoretical standpoint, the contribution of the electron-phonon scattering at these relatively slow decay processes was investigated. The main limitation of the theoretical approach is simply the fact that so far only freestanding Pb layers could be modeled. In this thesis, the influence of the silicon substrate is taken into consideration both on the complex crystallographic structure ($(\sqrt{3} \times \sqrt{3})$ R30-reconstruction) and the electronic structure of the Pb layers.

In addition, optical phonons were needed to determine the electron-phonon coupling in the quantum well states that are farther away (above) the Fermi energy. The "frozen-phonon" approach is applied, as described in [129]. The method is characterized by changes in the atomic geometry of the system according to the eigenmode i of a given phonon to Δu_i . Due to the Deformations potential theorem [95], the electron-phonon coupling can be determined from the matrix element. The process is particularly suitable for optical deformation potentials, since their matrix elements are independent of \mathbf{q} to a good approximation. Then this gives:

$$D_{nk,iq}^{n'\mathbf{k}+\mathbf{q}} \approx D_{n,i} \langle \Psi_{n',\mathbf{k}+\mathbf{q}} | e^{i\mathbf{q}\cdot\mathbf{r}} | \Psi_{n,\mathbf{k}} \rangle \quad (1.1)$$

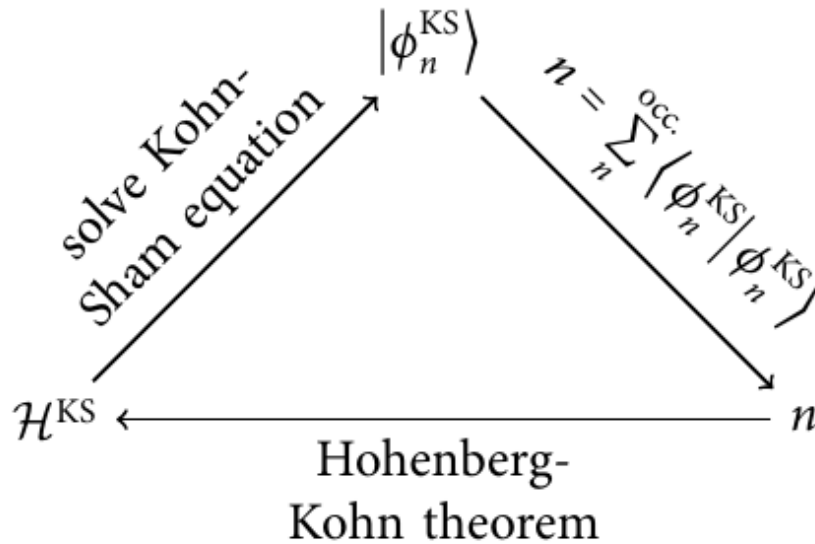
where $D_{n,i}$ is given by:

$$D_{n,i} = \frac{\Delta E_n}{\Delta u_i} \quad (1.2)$$

The application of the procedure described above is provided for multi-layered quantum well layers with Pb-states, as well as the Sn-adsorbed layer with cover 1/3. The extracted values of the state-resolved electron-phonon coupling are incorporated in the model Hamiltonian. In **CHAPTER6** a particular option i.e., Sn on semiconductor substrates, is investigated. The often-long-lived states inside the band gap induced by an adsorbate layer or an ultra-thin deposited metal film may host rather long-lived excitations (hundreds of femtoseconds). However detailed knowledge about their atomic and electronic structure is required to analyze the processes governing their relaxation. Sn/Si(111)-($\sqrt{3} \times \sqrt{3}$) was offered as a model system to investigate correlation effects encouraged by several studies that have reported phase transitions to distorted and/or insulating ground states in related surfaces as, e.g., in Pb/Ge(111)-($\sqrt{3} \times \sqrt{3}$) [18], specifically, the correlations that were reported to be responsible for the formation of a Mott insulating ground state in Sn/Si(111)-($\sqrt{3} \times \sqrt{3}$) [79, 91]. However, a question is left unanswered about how to connect the abrupt transition from metallic to insulating behavior to a Mott-Hubbard type metal-to-insulator transition (MIT), where one would expect a rather gradual loss of spectral weight at the Fermi level for decreasing temperatures. Moreover, another concern which remains unclear is whether the potential Mott-Hubbard ground state also involves a magnetic order, since the spin frustration is a fundamental complication here. Experiments using scanning tunneling spectroscopy (STS) indicate that the Si(111):Sn ($\sqrt{3} \times \sqrt{3}$) system undergoes a metal-to-insulator transition below ~ 30 K. Below this temperature, the pseudo-gap near the Fermi energy develops into a sharp gap whose width is reported to be 30 meV [79] or 35 meV according to more recent measurements [85]. A strongly correlated system, Sn adatoms on Si(111), which is in contrast to relaxation in metallic bands, were studied in **CHAPTER6** to give rise an insulating surface with Mott-Hubbard bands inside the substrate band gap. Both the electronic and phononic band structures are calculated here. The strongly correlated electronic ground state is approximated within our DFT approach by an antiferromagnetic state treated with the HSE hybrid functional. Again, the deformation potentials for electron-phonon scattering have been obtained from my calculations. Since the Mott-Hubbard gap is found to be much larger than typical phononic quanta, the relaxation of hot carriers into the ground state is possible only by a multi-phonon process which gives rise to a very long lifetime of the excitations estimated by the calculations in this thesis.

Finally in **CHAPTER7** the overall conclusion which covers all my results for Raman spectroscopy (chapter 4), Pb:Si (chapter 5) and the Sn on Si(111), (chapter 6) is presented.

2 Theory



2.1 Density functional theory

2.1.1 The many-body problem

Density functional theory methods form the basis of a diversified and very dynamic area of present-day computational physics including atomic, molecular, solid state and even nuclear physics. In the 20th centuries (Thomas-Fermi and Hohenberg-Kohn theory, respectively), density functional concepts became subjects of mathematical physics. In 1994, a number of activities took place to celebrate the thirtieth anniversary of Hohenberg-Kohn-Sham theory.

In this study, Density functional theory (DFT) is employed which is the most widely applied method in theoretical material design due to its high predictive power. Conceptually, DFT reduces the complexity of a system with N electrons from the $3N$ -dimensional wave function to the 3-dimensional electron density. The Hohenberg-Kohn theorem proves that this mapping is exact. However, in practice, the part of the total-energy originating from the exchange and the correlation of electrons is too complex to be calculated for any material with more than a few electrons. Thus, Kohn and Sham introduced a fictitious non-interacting system in which all many-body effects are subsumed in the exchange-correlation functional.

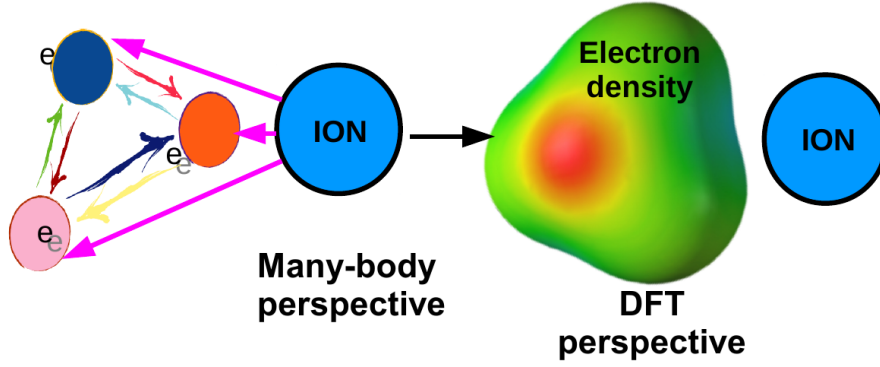


Figure 2.1: Illustration for the main idea of density-functional theory to describe the individual mutual interactions of the electrons and their interaction with ions with that of an electron ensemble represented only by its density.

2.1.2 Thomas-Fermi-Dirac Theory

In this theory which was independently studied by Thomas [117] and Fermi, the exchange energy and electron correlations are neglected, and the uniform density n is replaced by an inhomogeneous one $n(\mathbf{r})$. Hence, the total energy of a non-interacting, inhomogeneous and non-spin-polarized electron gas in the ground state in the Thomas-Fermi theory is given by:

$$E_{TF}[n, V_n] = C_F \frac{\hbar^2}{m} \int d^3\mathbf{r} n^{5/3}(\mathbf{r}) + \int d^3\mathbf{r} V_n(\mathbf{r}) n(\mathbf{r}) + \frac{1}{2} \int d^3\mathbf{r} \int d^3\mathbf{r}' v(\mathbf{r}-\mathbf{r}') n(\mathbf{r}) n(\mathbf{r}') \quad (2.1)$$

Where $\int d^3\mathbf{r}' v(\mathbf{r}-\mathbf{r}') n(\mathbf{r}')$ and $\int d^3\mathbf{r} V_n(\mathbf{r}) n(\mathbf{r})$ are Hartree potential and the potential energy in the field of the nuclei, respectively. The Thomas-Fermi model (TF) assumes that electrons are distributed uniformly in phase space, with two electrons in every h^3 of volume. Now, for each position space volume element $d^3(\mathbf{r})$, we fill out a sphere of momentum space to the Fermi momentum p_f :

$$\frac{4}{3}\pi p_f^3(\mathbf{r}) \quad (2.2)$$

As the number of electrons must be the same in both position space and momentum space, we find for the electron density $n(\mathbf{r})$:

$$n(\mathbf{r}) = \frac{8\pi}{3h^3} p_f^3(\mathbf{r}) \quad (2.3)$$

Solving for p_f and using this to calculate the classical kinetic energy, we now get a relation of the kinetic energy as a function of the electron density:

$$T_{TF}[n(\mathbf{r})] = C_F \int n^{5/3}(\mathbf{r}) d^3(\mathbf{r}) \quad (2.4)$$

where, now in atomic units,

$$C_F = \frac{3}{10} (3\pi^2)^{2/3} \quad (2.5)$$

Considering the exchange contribution as local exchange per electron by Dirac [29] the total energy of the electronic system improved, $E_{TFD}[n, V_n]$.

$$E_{TFD}[n, V_n] = E_{TF}[n, V_n] - C_D \frac{e^2}{4\pi\epsilon_0} \int d^3\mathbf{r} n^{4/3}(\mathbf{r}) \quad (2.6)$$

TF theory was, thus, the first official density functional theory (DFT). However, it had major drawbacks, as the exchange energy and electron correlation was totally neglected, resulting in a large error in the kinetic energy term. It was also proven that TF theory could not describe molecular bonding. Hence, the correlation between the electrons is neglected in this description and it needs to be improved through another theory which will be explained in the following.

2.1.3 The Hohenberg-Kohn theorem

Basis

As mentioned above, in the Thomas-Fermi-Dirac approach, the correlation between the electrons is fully neglected. One step further is Hohenberg-Kohn (HK) theory [50] which, at least for the ground states, is an exact theory for many-body systems. The Hohenberg-Kohn theorems relate to any system consisting of electrons moving under the influence of an external potential $V_{\text{ext}}(\mathbf{r})$. Stated simply, they are as follows: Theorem I (HK(I)) and Theorem II (HK(II)). Defining mappings C and D such that :

$$\begin{aligned} C : V_{\text{ext}} &\longrightarrow \Psi_0 \\ D : \Psi_0 &\longrightarrow n \end{aligned}$$

via Schrödinger equation : $(H_0|\Psi_0\rangle = E|\Psi_0\rangle)$ guarantees the HK theorem;

- Theorem I : For any system of interacting particles in an external potential $V_{\text{ext}}(\mathbf{r})$, the potential $V_{\text{ext}}(\mathbf{r})$ is determined uniquely, except for a constant by the ground state density $n_0(\mathbf{r})$:
HK(I) $\longrightarrow (C.D)^{-1} = D^{-1}.C^{-1}$ (as shown in the Fig. (2.2) schematically).
- Theorem II : A universal functional for the energy $E[n]$ in terms of the density $n(\mathbf{r})$ can be defined which is valid for any external potential $V_{\text{ext}}(\mathbf{r})$. The exact ground state energy of the system is the global minimum of this functional, and the density minimizing the functional is the exact ground state density $n_0(\mathbf{r})$.

In other words, HK(I) indicates that the external potential is a unique functional of electron density in the ground state; therefore, the total energy is also a functional of the ground state electron density. A consequence (an aftermath) of the first Hohenberg-Kohn theorem is that all system properties are only determined through the ground state electron density. In HK(I), the total energy of a system, which is a function of the ground state electron density through the first theorem, is minimized for the correct ground state energy. Hohenberg and Kohn defined a universal function, F_{HK} containing the function for the kinetic energy and that of the electron-electron interaction, \hat{W}_{ee} , which is valid for any system of electrons.

$$F_{HK}[n] = \langle \Psi[n] | \hat{T} + \hat{W}_{ee} | \Psi[n] \rangle, \quad (2.7)$$

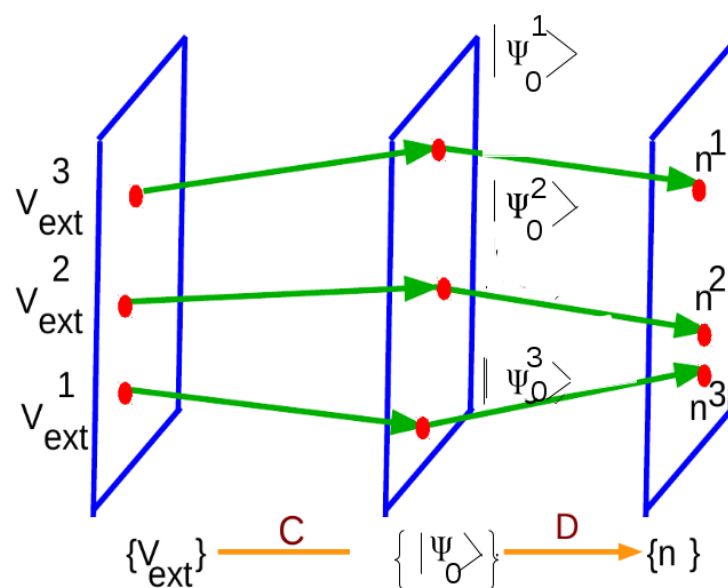


Figure 2.2: Schematic illustration of the Hohenberg-Kohn maps C and D . $V_{\text{ext}}(\mathbf{r})$ is the external potential, and the index 1, 2 and 3 are schematic of atom 1, 2 and 3. Ψ_0 is the ground state wave function and n is density.

which can be used to define the total electronic energy functional

$$E[n] = F_{HK}[n] + \int V_{\text{ext}}(r)n(\mathbf{r})d\mathbf{r} \quad (2.8)$$

$$E_0 = \min_n \left\{ F_{HK}[n] + \int V_{\text{ext}}(\mathbf{r})n(\mathbf{r})d\mathbf{r} \right\} \quad (2.9)$$

$F_{HK}[n]$ can, therefore, be calculated (in principle but not in practice) for all ground state densities $n(\mathbf{r})$ which is the most important (significant) conclusion of the HK-theorem. Once approximations for $F_{HK}[n]$ are known, they/it can be applied to all electronic systems ranging from atoms and molecules to solids. It is worth noting that, for degenerate ground states, $\Psi[n]$ is not unique but stands for any degenerate ground-state wave function. However, all $\Psi[n]$ give the same $F_{HK}[n]$, which is thus a unique functional of n . Hohenberg and Kohn further showed that the density functional $E[n]$ satisfies a variational property: the ground-state energy E_0 of the system considered is obtained by minimizing this functional with respect to N -electron densities n that are ground-state densities associated with some local potential (referred to as v -representable densities).

2.1.4 The Kohn-Sham scheme

The kinetic energy has a large contribution to the total energy. Therefore even the 1 % error in the kinetic energy of the Thomas-Fermi-Weizsäcker model prevented DFT from being used as a quantitative predictive tool. Thus DFT was largely ignored until 1965 when Kohn and Sham introduced a method which treated the majority of the kinetic energy exactly. In 1965 the accurate approximations for the functional $F_{HK}[n]$ have been obtained by means of the Kohn-Sham method [62]. The theory begins by considering the noninteracting reference system: N noninteracting electrons moving in external potential $V_{KS}(\mathbf{r})$, each in one of N orbitals, $\phi_i(\mathbf{r})$. Such a system will be defined by the Hamiltonian (Eq. 2.10) :

$$\hat{H}_{KS} = \hat{T}_{KS} + \hat{V}_{KS}(\mathbf{r}) \quad (2.10)$$

Where an effective potential $V_{KS}(\mathbf{r})$ and KS kinetic energy are given by:

$$V_{KS}(\mathbf{r}) = V_{ext}(\mathbf{r}) + V_H(\mathbf{r}) + V_{XC}(\mathbf{r}) \quad (2.11)$$

$$T_{KS}[n] = - \sum_{i=1}^{N/2} \int d^3\mathbf{r} \phi_i^*(\mathbf{r}) \nabla^2 \phi_i(\mathbf{r}) \quad (2.12)$$

which has an exact eigenfunction that is the single determinant constructed from the N lowest eigenstates of the one-electron equations:

$$\left[\frac{-1}{2} \nabla^2 + \hat{V}_{KS}(\mathbf{r}) \right] \phi_i(\mathbf{r}) = \varepsilon_i \phi_i(\mathbf{r}) \quad (2.13)$$

It is required that the ground state density be stationary. (In calculus of variations, the Euler-Lagrange equation, or Lagrange's equation, is a differential equation whose solutions are the functions for which a given functional is stationary.) The corresponding Euler-Lagrange equation is

$$\mu = \hat{V}_{KS}(\mathbf{r}) + \frac{\delta T_{KS}[n]}{\delta n(\mathbf{r})} \quad (2.14)$$

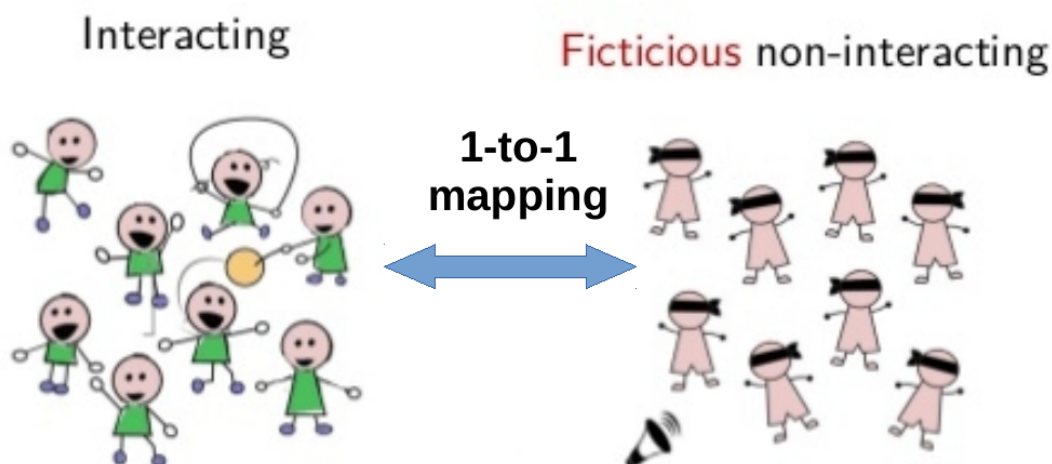


Figure 2.3: Schematically non-interacting KS electrons living in an external potential such that their density is the same as the fully-interacting density.

where the Lagrange multiplier, a familiar property to chemists, the chemical potential μ , has been introduced. In this system the total energy and electron density are given by:

$$E[n] = T_{KS}[n] + \int V_{KS}(\mathbf{r})n(\mathbf{r})d(\mathbf{r}) \quad (2.15)$$

and

$$n(\mathbf{r}) = 2 \sum_{i=1}^{N/2} |\phi_i(\mathbf{r})|^2 \quad (2.16)$$

The quantity $T_{KS}[n]$ is well-defined, but not equal to the exact kinetic energy, $T[n]$. Kohn and Sham reformulated the interacting problem so that its kinetic component is defined to be $T_{KS}[n]$ to give

$$E[n] = T_{KS}[n] + J[n] + \int V_{KS}(\mathbf{r})n(\mathbf{r})d(\mathbf{r}) + E_{XC}[n] \quad (2.17)$$

where $J[n]$ is the Coulombic integral expressed in terms of electron density and $E_{XC}[n]$ is the exchange-correlation energy. The Euler-Lagrange equation now becomes:

$$\mu = V_{\text{eff}}(\mathbf{r}) + \frac{\delta T_{KS}[n]}{\delta n(\mathbf{r})} \quad (2.18)$$

where the Kohn-Sham (KS) effective potential, $V_{\text{eff}}(\mathbf{r})$ is defined as:

$$V_{\text{eff}}(\mathbf{r}) = V_{\text{ext}}(\mathbf{r}) + \int \frac{n(\mathbf{r}')}{|\mathbf{r} - \mathbf{r}'|} d(\mathbf{r}') + V_{xc}(\mathbf{r}) \quad (2.19)$$

and the exchange-correlation potential, $V_{xc}(\mathbf{r})$ is

$$V_{xc}(\mathbf{r}) = \frac{\delta E_{xc}[n]}{\delta n(\mathbf{r})} \quad (2.20)$$

Kohn and Sham noticed that the Eq. 2.21 is the same as Eq. 2.13 by using the effective potential $V_{\text{eff}}(\mathbf{r})$ instead of V_{KS} . Thus, the exact density can be obtained by solving the N one-electron equations (the restricted KS equations)

$$\left[-\frac{1}{2}\nabla^2 + V_{\text{eff}}(\mathbf{r})\right]\phi_i(\mathbf{r}) = \epsilon_i\phi_i(\mathbf{r}) \quad (2.21)$$

Notice that V_{eff} depends on $n(\mathbf{r})$, via equation (2.19), hence the KS equations must be solved iteratively. The KS equations are very similar to the Hartree-Fock equations. In fact, setting the exchange-correlation potential to the HF exchange potential yields the HF equations. Drawing too many similarities to HF is dangerous, however. Firstly, the KS orbitals are simply a way of representing the density; they are not (as in HF) an approximation of the wavefunction. Also, HF theory is variational, providing an upper bound to the exact energy, yet DFT is only variational if the exact energy functional is used. The above analysis is only appropriate for closed shell molecules. Because the KS equations so closely follow the restricted HF equations, both the restricted open shell and unrestricted methodologies are readily available. A main advantage of this scheme is that it allows a straightforward determination of a large part of the kinetic energy in a simple way. Another advantage, from a more physical point of view, is that it provides an exact one-particle picture of interacting electronic systems. This then provides a rigorous basis for the one-particle arguments used in solid state physics and chemistry to explain and predict certain features of chemical bonding.

2.2 The exchange-correlation energy

Kohn-Sham density functional theory has proven to be a highly competitive method for a wide range of applications in solid state physics. For using the Kohn-Sham equations in practice we must know what the form of the exchange-correlation energy functional is. The central objective of Kohn-Sham DFT is to come up with accurate approximations to the exact exchange-correlation functional. As the exact form of E_{xc} is not known, some sort of approximations for E_{xc} have been used. These approximations are usually cast in the form of integral expressions of the type

$$E_{xc}[n] = \int e_{xc}(n, \nabla n, \nabla^2 n \dots) d\mathbf{r} \quad (2.22)$$

e_{xc} is called the exchange-correlation energy density. A significant portion of the vocabulary of modern DFT was developed by John Perdew in reference to a systematic approach called Jacob's ladder of density-functional approximations. In this classification, density-functional approximations that are constructed using the electron density n and no other ingredients represent rungs 1 of the ladder and are termed local density approximations (LDA), which have been used in solid state physics for quite some time. The class of functionals based on the generalized gradient approximation (GGA), which have made DFT a valuable tool in chemistry, represent rung two where e_{xc} depends on n and ∇n . In rung three we have meta-GGA functionals, for molecules, which are recently developed and have been shown to yield accuracy comparable to hybrid functionals, which include a certain amount of Hartree-Fock

(HF) exchange, have further improved upon the GGA results. However, a comparison with hybrid functionals in solids is difficult due to the high computational demands of traditional hybrids. In hybrid functionals the numerical cost increases as one climbs up, and this may not necessarily bring more information. Most problems in "computational nanoscience" are performed part way up the ladder, and this situation will probably remain true for some time. The historical development of density-functional approximations for exchange-correlation may be regarded as the process of climbing Jacob's ladder or as a story of passing the following milestones:

1. Analysis of exactly solvable models and introduction of various local density approximations e.g.

$$E_{xc}^{LDA}[n] = \int e_{xc}(n) d\mathbf{r} \quad (2.23)$$

2. Development of GGAs and meta-GGAs by bringing into play semi local ingredients and by grafting selected properties of the exact functional.

$$E_{xc}^{GGA}[n] = \int e_{xc}(n, \nabla n) d\mathbf{r} \quad (2.24)$$

3. Introduction of exact exchange into semi local functionals (hybrid DFT).
4. Empirical construction (fitting).
5. Development of nonlocal correlation functionals compatible with exact exchange

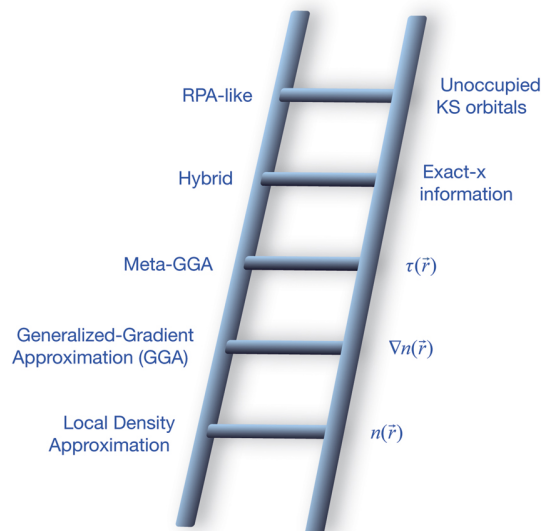


Figure 2.4: Schematic diagram of "Jacob's ladder" of exchange-correlation functionals proposed by J. P. Perdew [89].

From rungs 1 to 4, the theory is involving only occupied Kohn-Sham orbitals, while in a fifth rung, occupied and virtual Kohn-Sham orbitals are involved.

2.2.1 The local-density approximation

In the local density approximation (LDA), which is the simplest approximation, assuming that the density can be treated locally as uniform electron gas (the uniform electron gas is a system of many interacting electrons moving in the field of a uniform positive background charge as the average electron density, which is $n(\mathbf{r}) = \text{const}$); the value of $E_{xc}[n(\mathbf{r})]$ is approximated by the exchange-correlation energy of an electron in a homogeneous electron gas of the same density $n(\mathbf{r})$ and is given by:

$$E_{xc}^{LDA}[n(\mathbf{r})] = \int \epsilon_{xc}(n(\mathbf{r}))n(\mathbf{r})d\mathbf{r} \quad (2.25)$$

This approximation was originally introduced by Kohn and Sham and holds for a slowly varying density. The most accurate data for $\epsilon_{xc}(n(\mathbf{r}))$, is from quantum Monte Carlo[19, 121] calculations. The exchange-correlation potential is then given by:

$$V_{xc}^{LDA}[n(\mathbf{r})] = \frac{\delta E_{xc}^{LDA}}{\delta n(\mathbf{r})} = \epsilon_{xc}(n(\mathbf{r})) + n(\mathbf{r})\frac{\partial \epsilon_{xc}(n(\mathbf{r}))}{\partial n(\mathbf{r})} \quad (2.26)$$

The exchange energy of the electron gas is given exactly by [5]

$$E_x^{LDA}[n] = \left(\frac{3}{4}\right) \left(\frac{3}{\pi}\right)^{\frac{1}{3}} \int n^{\frac{4}{3}}(\mathbf{r})d\mathbf{r}, \quad (2.27)$$

while for the correlation energy of the electron gas we just have the form of analytic functionals:

$$E_c^{LDA}[n] = A \int n(1 + \alpha_1 \mathbf{r}_s) \log \left[1 + \frac{1}{A(\beta_1 \mathbf{r}_s^{\frac{1}{2}} + \beta_2 \mathbf{r}_s + \beta_3 \mathbf{r}_s^{\frac{3}{2}} + \beta_4 \mathbf{r}_s^2)} \right] d\mathbf{r} \quad (2.28)$$

where $\mathbf{r}_s = (\frac{3}{4\pi n})^{1/3}$ and $\alpha_1, \beta_1, \beta_2, \beta_3$ and β_4 are fixed parameters. The LDA is often surprisingly accurate and for systems with slowly varying charge densities generally gives very good results. The failings of the LDA are now well established: it has a tendency to favor more homogeneous systems and over-binds molecules and solids. In weakly bonded systems these errors are exaggerated and bond lengths are too short. In good systems where the LDA works well, often those mostly consisting of *sp* bonds, geometries and bond lengths and angles are accurate to within a few percent. Quantities such as the dielectric and piezoelectric constant are approximately 10% too large. The principal advantage of LDA-DFT over methods such as Hartree-Fock, which is a method typically used to solve the time-independent Schrödinger equation for a multi-electron atom or molecule as described in the Born-Oppenheimer approximation, is that where the LDA works well (correlation effects are well accounted for), many experimentally relevant physical properties can be determined to a useful level of accuracy. Difficulties arise where it is not clear whether the LDA is applicable. For example, although the LDA performs well in bulk group-IV semiconductors it is not immediately clear how well it performs at surfaces of these materials[19].

The bond lengths and lattice constants are predicted fairly accurate with local density approximation, but it severely overestimates atomization energies of molecules and solids. For comparison, the Hartree-Fock method, which is computationally more expensive than the LDA, predicts bond lengths much less accurately than LDA and underestimates atomization energies with a mean absolute error which is twice as large as the over-binding error of LDA.

2.2.2 Generalized-Gradient approximations

LDA treats all systems as homogeneous. However, real systems are clearly inhomogeneous with spatially varying electric fields due to nuclei and screening. In order to take this into account, a step may be taken beyond the LDA by including the derivative information of the density into the exchange-correlation functionals. One way to do this is to try to include gradients $|\nabla n(\mathbf{r})|$, $|\nabla n(\mathbf{r})|^2, \dots$ into the approximation. The reduced gradient s , which can one define as:

$$s = \frac{|\nabla n|}{n^{\frac{4}{3}}} \quad (2.29)$$

is related to $|\nabla n|$ so it is convenient to make the energy density e_{xc} depend on $|\nabla n|$. Through s , one can improve LDA by devising a functional of the form of density-gradient expansions:

$$E_{xc}[n] = \int e_{xc}^{LDA}[n][1 + \mu(n)s^2 + \dots]d\mathbf{r} \quad (2.30)$$

However, Perdew et al.[87] explained that the density-gradient expansions failed to give $E_{xc}[n]$ because, on the one hand, this expansion gives the negativity constraint for the exchange hole, $n_x(\mathbf{r}_1, \mathbf{r}_2)$,

$$n_x(\mathbf{r}_1, \mathbf{r}_2) < 0 \quad (2.31)$$

so,

$$\int n_{xc}(\mathbf{r}_1, \mathbf{r}_2)d\mathbf{r}_2 = -1 \quad (2.32)$$

which is associated with second-order truncated density-gradient expansions translated via the exact E_{xc} :

$$E_{xc}[n] = \frac{1}{2} \int d\mathbf{r}_1 n(\mathbf{r}_1) \int d\mathbf{r}_2 \frac{n_{xc}(\mathbf{r}_1, \mathbf{r}_2)}{|\mathbf{r}_1 - \mathbf{r}_2|} \quad (2.33)$$

On the other hand, a pathological divergence in the exponential density tails is found in all atomic and molecular charge distributions in the $v_x(\mathbf{r}) = \frac{\delta E_x[n]}{\delta n(\mathbf{r})}$, which is caused by the density-gradient correction term. This can be observed when $n(\mathbf{r}) = e^{-b\mathbf{r}}$ is substituted with Eq. (2.29) to obtain: $s = be^{\frac{b\mathbf{r}}{3}} \rightarrow \infty$ as $\mathbf{r} \rightarrow \infty$. To solve this problem, Perdew, Becke, and others suggested to replace the truncated series in square brackets in Eq. (2.30) with a damping function $F_{xc}(n, s)$, such that it remains finite as $\mathbf{r} \rightarrow \infty$ which leads to generalized gradient approximations (GGAs) like:

$$E_x[n] = \int e_{xc}^{LDA}(n)F_{xc}(n, s)d\mathbf{r} \quad (2.34)$$

where F_{xc} varies from case to case e.g. in 1986, it was introduced by Becke[6] as:

$$F_{xc}^{PBE}(s) = 1 + \frac{\alpha s^2}{1 + bs^2} \quad (2.35)$$

After generalized gradient approximations were perfected by the late 1980s, they performed not only much better than the LDA, but also quite well relative to medium-level wave-function methods. The correlation energy of GGAs has more complicated forms but uses damping functions to ensure that the correlation energy density has proper behavior in various physically relevant limits.

2.3 Hybrid functionals

The accuracy of DFT originates from the fact that the largest contributions to the total energy can be calculated exactly. An analytical expression is unknown only for the exchange-correlation energy; however, simple approximations such as local density approximation (LDA) and generalized gradient approximation (GGA), provide an accurate prediction of electronic and structural ground-state properties. The most prominent flaws in the local functionals are the presence of a spurious self-interaction and the systematic underestimation of the band gap. Describing the exchange-correlation energy with an LDA or a GGA functional, even in a single-electron system, the exchange-correlation and the Hartree contribution to the total energy do not cancel each other. As a consequence, these local functionals incorporate an unphysical self-interaction error (SIE), which leads to a delocalization and is, in particular, important for localized d and f states.

In 1993, however, Becke showed[8] that one can go beyond the accuracy of GGA by representing a universally applicable method, which should be a functional whose density derivative exists, so that it can be used both for electronic and geometric structural relaxations, to give accurate band gaps, and be quite computationally efficient. These conditions, which allow for some increase in computational cost, can be met by the hybrid functionals in which the exchange part is a contribution with a mixture of the exact exchange functional and a semi local approximation. This discovery led to many hybrid functionals such as B3PW91, B3LYP, PBEh and HSE. The basic form of hybrid functionals is:

$$E_{xc} = \alpha E_x^{exact} + (1 - \alpha)E_x + E_c \quad (2.36)$$

where E_x and E_c are some semi local density-functional approximations, and α ($0 \leq \alpha \leq 1$) is a universal parameter called mixing fraction. The value of α is usually determined by empirical fitting of Eq. 2.36 to reproduce experimental atomization energies, exact non-relativistic energies, reaction barrier heights, and other data. Fitting to atomization energies typically gives $\alpha \approx 0.2$ for GGAs and $\alpha \approx 0.1$ for meta-GGAs, while fitting to reaction barrier heights yields $\alpha \approx 0.5$.

2.3.1 Screened hybrid functionals

On the one hand, the idea of range-separated or screened hybrid functionals (as proved to be one of the DFT's biggest successes for the past decade) came up after the exact (Hartree-Fock-type) exchange functionals were not adequately able to describe opposite-spin electrons at close range (small $r_{12} \equiv |r_1 - r_2|$), while the Hartree-Fock method did not correlate the motion of electrons with opposite spins at all. The Coulomb part can be categorized into the short range (SR) and the long range (LR)[30] terms which are expressed as:

$$\frac{1}{r_{12}} = \frac{1 - f(r_{12})}{r_{12}} + \frac{f(r_{12})}{r_{12}}. \quad (2.37)$$

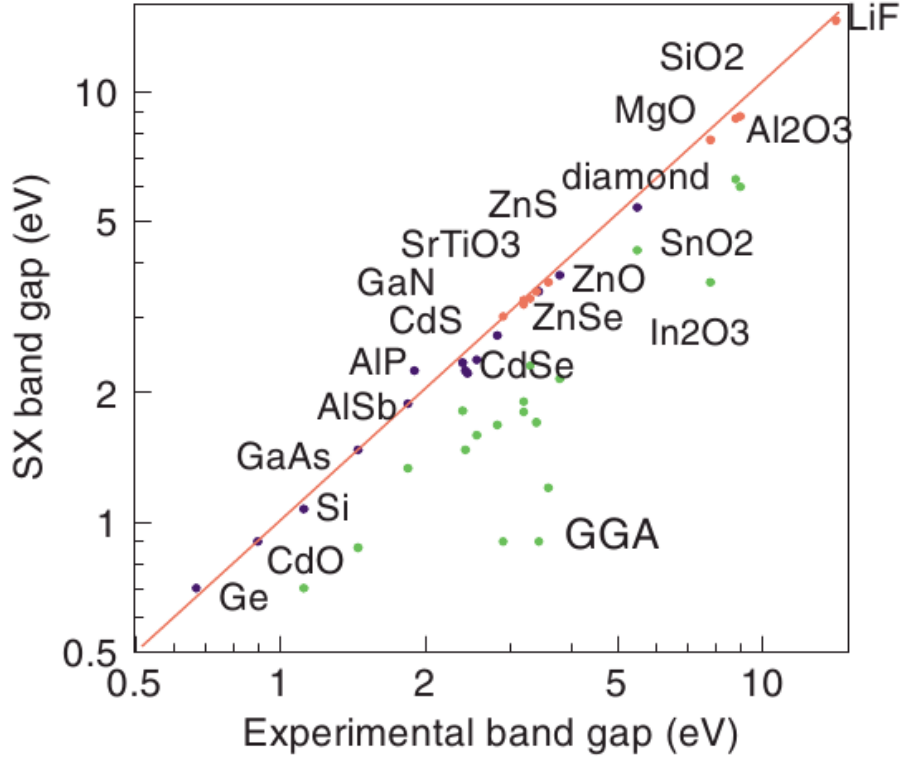


Figure 2.5: Theoretical versus experimental band gaps[24]

One of the popular choices for the screening function is the Gauss error function that is convenient in calculations employing Gaussian-type basis sets because all necessary two-electron integrals in this case can be evaluated efficiently.

$$f(r_{12}) = \text{erf}(\omega r_{12}) = \frac{2}{\sqrt{\pi}} \int_0^{\omega r_{12}} e^{-t^2} dt \quad (2.38)$$

$$\frac{1}{r_{12}} = \frac{\text{erfc}(\omega r_{12})}{r_{12}} + \frac{\text{erf}(\omega r_{12})}{r_{12}} \quad (2.39)$$

Where the first statement in formula is SR and the second one is LR. $\text{erfc}(\omega r_{12}) = 1 - \text{erf}(\omega r_{12})$ and ω are an error function and an adjustable parameter, respectively. Two limiting cases are :

$$\omega = \begin{cases} 0 & \text{SR} = \text{full coulomb operator} \\ \infty & \text{LR} = \text{full coulomb operator} \end{cases}$$

This screening function needs the associated exchange holes which are known for only a handful of density-functional approximations such as LDA, Becke-Roussel[7, 40], PBE, and TPSS. To avoid the need to the exchange hole, Hirao and *et al.*[56, 82] proposed a different definition for the screened components which is applicable to any GGA approximations.

Finally, replacing the long-range portion of exact exchange in a global hybrid functional with a long-range part of a semi local density functional makes hybrid DFT calculations possible on solids [49]. Heyd, Scuseria, and Ernzerhof indicated that lattice constants and band gaps predicted from HSE are much more accurate than any standard semi local functional including LDA, PBE, and TPSS [48] approximations.

$$E_{xc}^{HSE}(\omega) = \alpha E_x^{exact,SR}(\omega) + (1 - \alpha) E_x^{PBE,SR}(\omega) + E_x^{PBE,LR}(\omega) + E_c^{PBE} \quad (2.40)$$

where $0 \leq \omega < \infty$ The HSE functional can be viewed as an interpolation between pure PBE and the global hybrid PBE functional (PBEh). When $\alpha = 0.25$ and $\omega = 0$, HSE reduces to PBEh, while in the limit $\omega \rightarrow \infty$, it reduces to PBE. Comparing to the other methods mentioned above, the HSE method leads to substantially improved band gaps. Table 2.1 and Fig 2.5 show the results obtained with the LDA, GGA approximation, HSE functional and experimental results for the fundamental band gap of solids. The mixing parameter for HSE06 is 25% which modifies the hybrid functional equation in Eq.(2.36) to

$$H_{XC}^{HSE06} = 0.25 E_x^{Hf,SR}(\omega) + 0.75 E_x^{PBE,SR}(\omega) + E_x^{PBE,LR}(\omega) + E_c^{PBE} \quad (2.41)$$

For the HSE hybrid functional, the optimal value of ω rests between 0.2 and 0.3 \AA^{-1} [8]

Table 2.1: The theoretical and experimental band gap results for some selected materials in eV.

Materials	LDA	GGA	HSE	Exp
C ^a	4.11	4.21	5.42	5.48
Si ^b	0.61	0.61	1.17	1.17
Ge ^{d,e}	0.00	0.00	0.83	0.74
ZnO ^c	0.75	0.80	2.49	3.44

^a Reference [119], ^b Reference [55]

^c Reference [1], ^d Reference [119]

^e Reference [119]

2.4 Spin-Orbit Coupling

For high electrons velocities (close to the speed of light), which mostly occur in heavy elements (with nuclear numbers, Z , more than 50), the kinetic energy can reach to very high values. By traveling the electrons with the velocity, \mathbf{v} , around the nucleus, from the potential gradient due to the screened nucleus, they experience electric field \mathbf{E} and the magnetic field, $\mathbf{B} = \frac{1}{c}(\mathbf{E} \times \mathbf{v})$, which can be coupled with the spin, $\boldsymbol{\sigma}$. Starting from the Dirac equation :

$$H = -eV(\mathbf{r}) + \beta mc^2 + \boldsymbol{\alpha} \cdot (c\mathbf{p} + e\mathbf{A}(\mathbf{r})) \quad (2.42)$$

where \mathbf{A} and V are vector and scalar potential, respectively and e and m are charge and mass, respectively,. The spin can be expressed, S as the Pauli spin-matrices, σ , while β is the matrix of the same rank:

$$S = \langle \psi | \boldsymbol{\sigma} | \psi \rangle; \boldsymbol{\sigma}_x = \begin{pmatrix} 0 & 1 \\ 1 & 0 \end{pmatrix}, \boldsymbol{\sigma}_y = \begin{pmatrix} 0 & -i \\ i & 0 \end{pmatrix}, \boldsymbol{\sigma}_z = \begin{pmatrix} 1 & 0 \\ 0 & -1 \end{pmatrix} \boldsymbol{\alpha} = \begin{pmatrix} 0 & \sigma \\ \sigma & 0 \end{pmatrix}, \boldsymbol{\beta} = \begin{pmatrix} I_2 & 0 \\ 0 & -I_2 \end{pmatrix} \quad (2.43)$$

where are $\alpha = 4 \times 4$ matrices, $I_2 : 2 \times 2$ unit matrix. Coming back to the Schrödinger equation and rewrite the 4 component wavefunction as a 2-spinor (large (Ψ) and small (χ)) components. By rewriting the Dirac equation we have :

$$\begin{aligned} (E' - mc^2 + eV(\mathbf{r}))\psi &= \boldsymbol{\sigma} \cdot (c\mathbf{p} + e\mathbf{A}(\mathbf{r}))\chi \\ (E' - mc^2 + eV(\mathbf{r}))\chi &= \boldsymbol{\sigma} \cdot (c\mathbf{p} + e\mathbf{A}(\mathbf{r}))\psi, \end{aligned} \quad (2.44)$$

If we assume that $eV(\mathbf{r}) \ll E' - mc^2 \approx 2mc^2$ and $E = E' - mc^2$, we have :

$$[E + eV(\mathbf{r}) - \frac{1}{2m}(\mathbf{p}(\mathbf{r}) + \frac{e}{c}\mathbf{A}(\mathbf{r}))^2]\psi = 0 \quad (2.45)$$

To acquire spin-matrices terms, Eq. (2.45) must be refined to Dirac equation. So just for the large component, we have:

$$\begin{aligned} [E + eV(\mathbf{r}) - \frac{1}{2m}(\mathbf{p}(\mathbf{r}) + \frac{e}{c}\mathbf{A}(\mathbf{r}))^2 + \frac{1}{2mc^2}(E + eV(\mathbf{r}))^2 \\ + i\frac{e\hbar}{(2mc)^2}\mathbf{E}(\mathbf{r}) \cdot \mathbf{p} - \frac{e\hbar}{(2mc)^2}\boldsymbol{\sigma} \cdot (\mathbf{E}(\mathbf{r}) \times \mathbf{p}) - \frac{e\hbar}{2mc}\boldsymbol{\sigma} \cdot \mathbf{B}(\mathbf{r})]\psi = 0 \end{aligned} \quad (2.46)$$

The first three terms give the normal Schrödinger equation in the non-relativistic limit. The fourth term is mass-velocity term, and the 2 terms which are at the end of equation are scalar-relativistic terms, which are significant for heavy elements such as CdTe and HgTe components. In the Schrödinger equation, there is no term that explicitly includes the spin-operator. So starting from the Eq. (2.46) is given:

$$[-\frac{1}{2}\nabla^2 + V(\mathbf{r}) + \frac{\mu_B}{2c}\boldsymbol{\sigma} \cdot (\mathbf{E}(\mathbf{r}) \times \mathbf{p})]\psi_i = \epsilon_i\psi_i \quad (2.47)$$

As the electric field comes from the potential, ($V(\mathbf{r})$), we can rewrite the term: $\boldsymbol{\sigma} \cdot (\mathbf{E}(\mathbf{r}) \times \mathbf{p}) = \boldsymbol{\sigma} \cdot (\nabla V(\mathbf{r}) \times \mathbf{p}) = \frac{1}{r}\frac{dV(r)}{dr}(\boldsymbol{\sigma} \cdot \mathbf{L}) = \xi\boldsymbol{\sigma} \cdot \mathbf{L}$ The term $\xi\boldsymbol{\sigma} \cdot \mathbf{L}$ is the spin-orbit coupling (SOC), where the ξ is spin-orbit coupling constant, and \mathbf{L} is the orbital momentum operator. As the potential is proportional to the nuclear number of atom, the SOC constant will be large for the heavy atoms.

2.4.1 Rashba effect

In crystals, the electric field is given by the gradient of the crystal potential $E = -\nabla V$, which produces a spin-orbit field $w(p) = \frac{-\mu_B(\nabla V \times p)}{mc^2}$. As shown in previous part, traveling

electron at the velocity \mathbf{v} in an electric field through a Lorentz transformation turns this field into the magnetic field and this can couple to the electron spin, σ . A question arised here is that how such a field is generated inside a solid, presupposing the absence of any external field. This question can be answered with symmetries in the crystal and their effect on the eigenvalues of the certain state. With or without an inversion, symmetry center ($\mathbf{k}=0$) make changes in physical properties in crystals. The lack of inversion symmetry, which means $V(r) \neq V(-r)$, as a consequence of spin-orbit coupling the degeneracy of the bands can be lifted and the electronic energy bands are split by spinorbit (SO) coupling [17]. As seen in the previous section, when the electrons move in the electric field, they will experience the Lorentz-transformed electric field as magnetic field, so the energy of a right-moving spin-up particle will not be equal to the energy of a left moving spin-down particle,

$$\epsilon(\mathbf{k}, \uparrow) \neq \epsilon(-\mathbf{k}, \downarrow) \quad (2.48)$$

In contrast, for the crystal with the inversion symmetry we have:

$$\epsilon(\mathbf{k}, \uparrow) = \epsilon(-\mathbf{k}, \downarrow) \quad (2.49)$$

For an asymmetric quantum well, bulk inversion asymmetry and structure-inversion asym-

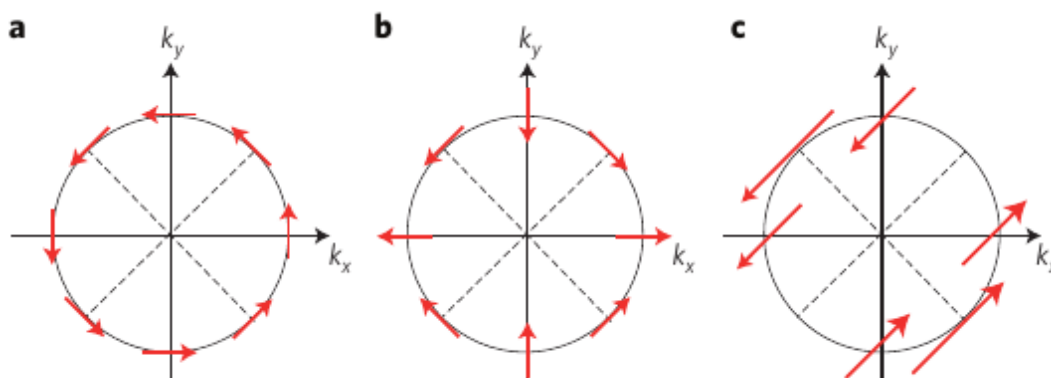


Figure 2.6: The illustration below shows the spin texture at the Fermi surface in the case of Rashba (panel a) and strain-induced (panel b) p-linear Dresselhaus SO coupling. In the example shown in panel c, when both are present with equal magnitude, the SO field aligns along with the $[110]$ direction, resulting in, for instance, the suppression of spin relaxation interaction in this direction [76]

metry give rise to Dresselhaus and Rashba spin-orbit contributions to the Hamiltonian, respectively. For the first time in 1955, Dresselhaus *et al.* [31] emphasized on the one-electron energy levels in bulk semiconductors such as GaAs or InSb, zinc-blend III-V semiconductor compounds, where lacking a center of inversion has important consequences of spin-orbit coupling. The outcome of his research was even if $\mathbf{B} = 0$, we have spin splitting of the electron and hole states at nonzero wave vectors. The Dresselhaus Hamiltonian which describes

the bulk inversion asymmetry (BIA) spin splitting due to SOC can be given by:

$$H_D = \alpha_D[\sigma_x p_x(p_y^2 - p_z^2) + \sigma_y p_y(p_z^2 - p_x^2) + \sigma_z p_z(p_x^2 - p_y^2)] \quad (2.50)$$

where α_D is known as the Dresselhaus parameter. The Eq.(2.50) can be reduced as Eq.(2.51) in the presence of strain along the (001) direction :

$$H_D = \alpha_D p_z^2 (\sigma_x p_x - \sigma_y p_y) \quad (2.51)$$

In 1959, besides zincblende components, Rashba et al. mention the second important

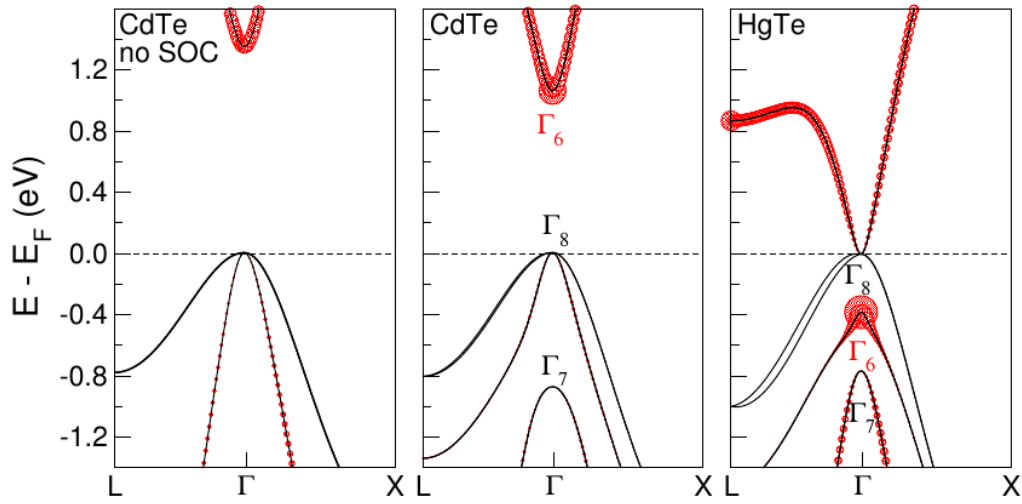


Figure 2.7: The band structure of CdTe and HgTe are shown around the Fermi level. In the case of CdTe, can be seen in the Γ point for highest occupied state for non-SOC. Three-fold degeneracy which is split with SOC (CdTe in middle) can be observed. In Fig HgTe (right) can be seen along the $\bar{\Gamma}L$ an additional splitting due to the Dresselhaus effect[2, 9].

crystal structure like inversion asymmetric wurtzite structure (e.g., GaN, CdS, and ZnO). He published papers about the Symmetry of Energy Bands in Crystals of Wurtzite Type[92], which demonstrated that the spin splitting of the dispersion $E(\mathbf{k})$ of s electrons near the Γ point $\mathbf{k} = 0$ is linear in \mathbf{k} and isotropic for \mathbf{k} perpendicular to the wurtzite c axis so that can be gotten a ring of extrema in the dispersion $E(\mathbf{k})$. It is the feature associated with Rashba spin orbit coupling. In the local frame of moving electrons with the effective mass, m^* , which is propagated with the velocity in an external electric field \mathbf{E} defined in a global frame of reference, the relativistic Lorentz transformation gives rise to a magnetic field $B = \frac{1}{c}(\mathbf{v} \times \mathbf{E}) = \frac{1}{m^*c}(\mathbf{k} \times \mathbf{E})$. The Rashba Hamiltonian can be given as :

$$H_R = \alpha_R \boldsymbol{\sigma}(\mathbf{p} \times \mathbf{E}), \quad H_R = \alpha_R \boldsymbol{\sigma} \cdot (\mathbf{k} \times \mathbf{E}), \quad H_R = \alpha_R (|E|) \boldsymbol{\sigma} \cdot (\mathbf{k} \times \hat{e}) \quad (2.52)$$

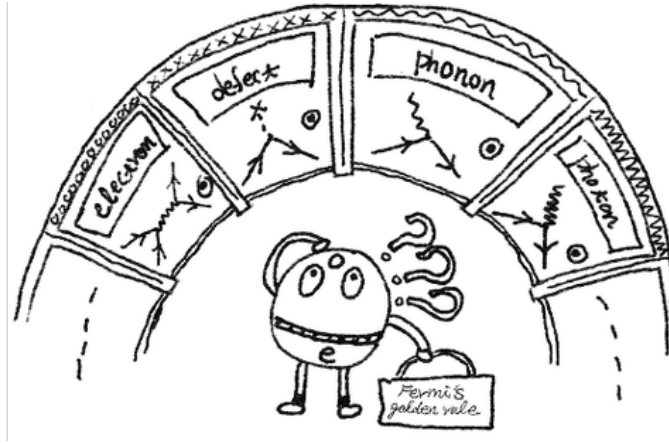
Obviously, some difference between Rashba and Dresselhaus terms exist such as : in the Dresselhaus term, spin splitting is proportional to k^3 , $\epsilon_D \propto k^3$ while in Rashba-term is linear

in k , $\epsilon_R \propto k$. Besides this, can be observed that the band extremum of a parabolic state from a point to a ring of extrema changes in Rashba terms, while in the Dresselhaus term the point is character of the band extremum. Finally the total SOC Hamiltonian can be written as:

$$H_{SOC} = H_D + H_R, \quad (2.53)$$

which results in a zero-field splitting. In Fig. (2.6), both terms are visualized, where the eigenvalues of the H_{SOC} at the Fermi energy are plotted. In Fig. (2.6)(a): Rashba effect can just be seen, where the Fermi surface consists of two freeelectron-like parabolas equally shifted in the \mathbf{k}_{\parallel} -plane against one another. In this case, i.e., Rashba SOC only, the spin polarization vector is always perpendicularly aligned with respect to \mathbf{k}_{\parallel} and the potential gradient $(\frac{\partial V}{\partial z})\hat{\mathbf{e}}_z$. Fig. (2.6)(b) is related to the Dresselhaus SOC only, in which the diagonal lines are still held for mirror planed; However, the circularly revolving character is lost and strong radial in-plane rotations are found elsewhere. Both Rashba and Dresselhaus SOC are shown in the the Fig. (2.6)(c) at the same time.

3 Theory of electron-phonon interaction



3.1 Introduction

The calculation of the vibrational eigenfrequencies of the crystalline lattice, from the point of view of the theory part (*ab initio* calculations of phonon frequencies), falls into two broad classes: the linear-response approach and the direct approach. In the case of semiconductors and transition metals, the linear-response approach is realized with much more difficulty, since the full dielectric matrix must be calculated in terms of the electronic eigenfunctions and eigenvalues of the perfect crystal. Tractable versions of the linear-response approach have been developed either in terms of a direct calculation of the density response [3] or a perturbation approach to the change in the total energy [41]. In the direct approach, restricted to phonons whose wavelength are compatible with the periodic boundary conditions, the displacement amplitude in terms of the difference in the energies of the distorted and the unperturbed lattices (frozen-phonon method) can be used to calculate the energy of a phonon, i.e. of a periodic distortion of the crystalline lattice. One variant of the direct or total-energy approach concentrates on the forces on the atoms induced by the displacements of other atoms in the supercell. From the forces calculated via the Hellmann-Feynman theorem, certain elements of the force constant matrix can be evaluated. By displacing entire planes of atoms, interplanar force constants may be calculated [67], allowing for the determination of the phonon dispersion relations in certain symmetry directions [64]. In this chapter the theory of electron-phonon coupling is explained with more details.

3.2 Density Functional Perturbation Theory

Calculating the ground state density and total energy of electronic systems, from bulk to nanostructures or molecules can be done very successfully using Density Functional Theory. One question arises about the electronic excited states. Are DFT results accurate in this area or not? The answer is that there are well known failures in the representation of electronic excited states, however if the ground state is perturbed very lightly, which leaves the system close to its electronic ground state, one can easily apply the traditional quantum formalism of perturbation theory, giving the approach of Density Functional Perturbation Theory (DFPT), which has been proposed independently by Zein et al. (1984) [130] and Baroni, Giannozzi, and Testa in Trieste (1987) [3].

3.2.1 Response functions

The calculation of phonon frequencies of the crystalline structure from *ab initio* methods, falls into two classes: the linear response method [3] and the direct method. An analytical way of computing the second derivative of the total energy with respect to a given perturbation can be done by Linear response, or density functional perturbation theory (DFPT)[4], in which a number of properties can be calculated from these methods depending on the nature of this perturbation. For example NMR response comes from magnetic fields; the dynamical matrix and phonons come from a perturbation in ionic positions, etc. The force constants matrix can be obtained by differentiating the Hellmann-Feynman forces on atoms with respect to ionic coordinates. This procedure reveals that the force constants matrix depends on the ground state electron charge density and on its linear response to a distortion of atomic positions.

Due to the variational principle of the density functional formalism, the second order change in energy depends on the first order change in the electron density. Response functions are second, third, or higher order derivatives of the total energy with respect to applied perturbation(s) and the dielectric matrix must be calculated in terms of the electronic eigenfunctions and eigenvalues of the perfect crystal. Typical perturbations can be atomic displacements, homogeneous external electric or magnetic fields, strain, etc. The physical properties related to the derivatives of the total energy such as forces, stress, dipole moment from the 1st order and the phonon dynamical matrix, elastic constants, dielectric susceptibility, Born effective charges, piezoelectricity, internal strain from the 2nd order and the non-linear dielectric susceptibility, phonon-phonon interaction from the 3rd order can be calculated. Further physical properties - such as entropy or thermal expansion - can be obtained integrating the total energy (or a thermodynamic potential) over phononic degrees of freedom. Total energy derivatives can be computed using either direct approaches (e.g., finite differences, molecular-dynamics spectral analysis) or perturbative techniques. The former suffer from various limitations such as size effects, ergodicity constraints, commensurability problems or the difficulty to decouple the responses to perturbations of different wavelengths. The perturbative theory applied to DFT, instead, allows one to treat not only periodic perturbations but also perturbations characterized by a non-zero, commensurate or incommensurate, wavevector. In addition, the computation of 1st order corrections to wavefunctions within perturbation theory can be done using a variational approach and algorithms similar to those used for ground-state (i.e. unperturbed) calculations. Hence, the perturbative tech-

nique can be naturally included in the usual DFT framework, while the external potential, charge density and the total energy are dependent on perturbation parameter, λ , as :

$$V_\lambda(\mathbf{r}) \simeq V(\mathbf{r}) + \lambda \frac{\partial V(\mathbf{r})}{\partial \lambda} + \frac{1}{2} \lambda^2 \frac{\partial^2 V(\mathbf{r})}{\partial \lambda^2} + \dots; \quad (3.1)$$

$$n_\lambda \simeq n(\mathbf{r}) + \lambda \frac{\partial n(\mathbf{r})}{\partial \lambda} + \frac{1}{2} \lambda^2 \frac{\partial^2 n(\mathbf{r})}{\partial \lambda^2} + \dots, \quad (3.2)$$

and

$$E_\lambda \simeq E + \lambda \frac{\partial E}{\partial \lambda} + \frac{1}{2} \lambda^2 \frac{\partial^2 E}{\partial \lambda^2} + \dots \quad (3.3)$$

The first-order derivative $\frac{\partial E}{\partial \lambda}$ does not depend on any derivative of $n(\mathbf{r})$ (from Hellmann-Feynman theorem):

$$\frac{\partial E}{\partial \lambda} = \int n(\mathbf{r}) \frac{\partial V(\mathbf{r})}{\partial \lambda} d\mathbf{r} \quad (3.4)$$

In this thesis the Raman spectroscopy (discussed in chapter 4) was calculated from Born effective charge within DFPT method and the phonon dispersions in chapter 5 and 6 were calculated with the help of finite displacement. Both methods were applied in the plane wave basis set code, the Vienna Ab initio Simulation Package, VASP.

3.2.2 Perturbation theory

The perturbed Hamiltonian of the system can be written as unperturbed Hamiltonian, $H^{(0)}$, plus an external potential, $V_{ext}(\lambda)$:

$$H(\lambda) = H^{(0)} + V_{ext}(\lambda) \quad (3.5)$$

Where the unperturbed Schrödinger equation gives us the solution :

$$H^{(0)}|\psi_i^{(0)}\rangle = \epsilon_i^{(0)}|\psi_i^{(0)}\rangle \quad (3.6)$$

where i labels eigenvalues and eigenvectors of $H^{(0)}$. The next step is to get the answer of a perturbation of the Hamiltonian $H(\lambda) = H^{(0)} + \lambda H^{(1)} + \lambda^2 H^{(2)}$ which will change the resulting eigenstates and eigenvalues, generically to arbitrary order in λ . The unperturbed wavefunctions and eigenvalues are shown as $\psi_i(\lambda) = \psi_i^{(0)} + \lambda \psi_i^{(1)} + \lambda^2 \psi_i^{(2)}$ and $\epsilon_i(\lambda) = \epsilon_i^{(0)} + \lambda \epsilon_i^{(1)} + \lambda^2 \epsilon_i^{(2)}$, respectively. The goal is to solve the perturbed Schrödinger equation:

$$H(\lambda)|\psi_i(\lambda)\rangle = \epsilon_i(\lambda)|\psi_i(\lambda)\rangle \quad (3.7)$$

The first-order correction to the wavefunctions can be computed by solving the Sternheimer equation [113]:

$$(H^{(0)} - \epsilon_i^{(0)})|\psi_i^{(1)}\rangle = -(H^{(1)} - \epsilon_i^{(1)})|\psi_i^{(0)}\rangle \quad (3.8)$$

Eq. (3.8) can be solved by expanding $|\psi^{(1)}\rangle$ (which is orthonormal and complete) in the basis of $|\psi^{(0)}\rangle$:

$$|\psi^{(1)}\rangle = \sum_{j \in I^\perp} |\psi^{(0)}\rangle \frac{\langle \psi_j^{(0)} | H^{(1)} | \psi_i^{(0)} \rangle}{\epsilon_i^{(0)} - \epsilon_j^{(0)}} \quad (3.9)$$

The subset I of the wavefunction(s) is corresponding to the eigenvalue $\epsilon_i^{(0)}$ and the subset of the wavefunctions in the orthogonal subspace I^\perp . The 1st order and the 2nd order eigenvalues are :

$$\begin{aligned} \epsilon_i^{(1)} &= \langle \psi_i^{(0)} | H^{(1)} | \psi_i^{(0)} \rangle \\ \epsilon_i^{(2)} &= \langle \psi_i^{(0)} | H^{(2)} | \psi_i^{(0)} \rangle + \langle \psi_i^{(0)} | H^{(1)} - \epsilon_i^{(1)} | \psi_i^{(1)} \rangle \end{aligned}$$

3.2.3 Density Functional Perturbation Theory

In this part the perturbation theory is integrated in Density Functional Theory. In DFT, by minimizing the functional of the electronic density, the ground-state energy of the electronic system can be obtained as

$$E_{el}[n(\lambda)] = \sum_{i=1}^{N_e} \langle \psi_i(\lambda) | T + V_{ext}(\lambda) | \psi_i(\lambda) \rangle + E_{Hxc}[n(\lambda)] \quad (3.10)$$

where the Kohn-Sham orbitals follow the orthonormality constraint $\langle \psi_i(\lambda) | \psi_j(\lambda) \rangle = \delta_{ij}$ and the Hartree and exchange-correlation energy functional is denoted as E_{Hxc} . The electronic density is given by :

$$n(\mathbf{r}, \lambda) = n^{(0)}(\mathbf{r}) + \lambda n^{(1)}(\mathbf{r}) + \lambda^2 n^{(2)}(\mathbf{r}) + \dots \quad (3.11)$$

As mentioned above, the goal of DFPT is to compute the derivatives of the electronic energy of DFT with respect to different perturbations. The electronic energy part in the first order correction can be computed from the 0th order wavefunctions and the perturbing potential at the 1st order:

$$E_{el}^{(1)} = \sum_{i=1}^{N_e} \langle \psi_i^{(0)} | H^{(1)} | \psi_i^{(0)} \rangle = \sum_{i=1}^{N_e} \langle \psi_i^{(0)} | [T + V_{ext}]^{(1)} | \psi_i^{(0)} \rangle + \left. \frac{dE_{Hxc}[n^{(0)}]}{d\lambda} \right|_{\lambda=0} \quad (3.12)$$

Eq.(3.12) is the Hellmann-Feynman theorem for DFT. The first-order change in the Hamiltonian and density can be done by:

$$\begin{aligned} H^{(1)}(\mathbf{r}) &= T^{(1)} + V_{ext}^{(1)} + V_{Hxc}^{(1)} = T^{(1)} + V_{ext}^{(1)} + \int \frac{\partial^2 E_{Hxc}}{\partial n(r) \partial n(r')} \Big|_{n^{(0)}} n^{(1)}(r') dr' \\ n^{(1)}(\mathbf{r}) &= \sum_{i=1}^{N_e} \left[\psi_i^{*(1)}(r) \psi_i^{(0)}(r) + \psi_i^{*(0)}(r) \psi_i^{(1)}(r) \right] \\ V_{Hxc}(\mathbf{r}, \lambda) &= \frac{\partial E_{Hxc}[n(\lambda)]}{\partial n(r)} \end{aligned}$$

This explanation explicitly shows that the 2^{nd} order derivatives of the total energy are completely determined by the 1^{st} order derivatives of the wavefunctions. The practical importance of the "2n + 1" theorem is that it allows access to 3^{rd} order derivatives of the total energy, e.g. 3^{rd} order effects (such as anharmonic phonon line widths, Raman scattering cross sections, nonlinear optical response) at the same computational cost as harmonic properties. The interatomic force constants and dynamical matrices are 2^{nd} -order derivatives of the Born Oppenheimer energy with respect to atomic displacements. Hence they can be accurately and efficiently computed using DFPT [42].

3.3 Adiabatic approximation

finding solutions for the Schrödinger equation, Eq. (3.13),

$$H\Psi(\{\mathbf{R}, \mathbf{r}\}) = \varepsilon\Psi(\{\mathbf{R}, \mathbf{r}\}) \quad (3.13)$$

is the task where the dynamics of electrons and ions in a crystal can be described by the total Hamiltonian

$$H = T_N + V_{N-N} + T_e + V_{e-e} + V_{e-N} \quad (3.14)$$

where $\{\mathbf{R}\}$ and $\{\mathbf{r}\}$ describe the locations of all ions and electrons, respectively. Solving Eq. (3.13) is too complicated when having a large number of ions and electrons in solid. As the speed of electron is much faster than ions (because a proton has 1836 times the mass of the electron), the inverse mass of the nuclei, $\frac{1}{M}$, in the general Hamiltonian can be regarded. If the mass of nuclei is set as infinite and perturbation series can be defined in terms of the kinetic energy of nucleus. Decoupling of the dynamics of the electrons and ions and neglecting the electronic excitations induced by the ionic motion is described by the adiabatic or Born-Oppenheimer approximation which is an excellent approximation assuming the electrons adiabatically follow the ions so the electronic properties can be calculated by fixing the ions in a particular configuration. The total wavefunction can be written as a product :

$$\Psi(\{\mathbf{R}, \mathbf{r}\}) = \chi(\{\mathbf{R}\})\Psi(\{\mathbf{r}\}; \{\mathbf{R}\}), \quad (3.15)$$

Since $\Psi(\{\mathbf{r}\}; \{\mathbf{R}\})$ defines a complete set of states for the electrons at each $\{\mathbf{R}\}$ and $\chi(\{\mathbf{R}\})$ and depends only parametrically on the ion coordinates while the ionic wave function, depends only on the ionic positions, $\{\mathbf{R}\}$. Going beyond the adiabatic approximation is can be reached by expanding the wavefunction of the solid in the form of :

$$\Psi_s(\{\mathbf{R}, \mathbf{r}\}) = \sum_i \chi_{si}(\{\mathbf{R}\})\Psi_i(\{\mathbf{r}\}; \{\mathbf{R}\}) \quad (3.16)$$

The eigenvalue problem $H\Psi_s = \varepsilon_s\Psi_s$ leads to the following equation for the ionic part

$$[T_N + \varepsilon_e(\{\mathbf{R}\}) - \varepsilon_s]\chi_{si}(\{\mathbf{R}\}) = - \sum_{i'} G_{ii'}\chi_{si'}(\{\mathbf{R}\}) \quad (3.17)$$

, where $G_{ii'} = K_{ii'} + P_{ii'}$ where $K_{ii'}$ and $P_{ii'}$ are non-adiabatic terms which can be obtained by :

$$K_{ii'}(\{\mathbf{R}\}) = \sum_J \frac{1}{M_J} \langle \Psi_i(\{\mathbf{r}\}; \{\mathbf{R}\}) | \nabla_J | \Psi_{i'}(\{\mathbf{r}\}; \{\mathbf{R}\}) \rangle \nabla_J \quad (3.18)$$

$$P_{ii'}(\{\mathbf{R}\}) = \sum_J \frac{1}{2M_J} \langle \Psi_i(\{\mathbf{r}\}; \{\mathbf{R}\}) | \nabla_J^2 | \Psi_{i'}(\{\mathbf{r}\}; \{\mathbf{R}\}) \rangle \quad (3.19)$$

Derivatives of the electronic wavefunctions with respect to the ion coordinates, and take into account possible excitations in the electronic subsystem due to the motion of the ions are contained in two of off-diagonal matrix element, $K_{ii'}(\{\mathbf{R}\})$ and $P_{ii'}(\{\mathbf{R}\})$, where the $K_{ii'}(\{\mathbf{R}\})$ is the dominant one. The adiabatic approximation is adequate for both free-electron-like systems and for compounds possessing tighter bound valence electrons like transition metals.

3.4 Harmonic approximation

For studying the lattice vibrations harmonic approximation is a good first step. Phonons are the quantized vibrational modes of atoms in solids, which usually can be described as harmonic oscillators. A one dimensional harmonic oscillator can be written with the Hamiltonian :

$$\hat{H} = \frac{\hat{p}^2}{2m} + \frac{K\hat{x}^2}{2} \quad (3.20)$$

or

$$\hat{H} = \frac{\hbar\omega_k}{2} \left(-\frac{\partial^2}{\partial \xi^2} + \xi^2 \right) \quad (3.21)$$

where the m and K are mass and harmonic force constant ($\omega_k^2 = \frac{K}{m}$ and $\xi = x(\frac{m\omega_k}{\hbar})^{1/2}$). One solution for Eq. (3.21) is given by:

$$H\psi_n = \hbar\omega_k \left(n + \frac{1}{2} \right) \psi_n \quad (3.22)$$

Creation and annihilation operators, a and a^\dagger , can be written as :

$$a_k = \frac{1}{\sqrt{2}} \left(\xi + \frac{\partial}{\partial \xi} \right) = \sqrt{\frac{m\omega_k}{2\hbar}} \left(x + \frac{ip}{m\omega_k} \right) \quad (3.23)$$

$$a_k^\dagger = \frac{1}{\sqrt{2}} \left(\xi - \frac{\partial}{\partial \xi} \right) = \sqrt{\frac{m\omega_k}{2\hbar}} \left(x - \frac{ip}{m\omega_k} \right) \quad (3.24)$$

The amplitude of the lattice vibration on site l at time t can be given as :

$$x_l(t) = \sum_k \left(\sqrt{\frac{\hbar}{2mN\omega_k}} \right) \left(a_k e^{-i\omega_k t} + a_{-k}^\dagger e^{i\omega_k t} \right) e^{ikl} \quad (3.25)$$

The summation is over all k in the first Brillouin zone.

3.5 Introduction to electron-phonon interaction

From the *ab initio* perspective, there has been no progress in the electron-phonon coupling area, until the Density Functional Theory was well established in the early 1980s. But, the developed version of DFT, the Density Functional Perturbation Theory, (DFPT), was born in the mid of 1990s. So the majority of the theoretical studies in this field comes back to the semi-empirical model Hamiltonians, but the aim of this thesis is simply the fact that, by calculating the electron-phonon coupling and relaxation time prepare the information to establish the theoretical developments relating to the model Hamiltonians as referred to in the outstanding monographs by Ziman (1960), Grimvall (1981), Mahan (1993). In 1929, the first quantum theory of the temperature-dependent electrical resistivity of metals and the formal solutions of the Schrödinger equation of periodic potentials discussed by Bloch where the first instance of the term "electron-phonon interactions" under the title: "The interaction of the electrons and the elastic waves of the lattice" was published. After Bloch, in 1932, Frenkel replaced the Bloch's "elastic waves" by the name "phonons". The calculation of the electron-phonon coupling from first-principles is challenging because of the necessity of evaluating Brillouin zone integrals with high accuracy. Such calculations require the evaluation of matrix elements between electronic states connected by phonon wavevectors. Well-established software packages are available for computing electronic states and eigenvalues through Density-Functional Theory, as well as phonon frequencies and eigenmodes through Density-Functional Perturbation Theory. However large numbers of matrix elements may be necessary to achieve numerical convergence of the Brillouin zone integrals over these matrix elements. For example, in order to compute the electronic lifetimes associated with the electron-phonon interaction, it is necessary to evaluate a Brillouin zone integral over all the possible phonon wavevectors (thousands to millions). Since lattice-dynamical calculations for each phonon wavevector are at least as expensive as self-consistent total energy minimizations, achieving numerical convergence in the Brillouin zone integrals over the phonon wavevectors by brute force calculations may become a prohibitive computational task.

3.5.1 Historical development

Starting from the standard form of the Hamiltonian which is describing a e-ph coupling it would be useful in order to discuss about the approaches in this area:

$$\begin{aligned}
\hat{H} = & \sum_{n\mathbf{k}} \epsilon_{n\mathbf{k}} \hat{c}_{n\mathbf{k}}^\dagger \hat{c}_{n\mathbf{k}} + \sum_{\mathbf{q}\nu} \hbar\omega_{\mathbf{q}\nu} (\hat{b}_{\mathbf{q}\nu}^\dagger \hat{b}_{\mathbf{q}\nu} + \frac{1}{2}) \\
& + N_p^{-1/2} \sum_{\substack{\mathbf{k}, \mathbf{q} \\ mn\nu}} D_{mn\nu}(\mathbf{k}, \mathbf{q}) \hat{c}_{m\mathbf{k}+\mathbf{q}}^\dagger \hat{c}_{n\mathbf{k}} (\hat{b}_{\mathbf{q}\nu} + \hat{b}_{-\mathbf{q}\nu}^\dagger) \\
& + \left[N_p^{-1} \sum_{\substack{\mathbf{k}, \mathbf{q}, \mathbf{q}' \\ mn\nu\nu'}} D_{mn\nu\nu'}^{DW}(\mathbf{k}, \mathbf{q}, \mathbf{q}') \hat{c}_{m\mathbf{k}+\mathbf{q}+\mathbf{q}'}^\dagger \hat{c}_{n\mathbf{k}} \right. \\
& \left. \times (\hat{b}_{\mathbf{q}\nu} + \hat{b}_{-\mathbf{q}\nu}^\dagger) (\hat{b}_{\mathbf{q}'\nu'} + \hat{b}_{-\mathbf{q}'\nu'}^\dagger) \right].
\end{aligned} \tag{3.26}$$

In the Eq. (3.26), that is written in the form of second quantization, the first and the second terms are related to the electron and phonon description, respectively. The third and fourth

terms are related to the e-ph coupling with the first and second orders atomic displacements. N_p is the number of unit cells in the Born-von Karman (BvK) boundary conditions and the $\epsilon_{n\mathbf{k}}$ is the single particle eigenvalue for an electron with the crystal momentum \mathbf{k} in band index n . $\omega_{\mathbf{q}\nu}$ is the lattice vibration frequency with the crystal momentum \mathbf{q} . Where $D_{mn\nu}(\mathbf{k}, \mathbf{q})$ and $D_{mn\nu\nu'}^{DW}(\mathbf{k}, \mathbf{q}, \mathbf{q}')$ are the matrix elements and the strengths of the coupling between electron and phonon subsystems, respectively. The drawback of Eq. (3.26) is simply the fact that any prescription for determining the numerical parameters for matrix elements, eigenvalue of electron and the frequency of the lattice vibration can not be provided by this Hamiltonian.

3.5.2 Early approaches to the e-ph interaction in DFT

1) In *metals*: The first study returns to the free electron gas model where the electronic excitation is $\epsilon_{n\mathbf{k}} = \hbar^2 \mathbf{k}^2 / 2m_e - \epsilon_F$. The m_e , ϵ_F are electron mass and Fermi energy, respectively. From Debye mode the relation between the angular frequency, ω , and the wave vector, \mathbf{q} , is $\omega_{\mathbf{q},\nu} = v_s |\mathbf{q}|$, where v_s is the velocity of the sound wave. It looks simple but determining the matrix elements will be the challenging part. By expressing the matrix element as

$$D_{mn\nu}(\mathbf{k}, \mathbf{q}) = -i \left(\frac{\hbar}{2N_p M_k \omega_{\mathbf{q},\nu}} \right)^{1/2} \mathbf{q} \cdot \mathbf{e}_{k\nu}(\mathbf{q}) V_0,$$

where V_0 is a unit-cell average of the "effective potential". In 1929 the first approximation for this matrix element came from Bloch's model which the average potential was considered as $V_0 = \hbar^2 / (16m_e a_0^2)$, where a_0 is Bohr radius. After Bloch's model, "rigid-ion" approximation, which $V_k(\mathbf{q})$ is considered as the Fourier component of the ionic Coulomb potential instead of V_0 , but this approximation leads to unrealistic EPC. Until 1937 the effect of electronic screening was neglected. Bardeen introduced one model where the average potential, V_0 , is replaced with $V_k(\mathbf{q})/\epsilon(q)$ where the $\epsilon(q)$ is Lindhard function, which is defined by the k_{TF} and k_F are the Thomas-Fermi screening wave vector and the Fermi wave vector, respectively.

$$\epsilon(\mathbf{q}) = 1 + (k_{TF}/q)^2 F(q/2k_F)$$

and

$$F(x) = 1/2 + (4x)^{-1} (1 - x^2) \log|1 + x|/|1 - x|.$$

This strategy is similar in spirit to modern DFPT theory. One drawback in Bardeen's model in comparison to modern techniques is simply the fact that the exchange and correlation effects in the screening were neglected. But this limitation has been solved by Bardeen and Pines in 1955 and this was the first time that the electron-phonon coupling problem was addressed to use *field-theoretic* approach. In 1993 Mahan added the frequency-dependent Lindhard function in Eq. (3.26) :

$$V_0 \rightarrow V_k(\mathbf{q})/\epsilon(q, \omega_{\mathbf{q}\nu}).$$

2) In semiconductors: The theory investigation of the EPC is not restricted to metals but can also be extended to complicated systems like semiconductors. This idea was started by Bardeen and Shockley in 1950 with the "deformation potential" method. In this method atomic displacements are used to describe long-wavelength acoustic waves, which can cover

the elastic strain in the crystal. In their work the effective potential in Eq. (3.26) was replaced by

$$V_0 \rightarrow E_{1,n\mathbf{k}} = \Omega \frac{\partial \epsilon_{n\mathbf{k}}}{\partial \Omega}$$

where Ω is the volume of the unit cell. In this thesis the electron-phonon coupling was studied using the deformation potential approach.

3.6 The e-ph interaction in DFT

In this part the standard formalism for lattice vibration and electron-phonon coupling Hamiltonian will be discussed. Then a brief summation of the matrix element formalism will be presented.

3.6.1 Lattice vibrations in crystals

In this study all force constants are obtained by the phonopy [118] code, as it can provide force constants from both the Finite Displacement Method (FDM) [64, 86] and DFPT [39, 42]. In the following, the relation between the dynamical matrix, $D_{\alpha\beta}(jj', \mathbf{q})$, force constants and phonon dispersion are shown. The normal modes of vibrations of a crystal can be labeled with a wave vector \mathbf{q} and a band index ν . The cyclic boundary condition of the atomic displacements, which are densely distributed throughout the first Brillouin zone for the crystal, can be determined with wave vector (\mathbf{k}) and the indices of the atoms, j, j' , in a primitive unit cell of the crystal ($j, j' = 1, 2, \dots, n$). The squares of the $3n$ normal mode frequencies, $\omega_\nu^2(\mathbf{q})$, corresponding to a given value of \mathbf{q} are the eigenvalues of a $3n \times 3n$ Hermitian matrix, $D(\mathbf{q})$, which is called the (Fourier-transformed) dynamical matrix, where elements of $D_{\alpha\beta}(jj'|\mathbf{q})$ are labeled by the Cartesian axes ($\alpha, \beta, \gamma = x, y, z$). Displacement patterns in space of the atoms comprising the crystal when the latter is vibrating in the mode ($\mathbf{q}\nu$) can be described by the eigenvectors $\mathbf{e}_{\alpha\sigma\beta}(j|\mathbf{q}\nu)$. Starting with the potential energy the phonon system as a function of atomic positions is showing the relation between the eigenvectors (atomic displacements) and dynamical matrix:

$$V[\mathbf{u}(j_1l_1), \dots, \mathbf{u}(j_nl_n)] = V_0 + \frac{1}{2} \sum_{l_1l_2} \sum_{j_1j_2} \sum_{\alpha\beta} V_{\alpha\beta}(j_1l_1, j_2l_2) \mathbf{u}_\alpha(j_1l_1) \mathbf{u}_\beta(j_2l_2) \quad (3.27)$$

where the potential energy of the static crystal is V_0 and the j^{th} atom in the l^{th} unit cell is denoted as $\mathbf{u}(jl)$ and n and N denote the number of atoms in a unit cell and number of unit cell, respectively. The first derivative of the potential energy with respect to the corresponding atomic position is given:

$$F_\alpha(jl) = -\frac{\partial V}{\partial u_\alpha(jl)} \quad (3.28)$$

The second-order force constant ($\Phi_{\alpha\beta}$) is the second derivative of the potential energy with respect to a function of atomic positions:

$$\Phi_{\alpha\beta}(j_1l_1, j_2l_2) = \frac{\partial^2 V}{\partial u_\alpha(j_1l_1) \partial u_\beta(j_2l_2)} = -\frac{\partial F_\beta(j_2l_2)}{\partial u_\alpha(j_1l_1)} \quad (3.29)$$

A phase convention of dynamical matrix which is used in the phonopy code is as follows:

$$D_{\alpha\beta}(jj', \mathbf{q}) = \frac{1}{\sqrt{m_j m_{j'}}} \sum_{\nu} \Phi_{\alpha\beta}(j0, j'l') e^{(i\mathbf{q} \cdot [\mathbf{u}(j'l') - \mathbf{u}(j0)])}, \quad (3.30)$$

where m is the atomic mass and \mathbf{q} is the wave vector. As the dynamical matrix is hermitian and therefore admits real eigenvalues, the equation of motion can be written as:

$$\sum_{j'\beta} D_{\alpha\beta}(jj', \mathbf{q}) e_{\beta}(j', \mathbf{q}\nu) = m_j [\omega(\mathbf{q}\nu)]^2 e_{\alpha}(j, \mathbf{q}\nu),$$

where $e_{\alpha}(j, \mathbf{q})$ should be orthonormal for each \mathbf{q} :

$$\sum_{\alpha, j} e_{\alpha}^*(j, \mathbf{q}\nu) e_{\alpha}(j, \mathbf{q}\nu') = \delta_{\nu\nu'}$$

. In finite difference method, the derivatives in Eq. (3.29) can be approximated by

$$\Phi_{\alpha\beta}(j_1 l_1, j_2 l_2) \simeq - \frac{F_{\beta}(j_1 l_1; \Delta \mathbf{u}_{\alpha}(j_2 l_2)) - F_{\beta}(j_1 l_1)}{\Delta \mathbf{u}_{\alpha}(j_2 l_2)} \quad (3.31)$$

Second-order force constants are computed through the approximation of Eq. (3.31) with small displacements $\Delta \mathbf{u}_{\alpha}$ correspond to the finite atomic displacements that mean that the value is calculated under the displacements [21]. To compute the second-order force constants, we employed the technique presented by the Parlinski-Li-Kawazoe method [86], which is the relation between the force on each atom, a second-order force constant, and an atomic displacement.

3.6.2 Fröhlich Hamiltonian

The Fröhlich Hamiltonian, written in second quantization, is a good starting point on the discussion of electron-phonon coupling effects in periodic solids. In this Hamiltonian, coupling of the longitudinal acoustic phonons with the free electrons through unscreened Coulomb interactions is described. The electronic states are significantly influenced by lattice vibrations mostly in close vicinity of the Fermi energy. It is therefore appropriate to start with electrons moving in the static potential of a rigid ion lattice, without any renormalization by the lattice vibrations. On contrast, the bare vibrations of the ion lattice would be a bad starting point, because they are strongly altered by the screening of the electrons. This screening must be built into the description of the harmonic lattice vibrations which defines the noninteracting phonons.

Firstly, writing down the full Hamiltonian to clearly finding the terms, which are depending both on electrons and ions is the goal.

$$H = H_{el}^0 + H_{ph}^0 + H_{coulomb} + H_{int} \quad (3.32)$$

Here the H_{el}^0 , H_{ph}^0 , $H_{Coulomb}$ and H_{int} are defined as :

$$H_{el}^0 \approx \sum_{b, k, \sigma} E_{b, \sigma}(\vec{k}) c_{b, k\sigma}^{\dagger} c_{b, k\sigma} \quad (3.33)$$

$$H_{ph}^0 = \sum_{k\lambda} \omega_{k\lambda} \left(b_{k\lambda}^\dagger b_{k\lambda} + \frac{1}{2} \right) \quad (3.34)$$

$$H_{Coulomb} = \frac{1}{2} \sum_{kk'q} V(q) c_{k'+q\sigma'}^\dagger c_{k\sigma}^\dagger c_{k+q\sigma} c_{k'\sigma'} \quad (3.35)$$

$$H_{int} = \sum_{kk'\sigma\lambda} D_{kk'} c_{k\sigma}^\dagger c_{k'\sigma} \left(b_{-q\lambda}^\dagger + b_{q\lambda} \right) \quad (3.36)$$

where \vec{k} is the momentum which is restricted to the first BZ, and σ is the spin. λ denotes polarization and $q \equiv k' - k$ is the wave vector of the phonon, which is created by $b_{k\lambda}^\dagger$ and $D_{kk'}$ is the electron-phonon coupling constant. The electron can end up in the final state $k'\sigma$ by the absorption (emission) of a phonon of momentum \mathbf{q} , from the initial state $k\sigma$ while undergoing a scattering process with amplitude $D_{kk'}$. In general many-body Hamiltonian, the electron-ion potential around the equilibrium positions, \vec{R}_j^0 , can be written as $\tilde{V}(r_{ij})$

$$\tilde{V}_{ei} = \sum_j V_{ei}(\vec{r}_j) = \sum_{i,j} V_{ei}(\vec{r}_j - \vec{R}_i)$$

while $R_i^{(0)}$ and Q_j are equilibrium positions and displacements of atoms, respectively. The position of the atoms can be written as $\vec{R}_i = \vec{R}_i^0 + \vec{Q}_i$. A Taylor expansion for the electron-ion potential around $R_i^{(0)}$ is shown below:

$$\sum_{ij} V_{ei}(\vec{r}_j - \vec{R}_i^0 - \vec{Q}_i) = \sum_{i,j} V_{ei}(\vec{r}_j - \vec{R}_i^0) - \sum_{i,j} \vec{Q}_i \cdot \nabla_j V_{ei}(\vec{r}_j - \vec{R}_i^0) + O(Q^2) + \dots$$

The information regarding the coupling of electrons to the lattice distortion is contained in the second term, as the periodic potential seen by conduction electrons just is defined in the first term. We can go in direction of Fourier transform of e-ph potential,

$$V_{ei}(\vec{r}) = \frac{1}{N} \sum_{\mathbf{q}} V_{ei}(\mathbf{q}) e^{i\mathbf{q} \cdot \mathbf{r}} \quad (3.37)$$

and

$$\nabla V_{ei}(\mathbf{r}) = \frac{i}{N} \sum_{\mathbf{q}} \mathbf{q} V_{ei}(\mathbf{q}) e^{i\mathbf{q} \cdot \mathbf{r}} \quad (3.38)$$

For acoustic phonons, we need to evaluate the combination:

$$V_{ep}(\mathbf{r}) = \frac{i}{N} \sum_{\mathbf{q}} V_{ei}(\mathbf{q}) e^{i\mathbf{q} \cdot \mathbf{r}} \mathbf{q} \cdot \left(\sum_j Q_j e^{i\mathbf{q} \cdot \mathbf{R}_j^{(0)}} \right) \quad (3.39)$$

where $V_{ep}(\mathbf{r})$ is the potential defined as the unscreened electron-atom potential. This potential acts upon the electrons and also upon other particles such as positrons.

$$Q_i(t) = i \sum_{\mathbf{k}, \lambda} \left(\frac{\hbar}{2MN\omega_{\mathbf{k}\lambda}} \right)^{1/2} \xi_{\mathbf{k}, \lambda} (b_{\mathbf{k}, \lambda} e^{-\omega_{\mathbf{k}\lambda} t} + b_{-\mathbf{k}, \lambda}^\dagger e^{i\omega_{\mathbf{k}\lambda} t}) e^{i\mathbf{k} \cdot \mathbf{R}_i^{(0)}} \quad (3.40)$$

where the $\xi_{\mathbf{k}, \lambda}^* = -\xi_{-\mathbf{k}, \lambda}$, \mathbf{M} are polarization vector and the ion mass, respectively. By using the definition of Q_i (Eq. (3.40)), displacement from the equilibrium position, one can show :

$$\frac{i}{N} \sum_j Q_j e^{i\mathbf{q} \cdot \mathbf{R}_j^{(0)}} = \frac{i}{N} \sum_{\mathbf{G}} Q_{\mathbf{q}+\mathbf{G}} = - \sum_{\mathbf{G}} \left(\frac{\hbar}{2MN\omega_{\mathbf{q}}} \right)^{1/2} \xi_{\mathbf{q}+\mathbf{G}} (b_{\mathbf{q}} + b_{\mathbf{q}}^\dagger),$$

where the \mathbf{G} summation all over the reciprocal lattice vectors of the solid. $\mathbf{q} + \mathbf{G}$ is the phonon states within the first Brillouin zone of the solid. The \mathbf{q} labels related to phonon, which should be in the first Brillouin zone, but with the \mathbf{G} can interact with the higher Fourier components. In Modern calculation as I presented in the Chapter results, we obtain the accurate phonon energies, $\omega_{\mathbf{q}}$ and the $\xi_{\mathbf{q}}$ for each mode and use them to calculate the electron-phonon properties. By integration over the charge density $n(\mathbf{r})$ of the solid, the electron-phonon coupling will be obtained as :

$$\begin{aligned} H_{ep} &= \int d^3\mathbf{r} n(\mathbf{r}) V_{ep}(\mathbf{r}) \\ &= - \sum_{\mathbf{q}, \mathbf{G}} n(\mathbf{q} + \mathbf{G}) V_{ei}(\mathbf{q} + \mathbf{G})(\mathbf{q} + \mathbf{G}) \cdot \xi_{\mathbf{q}} \left(\frac{\hbar}{2m\nu\omega_{\mathbf{q}}} \right)^{1/2} (b_{\mathbf{q}} + b_{-\mathbf{q}}^\dagger) \end{aligned} \quad (3.41)$$

The particle density operator, $n(\mathbf{q})$, can defined as :

$$n(\mathbf{q}) = \int d^3\mathbf{r} e^{-i\mathbf{q} \cdot \mathbf{r}} n(\mathbf{r}).$$

Then the electron-phonon Hamiltonian with the help of matrix element, $M_{\mathbf{q}+\mathbf{G}}$, can be rewritten as :

$$\begin{aligned} M_{\mathbf{q}+\mathbf{G}} &= -V_{ei}(\mathbf{q} + \mathbf{G})(\mathbf{q} + \mathbf{G}) \cdot \xi_{\mathbf{q}} \left(\frac{\hbar}{2m\nu\omega_{\mathbf{q}}} \right)^{1/2} \\ H_{ep} &= \sum_{\mathbf{q}, \mathbf{G}} M_{\mathbf{q}+\mathbf{G}} n(\mathbf{q} + \mathbf{G}) (b_{\mathbf{q}} + b_{-\mathbf{q}}^\dagger) \end{aligned} \quad (3.42)$$

3.7 Density Matrix Formalism

All observables can be written in the terms of creation and annihilation operator such as total electron density, $n(\mathbf{r})$. The electronic operators, $(c_{n\mathbf{k}}^\dagger)$ and $(c_{n'\mathbf{k}'})$, and the phonon operators, $(b_{n\mathbf{k}}^\dagger)$ and $(b_{n'\mathbf{k}'})$, can be defined with the fermionic and the bosonic commutation relation, respectively:

$$[c_{n\mathbf{k}}^\dagger, c_{n'\mathbf{k}'}]_\dagger = \delta_{n, n'} \delta_{\mathbf{k}, \mathbf{k}'} \quad [b_{i\mathbf{q}}^\dagger, b_{i'\mathbf{q}'}] = \delta_{i, i'} \delta_{\mathbf{q}, \mathbf{q}'} \quad (3.43)$$

The density can be written as:

$$n(\mathbf{r}) = \sum_{n\mathbf{k}, n'\mathbf{k}'} \psi_{n\mathbf{k}}^*(\mathbf{r}) \psi_{n'\mathbf{k}'}(\mathbf{r}) \langle c_{n\mathbf{k}}^\dagger c_{n'\mathbf{k}'} \rangle \quad (3.44)$$

The expectation value of the number operators of electron and phonon are $f_{n\mathbf{k}}$ and $n_{i\mathbf{q}}$, respectively, which can be described by the probability of finding an electron in state $\psi_{n\mathbf{k}}(\mathbf{r})$ and the phonon in mode i at wavevector \mathbf{q} .

$$f_{n\mathbf{k}} = \langle c_{n\mathbf{k}}^\dagger c_{n\mathbf{k}} \rangle \quad n_{i\mathbf{q}} = \langle b_{i\mathbf{q}}^\dagger b_{i\mathbf{q}} \rangle \quad (3.45)$$

Here, the quantum mechanical expectation value is denoted by $\langle \dots \rangle$. The transitions between states can be described as $\rho_{n'\mathbf{k}'}^{n\mathbf{k}}$, which is the transition probability amplitudes.

$$\rho_{n'\mathbf{k}'}^{n\mathbf{k}} = \langle c_{n\mathbf{k}}^\dagger c_{n'\mathbf{k}'} \rangle \quad (3.46)$$

So, the Hamiltonian of the system with the help of the second quantization is given by:

$$\begin{aligned} H = & \underbrace{\sum_{n\mathbf{k}} E_{n\mathbf{k}} c_{n\mathbf{k}}^\dagger c_{n\mathbf{k}}}_I + \underbrace{\sum_{i\mathbf{q}} \hbar\omega_{i\mathbf{q}} b_{i\mathbf{q}}^\dagger b_{i\mathbf{q}}}_II \\ & + \underbrace{\sum_{\substack{n\mathbf{k} \\ n'\mathbf{k}'}} \mathbf{A}(t) \mathbf{p}_{n'\mathbf{k}'}^{n\mathbf{k}} c_{n\mathbf{k}}^\dagger c_{n'\mathbf{k}'}}_{III} + \underbrace{\sum_{\substack{n\mathbf{k} \\ n'\mathbf{k}' \\ i\mathbf{q}}} \mathbf{D}_{n'\mathbf{k}'}^{n\mathbf{k}} c_{n\mathbf{k}}^\dagger c_{n'\mathbf{k}'} (b_{i-\mathbf{q}}^\dagger + b_{i\mathbf{q}})}_{IV}. \end{aligned} \quad (3.47)$$

where, the kinetic energy of the electrons and the phonon energy are described in part I and II, respectively. $\omega_{i\mathbf{q}}$ and $E_{n\mathbf{k}}$ are the phonon frequency of mode i at wave vector \mathbf{q} and single particle electron states. The part III coupling to the electromagnetic vector potential, $\mathbf{A}(t)$ with the momentum matrix element, $\mathbf{p}_{n\mathbf{k}, n'\mathbf{k}'}$ within dipole approximation is described. The electron-phonon coupling is presented in part IV. The coupling parameters, $\mathbf{D}_{n'\mathbf{k}'}^{n\mathbf{k}}$, are composed of a q -dependent factor and it is given by Fourier transform of the electron-phonon interaction potential [102]. $D_{i\mathbf{q}}$ strongly depends on material system. For example for polar semiconductors, Fröhlich coupling dominate the interaction. In this thesis, the deformation potential approximation is employed with parameters $D_{i\mathbf{q}}$ from *ab initio* calculations.

3.7.1 Bath hypothesis

In weak excitation and generally for typical excitation conditions, it is usually a good approximation to describe the phonons close to the thermal equilibrium. In the bath hypothesis, the phonon operators are not considered as dynamical variables and are not calculated in the differential equations. For the bosonic system (phonon operators), Bose-distribution is given by :

$$\langle b_{i\mathbf{q}}^\dagger b_{i\mathbf{q}} \rangle = n_{i\mathbf{q}}(T) = \frac{1}{e^{\frac{\hbar\omega_{i\mathbf{q}}}{k_B T}} - 1} \quad (3.48)$$

where the phonon dispersion energy, Boltzmann constant and temperature are represented by $\hbar\omega_{i\mathbf{q}}$, k_B and T , respectively. As a consequence, the physically investigatable quantities

can be totally expressed in terms of the statistical population densities $f_{n\mathbf{k}}$ and $\rho_{n\mathbf{k}}^{n'\mathbf{k}'}$. In this thesis, only these diagonal parts of the density matrix are non-vanishing. For the diagonal parts, the corresponding equations for phonon-carrier dynamics for $f_{n\mathbf{k}}$ and the in-and-out scattering rates, $\Gamma_{n\mathbf{k}}^{n'}$, are given by:

$$\frac{d}{dt}f_{n\mathbf{k}} = 2 \sum_{n'} [\Gamma_{n\mathbf{k}}^{n' in} (1 - f_{n\mathbf{k}}) - \Gamma_{n\mathbf{k}}^{n' out} f_{n\mathbf{k}}], \quad (3.49)$$

where,

$$\Gamma_{n\mathbf{k}}^{n' in} = \frac{\pi}{\hbar} \sum_{\mathbf{k}, i\mathbf{q}, \pm} |D_{n\mathbf{k}, i\mathbf{q}}^{n'\mathbf{k}'}|^2 \delta(\epsilon_{n\mathbf{k}} - \epsilon_{n'\mathbf{k}' \pm} \pm \hbar\omega_{i\mathbf{q}}) \left(n_{i\mathbf{q}} + \frac{1 \pm 1}{2} \right) f_{n'\mathbf{k}'}, \quad (3.50)$$

and

$$\Gamma_{n\mathbf{k}}^{n' out} = \frac{\pi}{\hbar} \sum_{\mathbf{k}, i\mathbf{q}, \pm} |D_{n\mathbf{k}, i\mathbf{q}}^{n'\mathbf{k}'}|^2 \delta(\epsilon_{n\mathbf{k}} - \epsilon_{n'\mathbf{k}' \pm} \pm \hbar\omega_{i\mathbf{q}}) \left(n_{i\mathbf{q}} + \frac{1 \mp 1}{2} \right) (1 - f_{n'\mathbf{k}'}). \quad (3.51)$$

In this study, the phonon occupation numbers, $n_{i\mathbf{q}}$, are treated in an equilibrium case, only temperature dependent within a bath approximation (phonon in equilibrium) and it is discussed more in chapter V about $n_{i\mathbf{q}}$.

4 Surface Vibrations

One bridge between experiment and theory in different fields of physics, chemistry and biology is spectroscopy such as Raman spectroscopy which can be considered a powerful approach for testing atomic structures of surfaces, layer and interface characterization due to the variety of different sample properties which are covered by this technique. This chapter is focused on the vibrational properties of lead on a Si (111) surface in the two different phases, T4 and H3, and includes the Raman measurements compared with my first principles calculations. Here the relation between the atomic surface structure for the $\sqrt{3} \times \sqrt{3}$ reconstruction, striped incommensurate (SIC) phase and the Raman spectroscopy of Pb on Si (111) is discussed. Comparing the data from DFT calculations and Raman spectra from experiments helps to achieve better understanding about the discrimination of these two phases, T4 and H3.

4.1 Introduction

Different structural characterization methods are existing such as TEM (Transmission Electron Microscopy), SIMS (Secondary Ion Mass Spectroscopy), high resolution X-ray diffraction, Luminescence techniques. Beside all these methods, Raman spectroscopy which is inelastic light scattering, is extremely well suited for identifying reacted layers and interfaces and the variety of different sample properties which are covered by this technique. Furthermore one can analyse the lattice dynamics through scattering by phonons. Last but not least the interface modes can be used to analyze the layer thicknesses and interface sharpness. To study intriguing electronic phenomena in low dimensional systems, like, spin density waves or Peierls-driven metal insulator transitions [108], metallic adlayers on semiconducting templates offer an excellent working ground. One such system is Pb:Si(111), and it has lead to in-depth research for the past two decades, due to the non-misability of the two elements resulting in atomically sharp interfaces [111]. In the recent theoretical study, [129], the effect of Pb layer thickness on the phonon band structure and the electron-phonon coupling was shown. Another advantage of Pb:Si(111) is that it facilitates in making of 2D quantum films as well as various 2D and quasi-2D electron gases with tunable potentials [112]. The layers of lead on Si(111) are electronically disconnected from the substrate and show a movement regime of 1D, if grown on vicinal templates [116] as 2D ribbons, which allow for the study of growth modes triggered by quantum well states, Rashba-splitting [28, 115] caused by spin-orbit coupling, and vicinal proximity effects of superconducting state of Pb islands [33]. The particular importance of electron-phonon coupling was revealed, when in 2D Pb monolayer phases, like the densely packed so-called striped incommensurate (SIC) phase on Si(111), superconductivity was reported [15, 131]. It was put forth that the Pb-Si-interface phonons dictate the electron-phonon interactions, as in the lead monolayers, the superconducting properties are different from multilayers ($\geq 2\text{ML}$) [131]. A large range of superstructures is hosted by the wetting layer regime of Pb:Si(111) and form chainlike linear phases to hexagonal phases, inside the so-called *devil's staircase* regime from 1.20 -

1.33 ML [20, 105, 112, 127].

The generation of these superstructures is due to two structural patterns : the $(\sqrt{7} \times \sqrt{3})$ unit cell and the $(\sqrt{3} \times \sqrt{3})$ unit cell indicating the spread of $\frac{6}{5}$ ML and $\frac{4}{3}$ ML, respectively [112, 127]. A large amount of attention has been given in the last few decades [37, 66, 105, 122] for the clarification of the atomic structure of the unit cells.

Two unique local structures (H3 and T4) [112] are put forth (Fig. 4.3) for the $(\sqrt{3} \times \sqrt{3})$ reconstructions. The difference in the total energies between the two structures is less than 0.01 eV per (1×1) [20, 94] unit cell based on DFT calculations, which may lead to creation of superstructures consisting of various coexisting local structures. The SIC phase is most probably consisting of H3 and T4 structures. But difficulty remains in obtaining details on surface structures through experimental evidence, in particular on multidomain surfaces, as there appears only minute differences between T4 and H3 models in simulated scanning tunneling microscopy images [20]. The focus of this chapter is on surface vibrations and their linkage to the atomic structure of lead on the Si(111) $(\sqrt{3} \times \sqrt{3})$ reconstructed SIC phase. In the previous study by Esser and coworkers [34, 72] the monolayer structure is investigated with the help of surface Raman spectroscopy (SRS) with the aim of revealing the surface local vibrational properties, similar to fingerprint spectra of molecules. The observed Raman lines can be attributed to surface phonon eigenmodes through the combination of SRS from the work of Dr.Esser et. al. and Density Functional calculations (our calculations) [110] and thus facilitate the establishment of a link directly to the surface atomic structure [35, 72, 109].

4.2 Theory of Raman Spectroscopy

Dealing with the analysis of inelastic light scattering processes, which is an energy transfer between the incident light and the sample, Raman spectroscopy can be considered as an energy-(loss or gain) spectroscopy by using photons. Understanding better the formalism of the scattering process light can be described in a microscopic quantum mechanical perturbation theory, which is represented as :

- a) creation of an electron-hole pair due to the incidence of a photon with $\hbar\omega_i$ through transition from the ground state $|e\rangle$ to and excited state, $|e'\rangle$,
- b) electronic transition due to creation of a phonon with energy $\hbar\Omega$, such as electronic transition from $|e\rangle$ to a different excited state $|e'\rangle$.
- c) By emission of a photon with energy of $\hbar\omega_s$, the electron comes back to the ground state from the $|e'\rangle$ state.

$$\hbar\omega_s = \hbar\omega_i - \hbar\Omega_j. \quad (4.1)$$

where the ω_i : incident-light frequency; ω_s : scattered-light frequency; Ω_j : eigenfrequencies of elementary excitations.

4.2.1 Experiment

The experimental details can be found in [110]

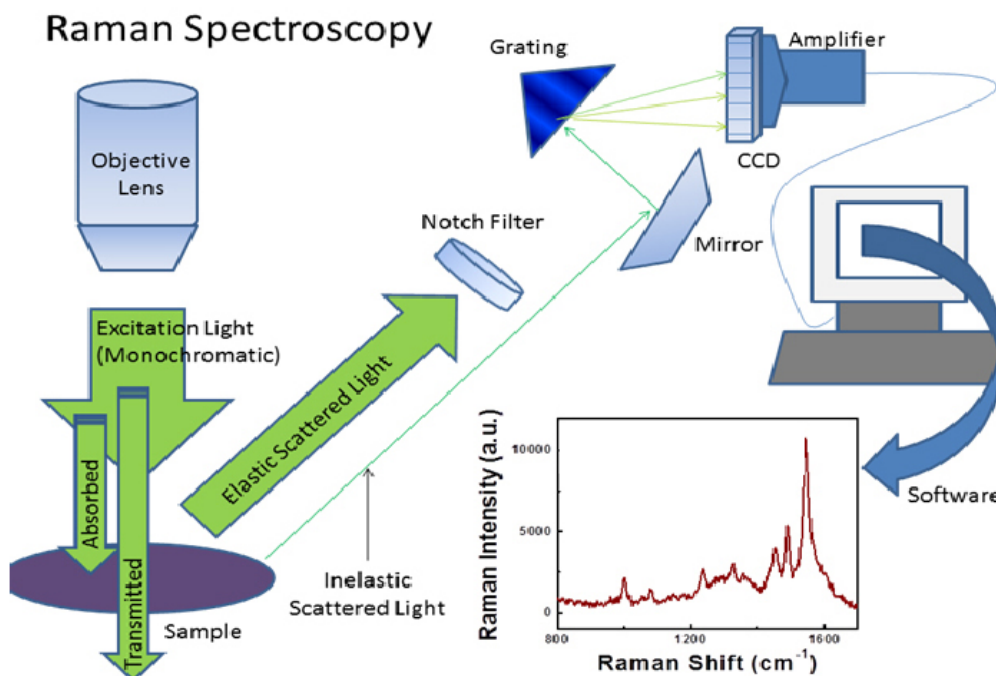


Figure 4.1: Schematic for process involved in collecting Raman spectra. The majority of scattered light is elastically scattered, meaning it has the same wavelength as the excitation source [44]

4.2.2 Basic Principles

Raman spectroscopy was carried out at a sample temperature of 50K in near back-scattering configuration. Back-scattering geometry is one of the possible configurations in which a Raman scattering experiment can be carried out. In this geometry, the axes of the propagation of the incident and scattered light is the same but their senses are opposite. On the other hand, the propagation and polarization of the incident and scattered light must be orthogonal:

$$\begin{aligned} k_i &= -k_s \\ k_i \perp E_i \quad , \quad k_s \perp E_s \end{aligned} \quad (4.2)$$

A laser excitation of 1.91eV (647.1nm) was chosen in resonant condition to the surface electronic band structure [99]. The spectral resolution of the Raman spectrometer, as verified by plasma lines, was 1.2 cm⁻¹. The experimental accuracy of the spectral lines is determined to <0.5 cm⁻¹.

4.2.3 Porto's Notation

A way to indicate the configuration of the Raman scattering experiment is Porto's notation, in which the orientation of the crystal is expressed with respect to the polarization of the laser in both the excitation and analysing directions. The notation of Porto, for Raman

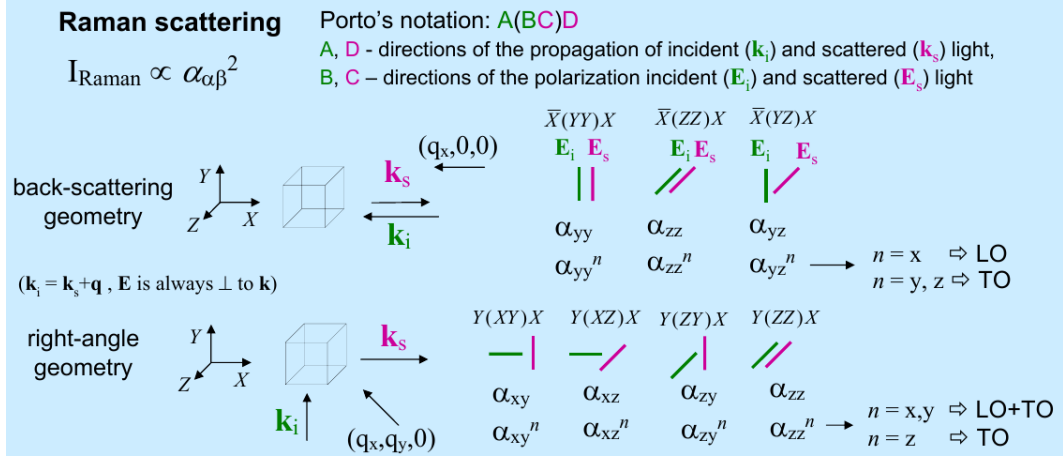


Figure 4.2: Porto's notation in back-scattering geometry and right-angle geometry [78].

scattering processes, consists of four letters:

$$A(BC)D$$

- A \equiv The direction of the propagation of the incident light (k_i).
- B \equiv The direction of the polarization of the incident light (E_i).
- C \equiv The direction of the polarization of the scattered light (E_s).
- D \equiv The direction of the propagation of the scattered light (k_s).

As shown in Fig. (4.2), A and D are the direction of the propagation of incident (k_i) and scattered (k_s) light, and B, C are directions of the polarization of the incident (E_i) and scattered (E_s) light.

In this chapter, the Raman spectra were recorded for different polarization configurations, i.e. either parallel or crossed polarizations of incident and scattered light, denoted as $\mathbf{z}(\mathbf{yy})\bar{\mathbf{z}}$ (A' symmetry) and the $\mathbf{z}(\mathbf{xy})\bar{\mathbf{z}}$ (A'' symmetry) polarization configurations (Porto notation). Assuming a C_{3v} -symmetry of the Pb/Si(111) ($\sqrt{3} \times \sqrt{3}$) structure, A' modes are symmetry conserving while A'' are symmetry breaking modes of the individual structures. For the Pb/Si(111) structure in the present work, however, the C_{3v} -symmetry applies only approximately, according to the calculated geometries.

4.3 First-principles Calculations

Here Density Functional Theory is used to calculate the phonon frequencies and displacement vectors of the Pb modes from first principles for comparison with the experimental results which are obtained by collaboration with the group of Prof. Esser [110]. The generalized gradient approximation (GGA) exchange-correlation functional [87] and the projector augmented wave method [10] are implemented in the software package VASP [63]. The valence

electrons $3s3p$ and $5d6s6p$ are included in the pseudopotentials of Si and Pb, respectively and the wavefunctions are expanded in a plane-wave basis set up to an energy cut-off of 400 eV. The effect of spin-orbit coupling and the spin degree of freedom was not considered at the Pb atoms as in the Ref. [106], it has been observed that the vibrational peak positions undergo only minor shifts when spin-orbit interactions are taken into account. The Si lattice constant is obtained as 5.47 Å, according to these settings, which is 0.7% larger than the experimental value.

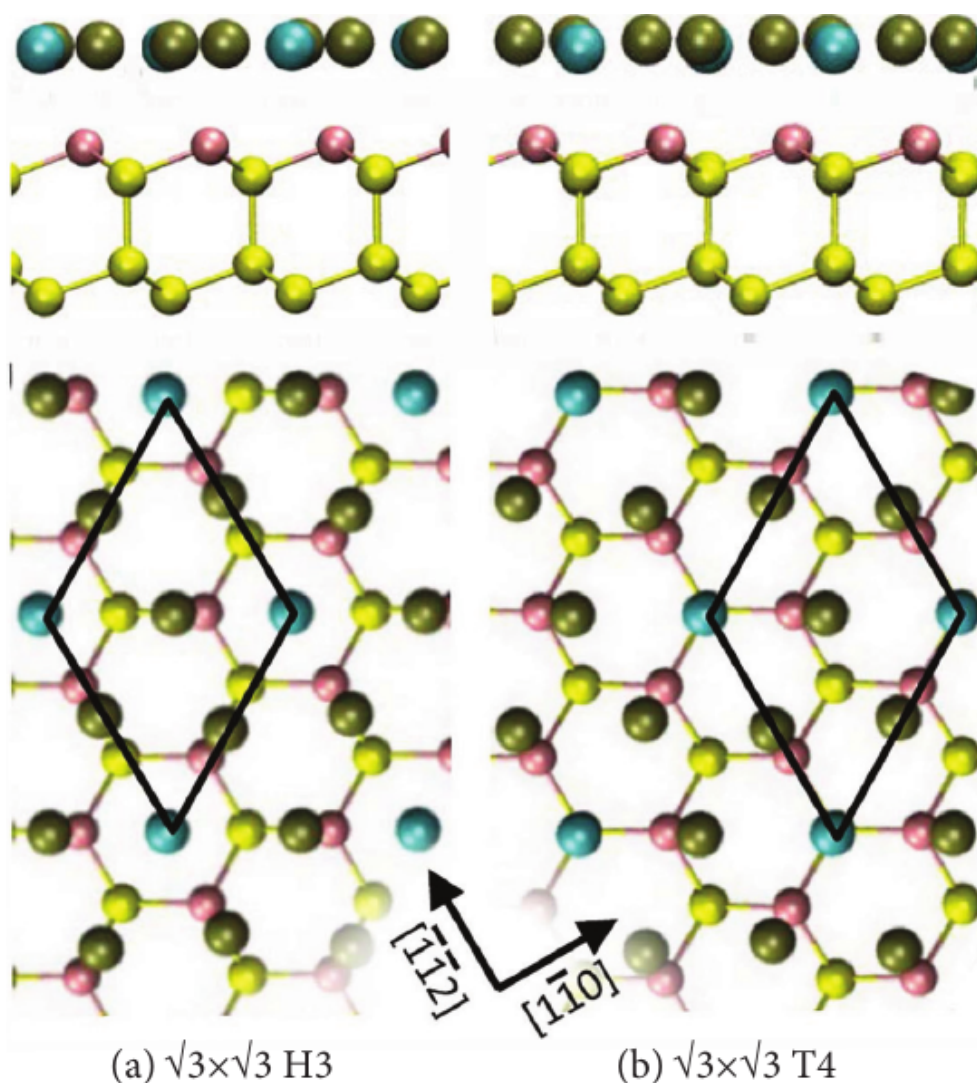


Figure 4.3: (Color online) Side (on top) and top views (bottom) of the structure models for the $(\sqrt{3} \times \sqrt{3})$ reconstructions of Si(111)-Pb [20]. Si substrate atoms are indicated in yellow (second layer) and magenta (first layer). Three Pb atoms (olive) saturate the Si dangling bonds by adsorbing on top of first layer Si atoms (T1, magenta), while one Pb atom (light blue) adsorbs above a second layer Si atom (T4, yellow) or above the hollow site (H3). The respective unit cells are labeled T4 or H3 according to the adsorption site closest to the central Pb atom. The corresponding unit cells (solid rhomboid) are indicated.

The possible strain relief in the SIC phase due to the coexistence of different domains is neglected through separate modelling of T4 and H3 structures. In contrast to Ref. [99], a thicker slab (7 bilayers) is used to model the Si substrate. Also in the relaxation of the atomic positions, the C_{3v} symmetry is no longer maintained, as the positions of T4 atoms have moved away from the three-fold rotational axis. With the use of Density Functional Perturbation Theory (DFPT), (which is explained in chapter 3), the force constants, and hence the phonon frequencies and eigenvectors at $\bar{\Gamma}$ for both structures are obtained in this thesis from the surface unit cells, Fig. 4.3. The static dielectric response is calculated using the same method and the tensor $Z_{\alpha\beta}$ of the Born effective charges is determined for each atom. The first derivative of the Cartesian component P_j of the polarization with respect to the ionic coordinate u_i represents each component of the tensor Z_{ij} . In case of non-resonant Raman scattering, Placzek's approximation (see Ref. [13] for a derivation) expresses the Raman tensor via the electronic polarizability tensor. The polarizability in connection with a specific phonon mode is calculated within the dipole approximation from the Born effective charges of the atoms involved in the displacements.

Macroscopic dielectric properties and Born effective charge tensors in VASP code are calculated for the ground state of an insulating system under the application of a finite homogeneous electric field. The VASP code implementation closely follows the approach of Nunes and Gonze [84]. Shortly one can say this approach is determining the ground state of an insulating system under the application of a finite homogeneous electric field \mathcal{E} , VASP solves for the field-polarized Bloch functions $\{\psi^{(\mathcal{E})}\}$ by minimizing the electric enthalpy functional:

$$E[\{\psi^{(\mathcal{E})}\}, \mathcal{E}] = E_0[\{\psi^{(\mathcal{E})}\}] - \Omega \mathcal{E} \cdot \mathbf{P}[\{\psi^{(\mathcal{E})}\}], \quad (4.3)$$

where $\mathbf{P}\{\psi^{(\mathcal{E})}\}$ is the macroscopic polarization as defined in the "modern theory of polarization"

$$\mathbf{P}\{\psi^{(\mathcal{E})}\} = -\frac{2ie}{(2\pi)^3} \sum_n \int_{BZ} d\mathbf{k} \langle u_{nk}^{(\mathcal{E})} | \nabla_k | u_{nk}^{(\mathcal{E})} \rangle \quad (4.4)$$

and $u_{nk}^{(\mathcal{E})}$ is the cell-periodic part of $\{\psi^{(\mathcal{E})}\}$. Adding a corresponding term to the Hamiltonian

$$H[\{\psi_{nk}^{(\mathcal{E})}\}] = H_0[\{\psi^{(\mathcal{E})}\}] - \Omega \mathcal{E} \cdot \frac{\delta \mathbf{P}[\{\psi^{(\mathcal{E})}\}]}{\delta \langle \{\psi^{(\mathcal{E})}\} |} \quad (4.5)$$

allows one to solve for $\{\psi^{(\mathcal{E})}\}$ by means of a direct optimization method. At first the zero-field ground state of the system is determined, and subsequently the program switches on the electric field and computes the field-polarized ground state orbitals. Additionally, from the change in the macroscopic electronic polarization due to the applied electric field, (part of) the components on the diagonal of the ion-clamped static dielectric tensor (ϵ_∞) are calculated, in accordance with:

$$\epsilon_{ii}^\infty = 1 + \frac{4\pi}{\epsilon_0} \frac{\partial \mathbf{P}_i}{\partial \mathcal{E}_i}, \quad i = x, y, z. \quad (4.6)$$

This option is only useful if one is interested in selected components on the diagonal of the ion-clamped dielectric tensor (for instance, in cubic systems). In the calculation, the

first steps correspond to the calculation of the zero-field groundstate. After reaching to the groundstate, the k -point mesh is regenerated using a set of symmetry operations, which takes into account that the symmetry of the system is possibly reduced by the applied electric field. In most cases the new set of k -points is larger than the original one. The orbitals at the additional k -points are generated from their symmetry equivalent counterparts in the zero-field case. This expanded set of orbitals is now reoptimized until convergence is better, and the initial electronic polarization is computed. Then the electric field is switched on, and the field-polarized groundstate is calculated. From the change in the electronic dipole moment due to the electric field VASP computes (part of) the components on the diagonal of the ion-clamped static dielectric tensor. The Born effective charge tensors can be written as :

$$Z_{ij}^* = \frac{\Omega}{e} \frac{\partial \mathbf{P}_i}{\partial \mathbf{u}_j} \quad i, j = x, y, z \quad (4.7)$$

Overall, the Raman intensity is given by [59]:

$$I \sim \sum_i \left| \sum_l \sum_j Z_{ij}^* e_i(l) \right|^2 \quad (4.8)$$

where the tensor of the Born effective charges is given by Z_{ij} and $\vec{e}_i(l)$ is the eigenvector belonging to phonon mode l , and the summation runs over i and j , the Cartesian coordinates of all atoms. Only the in-plane components x and y are summed over, as the electric field vector of the light lies in the surface plane, meaning the calculation averages over Raman contributions with A' and A'' symmetry. It is to be noted in this thesis however, that this theoretical approach to calculate Raman lines delivers limited accuracy with respect to intensities of experimental lines due to the neglect of electronic resonance effect [34, 36]. The displacement patterns of T4 and H3 structures reported in Ref.[99] and [106] are very useful with respect to assignment of modes. Due to the direction-dependent interaction between the Pb atoms and the surface Si atoms, the optical phonons of the Pb:Si(111) surface are found at significantly higher energies in comparison to the phonons in bulk lead. This trend, observed previously in DFT-LDA calculations [52, 83] is conformed with this present study.

4.4 Discussion of theoretical and experimental point of view

Polarized Raman spectra of the $(\sqrt{3} \times \sqrt{3})$ Pb/Si(111) surface are shown in Fig. 4.4 for the $\mathbf{z}(\mathbf{yy})\bar{\mathbf{z}}$ (A' symmetry) and the $\mathbf{z}(\mathbf{xy})\bar{\mathbf{z}}$ (A'' symmetry) polarization configurations. The surface vibrational contributions (surface Raman spectra) are clearly evident in the difference of spectra recorded on the clean reconstructed and the disordered reference surface. The experimentalists compared the spectra of the samples to those of a disordered reference surface to identify the surface Raman peaks. By curve fitting with Voigt line profiles after background subtraction (Fig. 4.5) our experimental colleagues extracted the surface Raman spectra for both polarization configurations (Tab. 4.1). Both scattering configurations show the surface Raman modes, but exhibit different intensities in A' and A'' mode symmetries, which validates assigning the Raman lines to surface vibrational eigenmodes. The surface Raman spectra show only the zone center modes [34, 72] in case of an ordered surface structure, and so

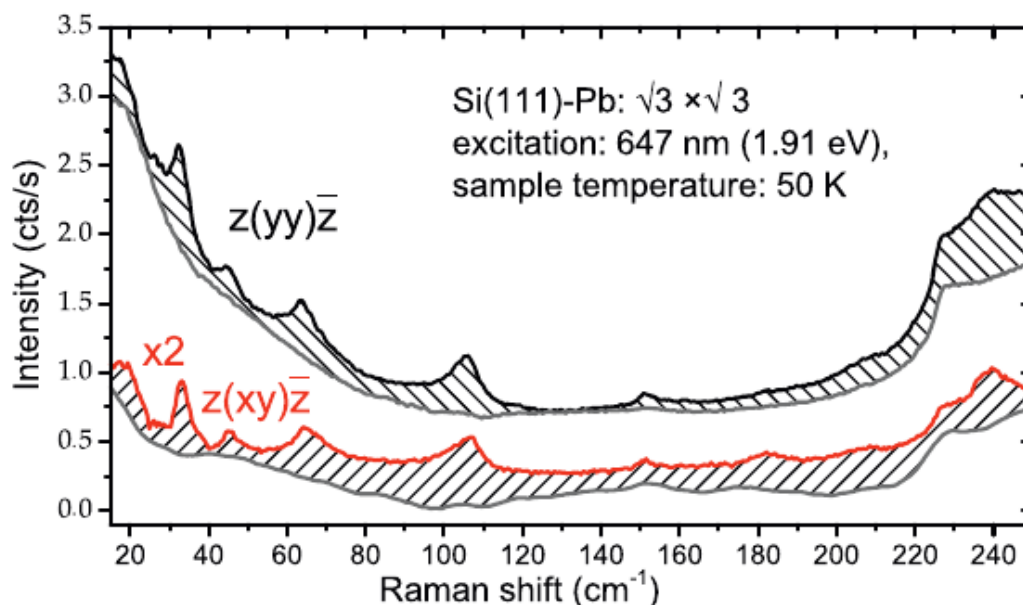


Figure 4.4: (Color online) SRS spectra of the $(\sqrt{3} \times \sqrt{3})$ reconstructed Si(111)-Pb surface and the non-ordered reference surface (gray) in parallel and perpendicular polarization configurations $\mathbf{z}(\mathbf{y}\mathbf{y})\bar{\mathbf{z}}$ (A' symmetry, black) and $\mathbf{z}(\mathbf{x}\mathbf{y})\bar{\mathbf{z}}$ (A'' , red). The intensity difference between reconstructed and reference surface (shaded area) reveals the surface response [110].

the experimental surface Raman spectra according to calculated zone center modes for both H3 and T4 structures (as shown in Fig. 4.5) will be discussed here. For the T4 structure a very complete picture including phonon dispersion, degree of surface localization, mode displacement patterns and density of phonon states is available from previous calculations [99]. Due to the large difference in atomic masses of Pb and Si, surface vibrations involving Pb displacements appear at low frequencies, while Si related vibrations appear at higher frequencies. Displacement patterns of the individual modes calculated in this thesis based on the seven bilayer slab are shown in Figs. 4.6 and 4.7. Dependence of the layers on one another can be observed only in the modes below 15cm^{-1} , which are experimentally almost inaccessible, and the corrugated potential of the Si surface leads to observable changes in the vibrational frequencies of the Pb layer. The types of surface vibrational modes for both H3 and T4 structural modes can be classified depending on the above mentioned dependency and mode displacement patterns in Figures 4.6 and 4.7 as : (see also Tab. 4.1):

The splitting of the degenerate mode, in case of enforced symmetry, results in modes appearing in groups, because the ground-state atomic structure slightly deviates from the C_{3v} symmetry. But due to the minuteness of the splitting ($< 1\text{cm}^{-1}$) it is not reflected in the measurements, in any case, it is to be noted that the spectral range up to 15cm^{-1} is not achievable by Raman spectroscopy caused by the overlapping elastically scattered laser light. Low-frequency Raman with an approximate maximum of up to 95cm^{-1} are connected

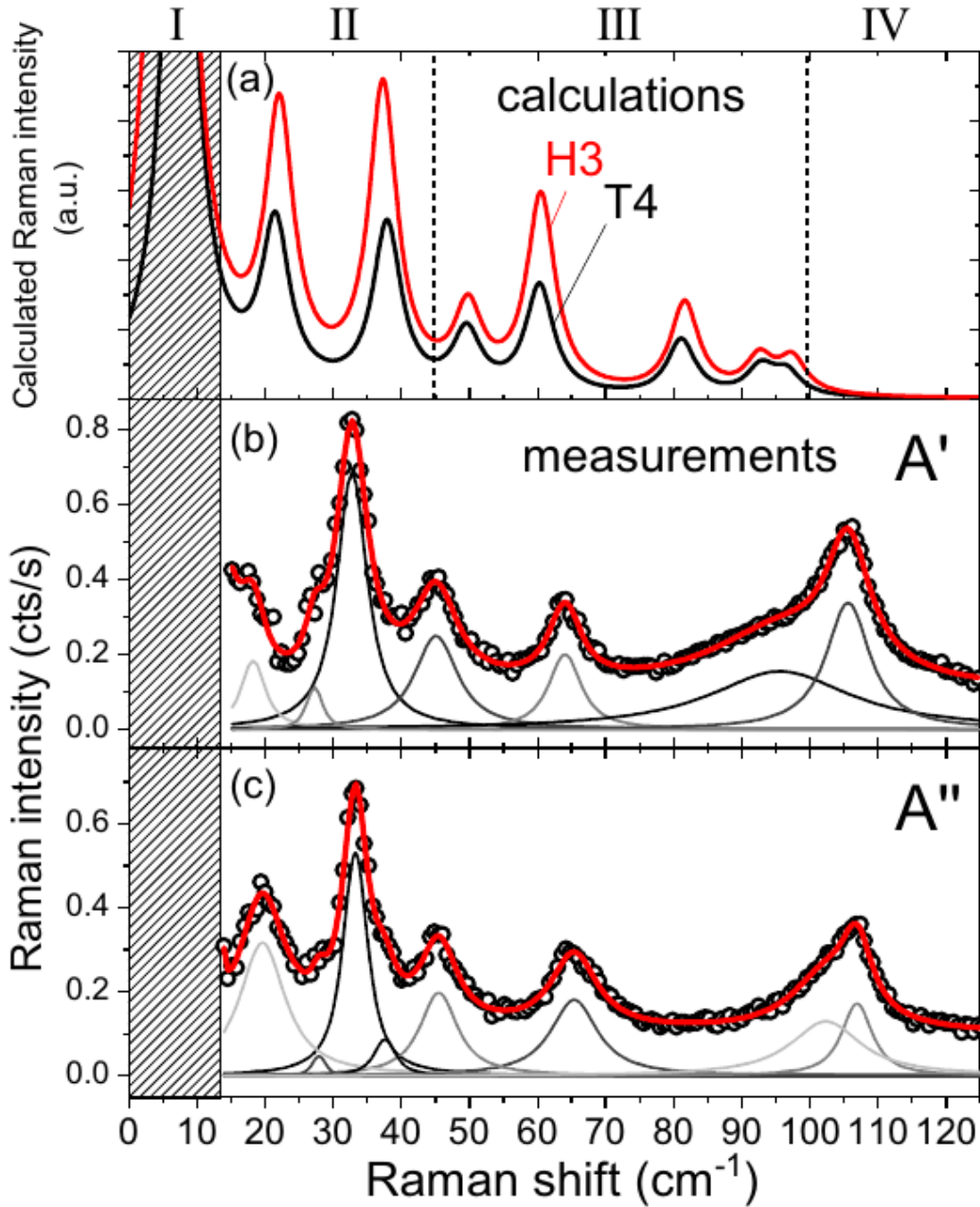


Figure 4.5: (Color online) Low energy Raman spectra of the $(\sqrt{3} \times \sqrt{3})$ reconstruction in A' and A'' symmetries in comparison to a calculated Raman spectra from phonon modes at the Brillouin zone center of both the T4 and H3 structures. The calculated spectrum consists of Lorentzian peaks broadened by 5 cm^{-1} . The calculated vibrational eigenfrequencies of T4 and H3 zone center modes are listed in Tab. 4.1. Measured spectra (open circles in (b) and (c)) are fitted by Voigt line profiles and the according peak positions also listed in Tab. 4.1 (b) and (c) from [110].

- I - in-plane sliding vibrations of the whole Pb adlayer below 15cm^{-1} ;
- II - out-of-plane vibrations with perpendicular displacements of the Pb adatoms in the range between $15 - 45\text{cm}^{-1}$;
- III - in-plane modes with combined displacements of both Si and Pb atoms between $45 - 95\text{cm}^{-1}$;
- IV - Si substrate related vibrations at higher frequencies i.e. above 95cm^{-1} .

to surface localized eigenmodes and therefore dependent in particular on the surface atomic structure, while the higher frequency modes are silicon substrate related vibrations. Table 4.1 shows a compilation of experimentally determined Raman frequencies and line widths together with the calculated modes (at $\bar{\Gamma}$) for T4 and H3. We would like to note that both the A' and A'' mode are expected to be active in both the T4 and the H3 structures, albeit with different intensities. The displacement patterns of the respective modes are shown in Figures 4.6 and 4.7 for the T4 and H3 structures, respectively. Due to stray light, in plane sliding vibrations, calculated for T4 and H3 ($7.1/7.7$ and $5.9/6.5\text{ cm}^{-1}$, respectively), can not be observed experimentally. In the range II of out-of-plane vibrations with perpendicular displacements of the Pb adatoms, calculated surface mode arise at 21.5 and 37.9 for T4 and 22.1 and 37.3 cm^{-1} for H3. For H3, such out-of-plane modes have been reported at 26 and 41 cm^{-1} recently [106] which corroborates our results. They refer to Raman lines at $18.2/19.6\text{ cm}^{-1}$, $27.3/27.9\text{ cm}^{-1}$ and $32.8/33.2\text{ cm}^{-1}$ found by curve fitting of the polarization resolved difference spectra. The line width of these modes varies between 4.8 and 9.6 cm^{-1} , indicating that the broad peaks are most probably a superposition of a number of eigenmodes, as expected from calculations.

In the range III of in-plane modes with combined displacements of Si and Pb, calculated surface mode arise at 49.6 and 60.3 for T4 and 49.8 and 60.5 cm^{-1} for H3. They refer to Raman lines at $45.1/45.5\text{ cm}^{-1}$, $64.0/65.4\text{ cm}^{-1}$ found by curve fitting of the polarization resolved difference spectra. The line width of these lines varies between 7 and 10 cm^{-1} , which indicates that they are also most likely a superposition of several eigenmodes. Moreover, calculated surface modes arise at 81.5 and 92.8 for T4 and at 81.6 and 92.2 cm^{-1} for H3. In the Raman spectra there appears a very broad band in the according spectral range which indicates the existence of surface modes but does not allow for a particular mode assignment.

In the range IV at frequencies higher than 95cm^{-1} vibrational modes of the Si substrate layers occur which lead to very broad Raman bands. These modes are not well represented within the finite slab geometry applied in the calculations. However, these modes do not depend sensitively on the surface structure since they are no surface confined modes.

Altogether, the calculated H3 and T4 surface phonon modes give a very detailed interpretation of the experimentally observed surface Raman modes. Most of the calculated surface vibrational modes fit very well, i.e. within $3\text{-}5\text{ cm}^{-1}$, to the Raman lines. Taking into account that the calculations are based on model structures which neglect the strain relief due to the coexistence of different domains in the SIC phase, the agreement between experiment and theory is very satisfactory. The comparison between experiment and theory thus allows us

Table 4.1: Compilation of calculated Γ -point vibrations in T4 and H3 structures and measured A' and A'' modes. The FWHM of measured lines is indicated in parenthesis. The confidence interval of frequency positions ($<0.5 \text{ cm}^{-1}$) is well below the specified line widths.

mode class	T4 (cm^{-1})	H3 (cm^{-1})	Exp. A' (cm^{-1})	Exp. A'' (cm^{-1})
I. in plane sliding	7.1	5.9	–	–
	7.7	6.5		
II. mixed out-of-plane	21.5	22.1	18.2 (4.8)	19.6 (9.6)
	37.9	37.3	32.8 (6.3)	33.2 (4.8)
III. in plane optical	49.6	49.8	45.1 (9.2)	45.5 (7.8)
	60.3	60.5	64.0 (6.8)	65.4 (10)
	81.5	81.6	–	–
	92.8	92.2	96 (>10)	102 (>10)
IV. substrate surface resonance			106 (>10)	107 (>10)

to identify the type and even the atomic displacements of Pb/Si/111) surface modes. Only the two highest-energy surface optical modes around $81.5/81.6 \text{ cm}^{-1}$ and $92.8/92.2 \text{ cm}^{-1}$ cannot be resolved individually due to a very large linewidth in the respective Raman band.

In spite of the very good overall agreement between experiment and theory, however, it is impossible to distinguish between the two adsorption geometries H3 and T4 in the SIC phase, since the related calculated eigenmodes are much too close in eigenfrequency.

The differences between experimental and calculated Raman spectra are larger than those between calculated H3 and T4 spectra.

As stated before we conclude that the Pb adlayer is relatively weakly bound to the Si substrate, in accordance with the large binding distance between Pb and Si. Thus, the strong bonding within the Pb adlayer on the one hand and the structure of the uppermost few Si lattice planes dominates the vibrational spectrum, while the difference in registry between T4 and H3 adlayers and the Si substrate yields only a small correction to mode frequencies. Moreover, we would like to remind that the Pb adlayer is not commensurable with the Si substrate, again in agreement with our view of a weakly bound adlayer structure and the finding of a very weak polarization dependence of Raman spectra.

The accuracy of the Raman calculations is limited on the one hand due to the finite slab geometry and the assumption of nonresonant conditions. On the other hand the assignment of Raman lines to surface phonon modes at the Brillouin zone center is strictly correct only in ideally periodic structures. In the calculations, strain and grain boundaries (idealized model surface structures are used in the calculation) are neglected. Modes with finite \mathbf{k} -

vectors may be activated in Raman scattering by the structural disorder, as realized for instance in a T4/H3 multi-domain surface structure. However, as evident from the calculated dispersion relation [99, 106], most of the surface localized modes employ rather flat dispersion branches. Thus it is justified to assume that the dominant part of the Raman signal of the surface confined modes is related to the $\bar{\Gamma}$ frequencies. Nevertheless, the line shape of the Raman lines, in particular, should carry additional information about domain size and domain distribution, similar as it is known for nanocrystalline materials. This on the one hand limits the present degree of agreement between Raman lines and calculated modes from the model structures, but on the other hand has the potential to extract more structural information with future capabilities.

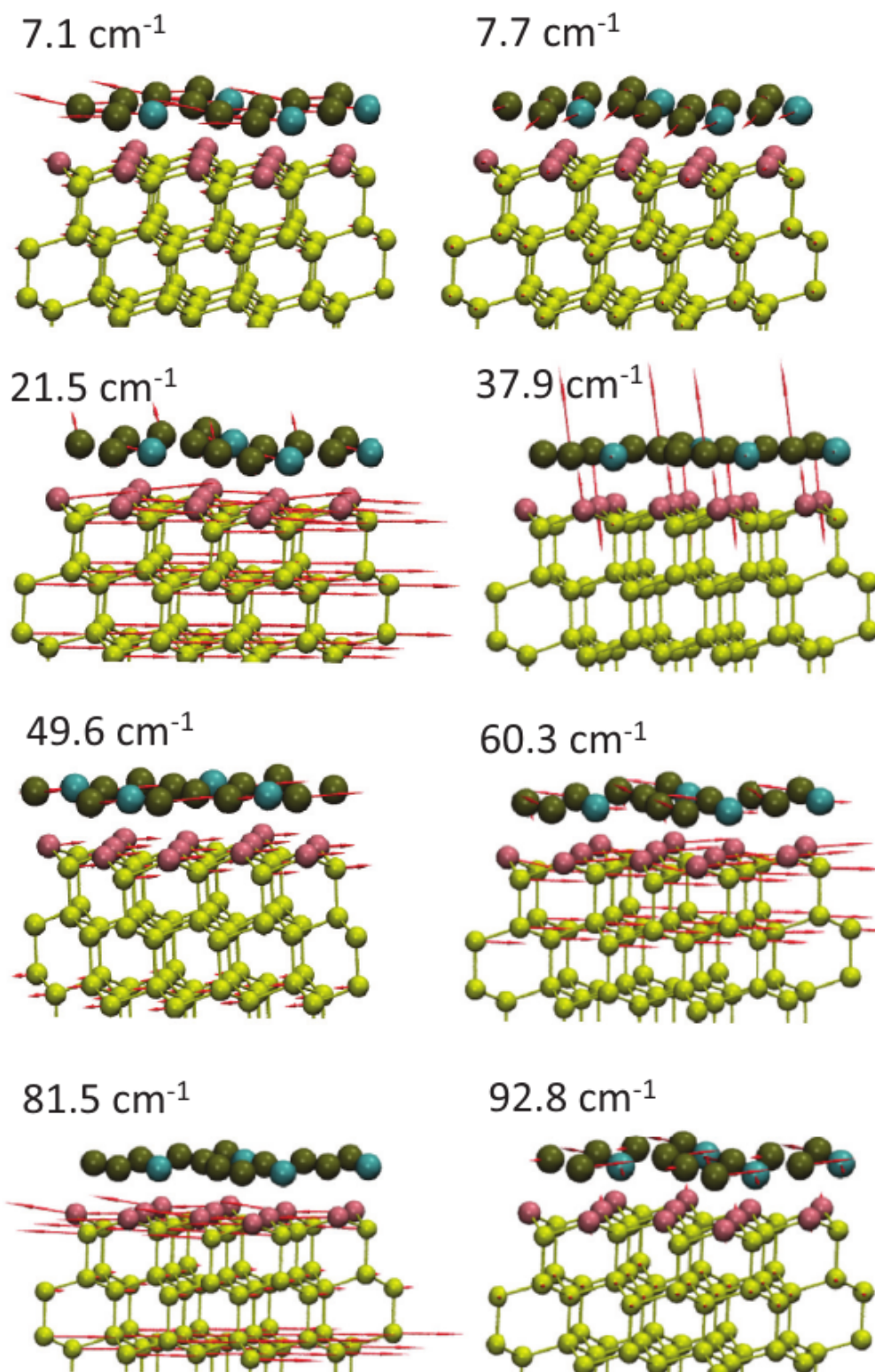


Figure 4.6: (Color online) Calculated vibrational patterns of the $(\sqrt{3} \times \sqrt{3})$ T4 reconstruction. The lengths of the arrows are proportional to the contribution of each atom to the eigenvector of the dynamical matrix. For the modes at 21.5, 37.9 and 60.3 cm^{-1} , one representative of three nearly degenerate eigenvectors is shown, while the mode at 49.6, 81.5 and 92.8 cm^{-1} are doubly degenerate.

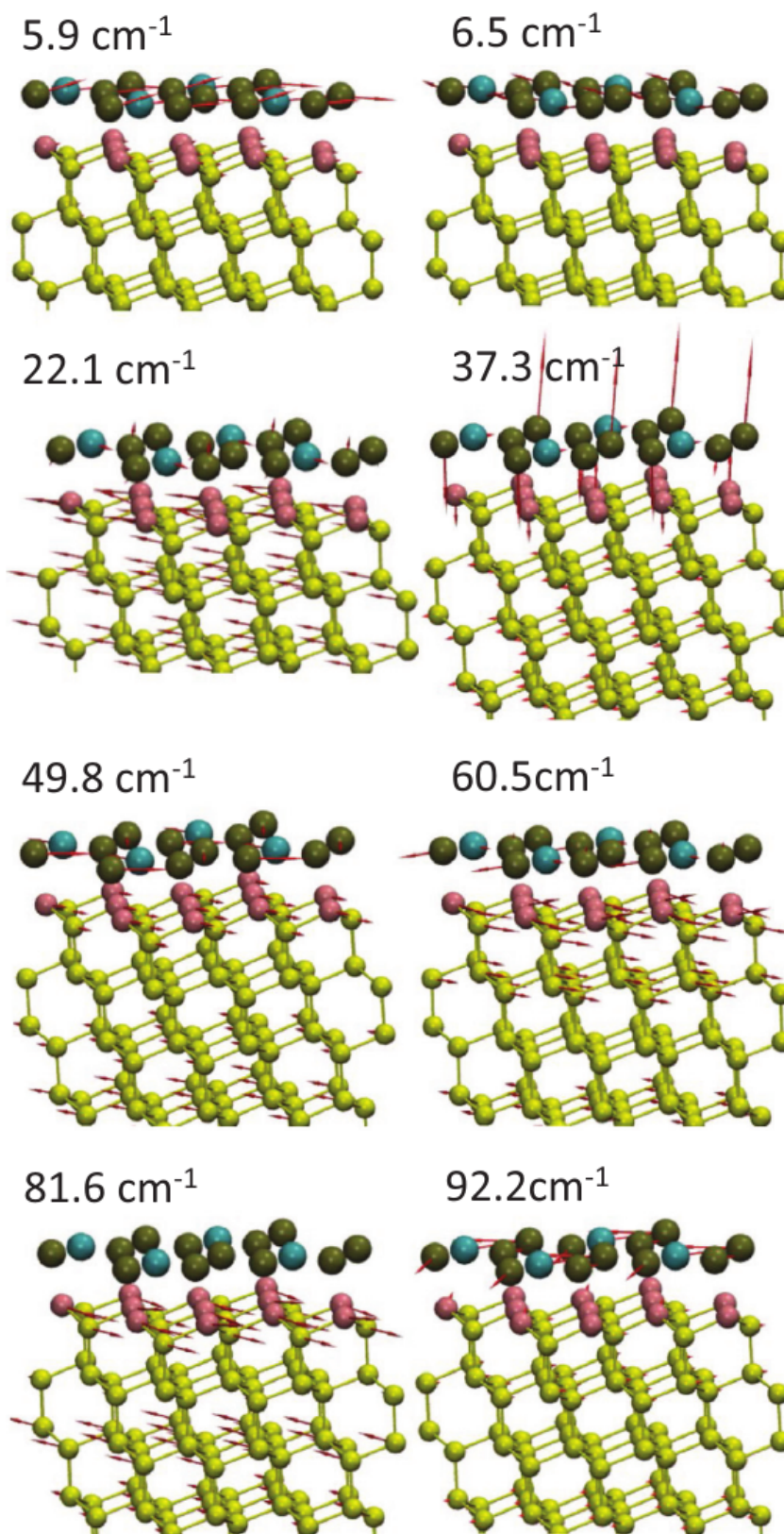


Figure 4.7: (Color online) Calculated vibrational patterns of the $(\sqrt{3}\times\sqrt{3})$ H3 reconstruction. For the modes at 22.1, 37.3 and 60.5 cm^{-1} , one representative of three nearly degenerate eigenvectors is shown, while the mode at 49.8, 81.6 and 92.2 cm^{-1} are doubly degenerate.

5 Electron-phonon coupling in the weakly correlated system Pb:Si(111)

One example, which offers a suitable probing ground for studying the competition between the relaxation mechanisms of electron-electron and electron-phonon scattering is quantum well states (QWS) in thin Pb films. In this thesis, for the first time, the electronic band structure of the Si(111) with the $\sqrt{3} \times \sqrt{3}$ reconstruction is considered to model the thin films metal, (Pb), including the Si as substrate and identify quantum well states, (QWSs), for film thicknesses between 3 and 6 ML with the help of density functional theory. Till now scientists just consider a simple model which is (1×1) unit cell for investigation of QWSs on semiconductor such as Si(111). In addition, phonon spectra and matrix elements for electron-phonon coupling within deformation potential theory were obtained from our DFT calculations. The contribution of electronic processes (impact ionization) to the lifetime can be estimated from the imaginary part of the electronic self-energy calculated in the GW approximation. Moreover, by numerically solving the rate equations for the occupation numbers in a prototypical electronic band structure coupled to a phononic heat bath, we are able to follow the dissipation of the electronic excitation energy to the Pb lattice vibrations over long time (several picoseconds). The time scales extracted from the simulations are compared to the experimental data from time-resolved pump-probe experiments. In the following I will show by means of deformation-potential theory the electron-phonon coupling strength in quantum-confined states. The aim of this part is simply the fact that with the help of first-principles calculations for the band structures and phonon dispersion and phonon bath model reach to this point to examine the relaxation time for the electron-phonon for 4 and 5 ML lead on the Si(111).

5.1 Introduction

Beside the Coulomb interaction, one of the fundamental interactions which plays a crucial role in the electron and lattice dynamics of condensed matter systems is the electron-phonon interaction, for example a variety of physical phenomena such as electrical resistivity, conventional superconductivity [25], charge transport in electronic and optoelectronic devices.

5.1.1 electron-phonon interaction in Pb:Si experimental standpoint

The scanning tunneling microscopy measurement by Zhang et al. [131] is reported as a good example to investigate the electronic structure and superconductivity of the single atomic layers of Pb:Si(111) and In:Si(111) that are grown epitaxially. The influence of Si substrate is shown through the formation of covalent bonds at the interface. The dimensionless electron-phonon coupling parameter, λ , that comes from variable-temperature ARPES (angle-resolved photo emission spectroscopy) measurement shows that the phonon modes from interface bonding must contribute to e-ph coupling. Investigating EPC, both in super-

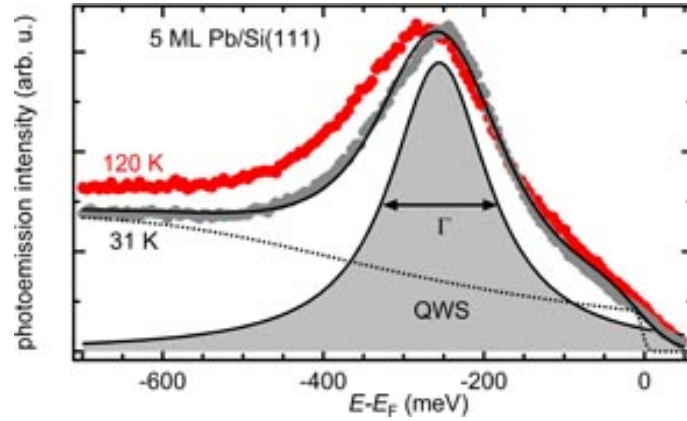


Figure 5.1: Laser photoemission spectrum in normal emission is shown (at $k = \Gamma \pm 0.02 \text{ \AA}^{-1}$) for a 5 ML thick lead film on Si(111) for two different temperatures as indicated. The filled area represents the highest occupied QWS contribution to the spectrum. The dashed line represents the considered background including the FermiDirac distribution function. The limited spectral resolution results in a finite spectral weight above the Fermi level. Adopted from [73]

conductivity materials and in metals far away from equilibrium, constitutes a field of research that has considerably been in the focus of attention recently. In the following I bring some examples of experimental work which are related to the role of electron-phonon coupling in QWSs of Pb on Si(111) substrate, which is in line with the topic of this chapter. As example

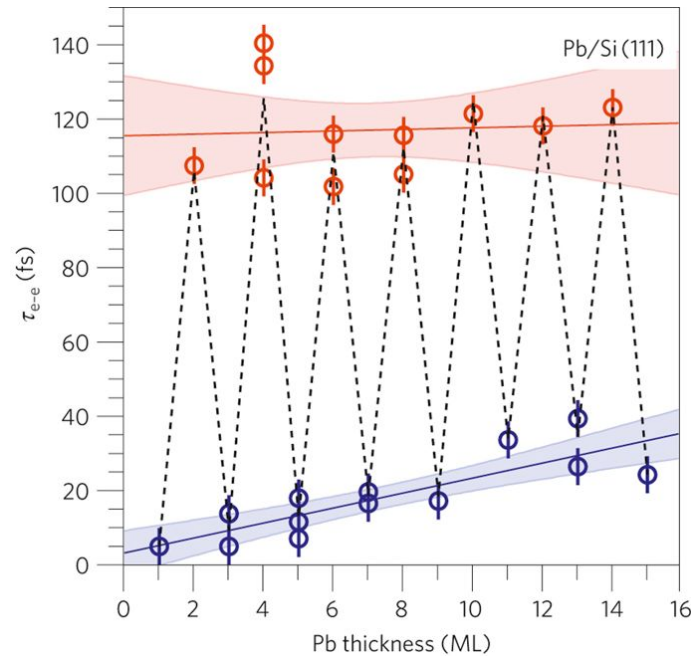


Figure 5.2: Lifetime of the luQWS as a function of Pb thickness. Adopted from [61]

can be mentioned the work of Ligges et al. ([73]) which is the temperature-dependent line

width analysis of occupied quantum well states with the help of femtosecond laser photoemission spectroscopy. They investigated role of the electron-phonon coupling parameters in the vicinity of the Γ point, for electronic quantum well states in epitaxial lead films on a Si(111) substrate. They used the 5, 7 and 12 ML films of lead on Si(111) and that shows the electron-phonon coupling values in the range of 0.6 - 0.9, while the momentum averaged electron-phonon coupling at the Fermi level of bulk lead, ($\lambda = 1.1 - 1.7$) (Fig. 5.1), thus, is attributed to the influence of the substrate on the Pb electronic and vibrational structures. Another example is about the unoccupied electronic band structure of Pb:Si(111) at energies 3-4 eV above the Fermi level which has done by [114]. Hence, the intrinsic electronic states of Pb atomic layer in this energy range have few opportunities to disintegrate in Si-bulk states, which leads to a unusually long electronic life time of up to 35 fs (for a metallized surface at these energies).

Experimentally it is found that Pb-multi layers with atomically smooth, well-defined interfaces to the silicon substrate can be prepared. In these layers, quantum effects in the electronic structure become noticeable, which results from the confinement of charge carriers within the Pb layer. Quantum well states are observed, derived from p_z orbitals of Pb atoms which occur depending on layer thickness. This quantum well states are at different energies, both above and below the Fermi energy.

Based on the experimental perspective, the lifetime of electrons that have been raised in an unoccupied quantum well state by 2PPE are accurately measured [61]. From the Fig. (5.2), one can see that the energetic position of the quantum well states varies widely, depending on whether the Pb film consists of an even or an odd number of layers; moreover, there are striking differences in the life time of the hot electrons. While the highly excited states in the "odd" Pb films disintegrate in less than 40 fs, the "straight" Pb films possess a quantum well state with 120 fs life time [61].

The relaxation dynamics of occupied quantum well states in Pb:Si(111) was investigated experimentally Fig.(5.3) by time-resolved photoemission spectroscopy [96]. In their work, the modifications of the occupied electron states -that occur on an ultrafast timescale and are driven by the photoexcitation- were discussed. They are shown both through: a) using the moderate excitation densities and focus on a transient, while the electronic system is in a non-equilibrium state, and increases in binding energy of the QWSs driven by the optical excitation, and b) the excitation of a coherent surface phonon mode at a frequency of ≈ 2 THz.

5.1.2 life time of hot carrier in Pb:Si from theoretical standpoint

From the theoretical standpoint, the contribution of the electron-phonon scattering at these relatively slow decay processes was investigated. The results are within the expected experimental magnitude, however, does not indicate any satisfactory quantitative agreement. The main limitation of the theoretical approach is simply the fact that so far only freestanding Pb layers could be modeled. In this thesis, the influence of the silicon substrate is taken into consideration both on the complex crystallographic structure ($(\sqrt{3} \times \sqrt{3})$ R30-reconstruction) and the electronic structure of the Pb layers.

The theoretical analysis of the life time went far out exclusively by a Fermi liquid behavior, where in the electron-electron scattering rate was down from the Pb-volume metal basis.

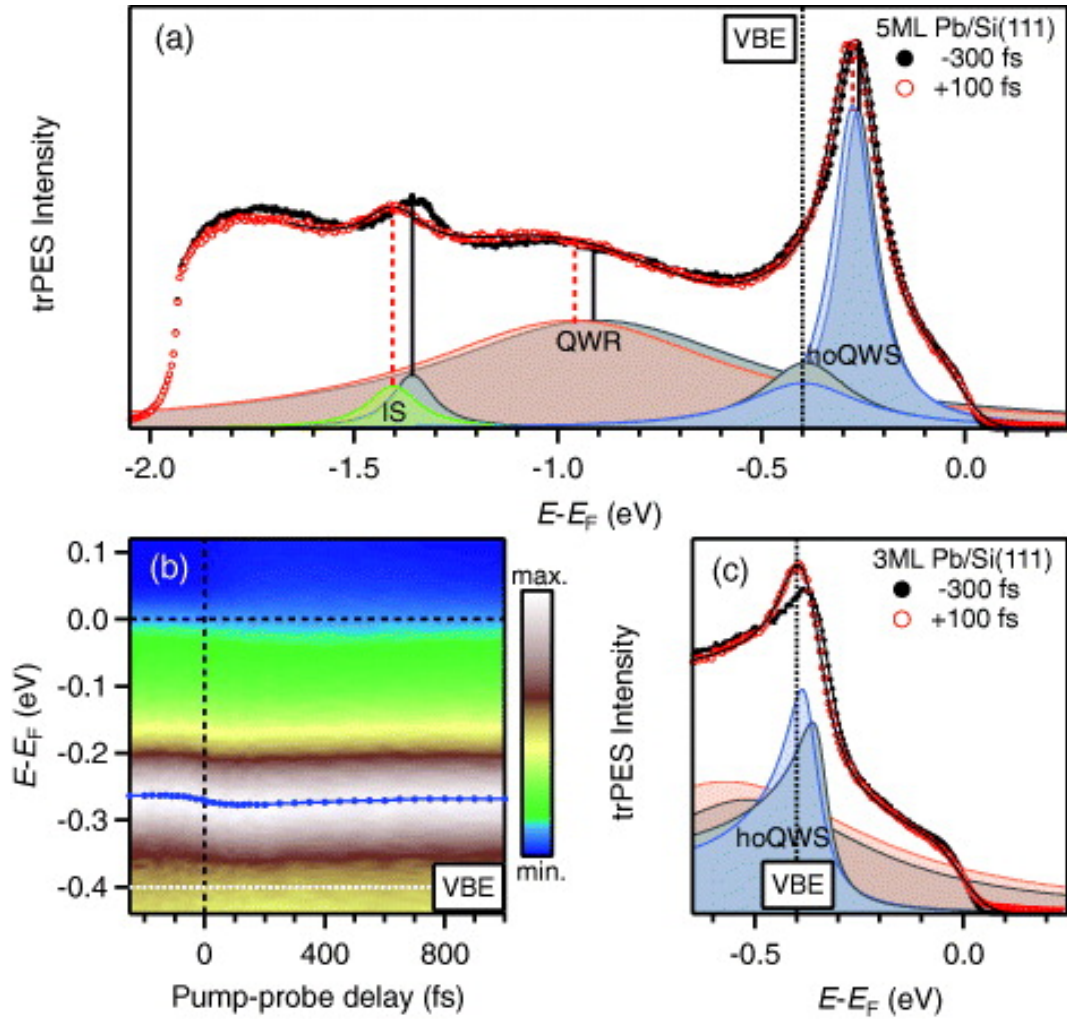


Figure 5.3: ”(a) trPES spectra of a 5 ML Pb film before (black filled circles) and 100 fs after optical excitation (red open circles). The pronounced peak at $E - E_F = 0.26$ eV is the highest occupied the quantum well state (hoQWS). In addition, a broad quantum well resonance (QWR) and an IS at the Pb/Si interface are observed. The peaks used in the fitting model are shown as shaded areas, and the peak positions, determined by the fits, are indicated, exhibiting a peak shift 1E to higher binding energy. The small shoulder at $E - E_F \approx 0.4$ eV is the hoQWS of small areas with 3 ML coverage within the probed spot. (b) trPES intensity for 5 ML coverage in a false color plot is a function of pump-probe delay. The blue line and symbols mark the peak position of the hoQWS obtained by fitting the spectra (see the text). (c) trPES spectra as in (a), but for 3 ML Pb/Si. Consider the pronounced asymmetry of the hoQWS line shape near the silicon VBE, which is reduced upon excitation.” Adopted from [96].

The contribution of the theory includes calculating the scattering rate of the imaginary part of the electronic self-energy that has been evaluated as part of the GW method [32]. In another work [16, 97, 98], the relaxation of the hot electrons was calculated through

exciting lattice vibrations by means of a quantum Boltzmann equation, which was derived from the density matrix dynamics. For the relaxation on the nanosecond-time scale up to thermalization, we refer to [114], that deals with excitation energy input's being further distributed to the numerous lattice degrees of freedom.

For Pb-adsorbed layer (corresponding to $\frac{4}{3}$ monolayers) in $(\sqrt{3} \times \sqrt{3})R30$ reconstruction both the electronic band structure and the phonon spectrum have been studied in [99]. In Sakong's work, density functional theory and molecular dynamics methods were employed to study the dynamics of vibrations localized in a monolayer of Pb on Si(111).

5.2 Quantum well states in thin metallic films

In the following I bring the definition of QWSs and the reason why we chose the QWS of Pb:Si(111) to estimate the electron-phonon relaxation time.

5.2.1 Definition of QWSs

One example where QWS can be found are heterostructures, which are made by joining different materials, usually in layers (which are so thin typically about 100 \AA , or 40 atomic layers that the both electron and hole are considered as waves). In other words, a particular kind of heterostructure in which one thin "well" layer is surrounded by two "barrier" layers forms a quantum well. In fact, the allowed states in this structure correspond to standing waves in the direction perpendicular to the layers. Because only particular waves are standing waves, the system is quantized, hence the name "quantum well".

A free electron confined in a one-dimensional box provides a good starting point. For electronic motion perpendicular to the film surface, the wave vectors \vec{k} for stationary states, or quantum well states, are determined by the requirement that standing wave patterns fit into the geometry,

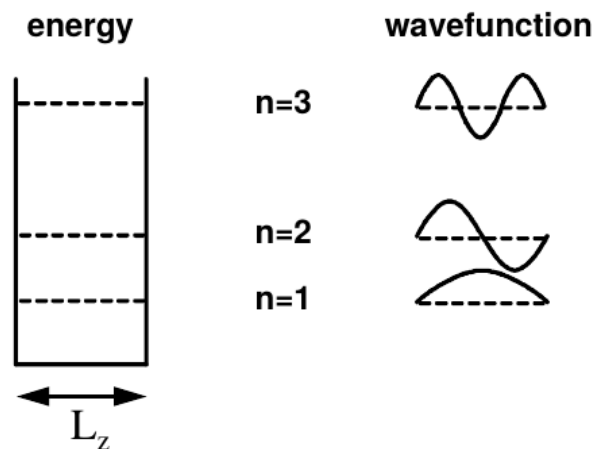


Figure 5.4: quantum well and associated wavefunctions.

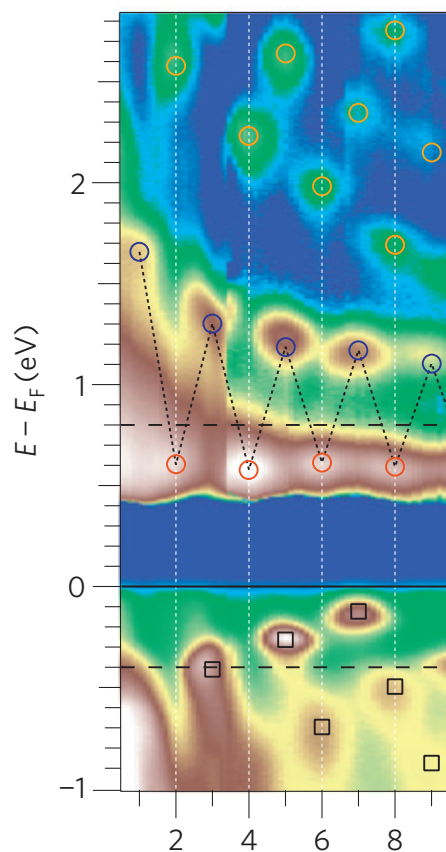


Figure 5.5: The 2PPE intensity is shown on a logarithmic scale, whereas the 1PPE intensity is plotted on a linear scale. Red (blue) circles indicate the binding energies of the luQWS for even (odd) N ; yellow circles indicate higher-lying QWSs. Adopted from [61]

$$k = \frac{n\pi}{d}, \quad (5.1)$$

where n is an integer quantum number and d is the film thickness or box dimension. The energy levels are given by

$$E = \frac{\hbar^2 k^2}{2m} = \frac{\hbar^2 (n\pi/d)^2}{2m} \quad (5.2)$$

where m is the free electron mass, and the wave functions are given by

$$\psi(z) \propto \sin\left(\frac{nz\pi}{d}\right) \quad (5.3)$$

And for the two dimensional case we can write:

$$\psi(x, y) = \frac{2}{\sqrt{L_x L_y}} \sin(k_x x) \sin(k_y y) \quad (5.4)$$

where the

$$k_x = \frac{n_x \pi}{L_x}, \quad k_y = \frac{n_y \pi}{L_y}$$

The standing electron wave can be considered to be in the QWS state when the thickness of a metal layer becomes comparable to the electron coherence length. These states are parallel to the surface. The bands typically show a free electron like dispersion, but are quantized in the direction perpendicular to the surface. As on one side the states are confined by the metal-substrate interface and the other side is the metal-vacuum interface, the confinement potential for QWS is asymmetric.

5.2.2 Motivation of study layers of lead on Si(111)

Since the thickness of lead (Pb) films grown on silicon can be defined with atomic precision from one monolayer (ML) to several tens of MLs [126], thin Pb films have become a prototype system in surface science and nanotechnology and have been subject to intense investigations, both experimentally and theoretically. The quest for the thin-film limit of superconductivity has spurred interest in the phonon band structure and electron-phonon coupling in the Pb films [14, 75, 131]. Due to their homogeneity, these systems lend themselves to the study of quantum effects in metals. The spatial confinement of the electronic bands derived from the $6p$ states of Pb leads to discrete electronic bands that show little dispersion for motion of the carriers within the film. These states have been called Quantum Well (QW) states. Moreover, it has been demonstrated [124] that the electronic and vibrational properties of Pb films display oscillations with the number of atomic layers, alternating properties of films with even or odd number of layers (Fig.5.5). This can be understood as a consequence of the p_z orbitals changing their sign at the position of the Pb nuclei, with the result that the sign of the QW wavefunctions is recovered only after each second Pb layer. Recently, both single-photon photoemission [73, 77] as well as two-photon pump-probe spectroscopy [60, 61] and scanning tunneling spectroscopy [51] have provided detailed insight into the level structure and the lifetime of excited electrons in the QW states. However, in the theoretical description of QW states, too little attention has been paid to a realistic description of the atomic structure. Due to the different lattice constants of Si and Pb, the film preparation may yield a variety of atomic structures. One example, realized by a dense single layer of Pb atoms on Si(111), is the so-called striped incommensurate phase [20]. Locally, it can be approximated by a $(\sqrt{3} \times \sqrt{3})$ unit cell of Si(111) containing four Pb atoms. Although this is already a slightly simplified model for Pb films on Si(111), even simpler models, namely free-standing Pb films with only one Pb atom per layer in the unit cell, have been used so far [47, 128]. The agreement between theory and experiment concerning both the energetic position of the QW states as well as their dispersion has not been satisfactory (see e.g. the comparison in Ref. [73]), probably due to the neglect of the Si substrate and the true lateral periodicity of the Pb film in the calculations. The unexpected almost vanishing dispersion of the highest occupied quantum well state in odd-layered films had already been noticed in earlier experiments [27].

As a consequence of the poorly described atomic structure, it has also proven difficult to capture the dynamical properties of the charge carriers within simple models. The lifetime broadening of the highest occupied quantum well state, caused by electron-phonon scattering, is well accessible to photoemission studies but is overestimated in a theory based on a

(1 × 1) structural model. As speculated in Ref. [73], the discrepancy could be due to an electronic wavefunction not strictly localized within the Pb film but extending partly into the Si substrate, which cannot be captured by a structural model employing a free-standing Pb film. Similarly, the relaxation rate of highly excited electrons may depend on structural details. Dynamical electron diffraction experiments [134] have shown that the energy deposited by a laser in the Pb films in the form of electronic excitations is converted to lattice vibrations in less than two picoseconds. However, quantitative knowledge of the electron-phonon coupling in highly excited states is scarce. In two-step pump-probe spectroscopy, electronic states at energies between 0.5 and 3.5 eV above the Fermi level were probed as intermediate states [61]. While the lifetime of short-lived states (in the tens of femtosecond regime) are controlled by electron-electron scattering, a possible contribution of electron-phonon scattering to the relaxation rate in the more long-lived states cannot be *a priori* excluded.

In this chapter, I attempt to develop a sound basis for the investigation of electronic relaxation processes in atomically thin Pb layers by working with the more realistic ($\sqrt{3} \times \sqrt{3}$) model for film thicknesses between 3 and 6 ML. In particular, I want to find out whether the oscillations with the layer thickness found in the electronic and vibrational properties also carry over to the more complex, derived quantities, e.g. the electron-phonon coupling strengths. In this thesis, Density functional theory calculations are employed to obtain both the electronic and the phononic two-dimensional band structures of the films. Subsequently, the strength of the electron-phonon coupling is investigated for representative (either occupied or unoccupied) QW states in the four-layer and five-layer Pb films. The results are compared to experimental data of the energetic position, dispersion, and lifetime of QW states.

5.3 Relaxation of excited electrons

The electron population decay observed experimentally for the luQWS is shown in Fig. (5.6) in the time domain by cross-correlation traces as a function of coverage. The (a) shows the population of odd layers Pb on Si (111), while the (b) shows the population of even lead layers. As it is shown for the odd layers fast population decay is observed, which slows down with increasing thickness. In contrast, for even N a slower and thickness-independent decay is found [61].

5.3.1 Estimated Lifetime due to e-e scattering

The experimentalists evaluated the quasiparticle lifetimes from a fit of their data to a rate-equation model that is convoluted with the laser-pulse envelope. This model enabled them to determine the hot-electron lifetimes independently from a delayed population build-up due to secondary electrons. Essentially, the lifetimes are given by the inverse slope of the initial population decay, $\tau = \frac{\hbar}{\Gamma}$, as indicated in Fig. (5.6). In their study for odd layer coverage: > 150 -200 fs and for even layer coverage: > 800 fs) [61] is observed. As it is shown in the (Fig.5.7) left, the lifetime is anticorrelated with the energy of the quantum well state above E_F , or in other words, is related to $\tau = \frac{1}{E-E_f}$. The black line in Fig.5.7 (left side) corresponds to [23] a GW calculation for bulk Pb. As we can see within the GW

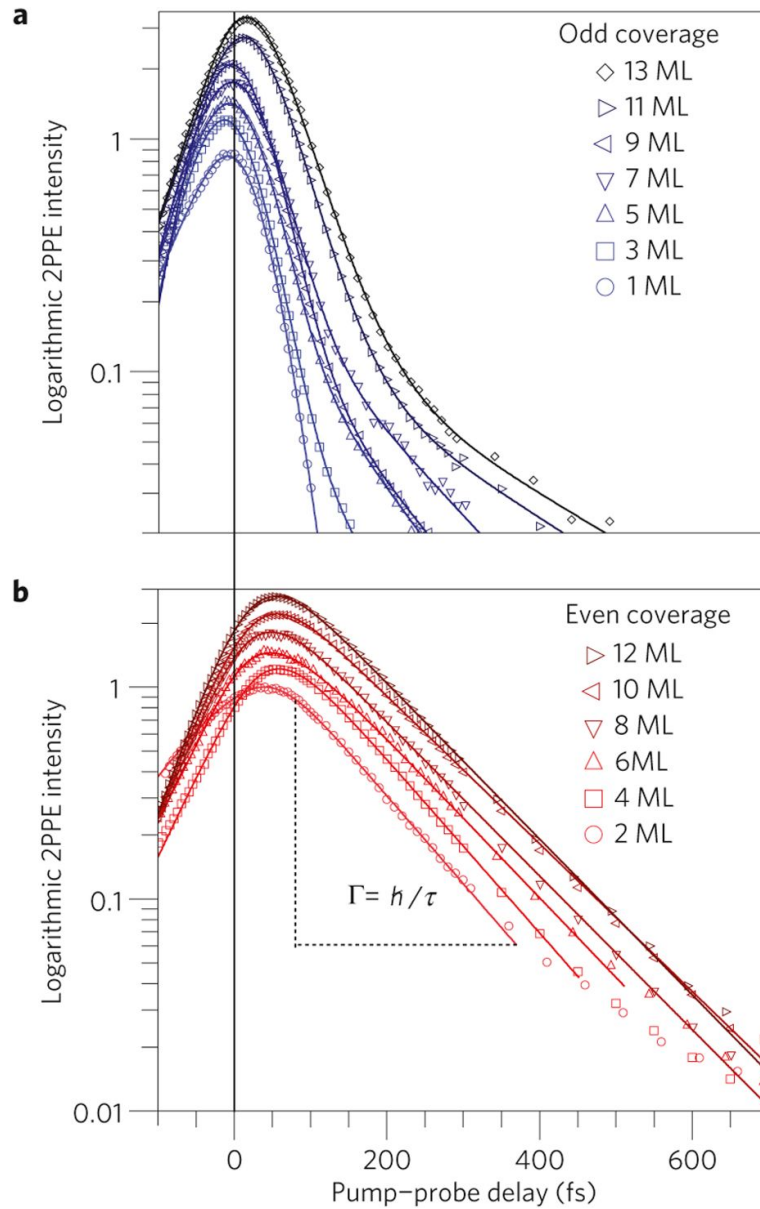


Figure 5.6: **a** and **b** are a logarithmic intensity scale of cross-correlation traces for odd and even N , respectively. The fast initial population decay time for odd N decreases with coverage, whereas the decay time for even N is slower and coverage independent. Adopted from [61]

approximation, this results directly in the quadratic dependence of Γ_{e-e} on $E - E_F$. From theoretical side of view a variety of methods is employed to study electron and hole dynamics in metals and a self-energy formalism of many-body theory is the most powerful of them used for calculations of inelastic e-e scattering. In right side of (Fig.5.7) we calculated the imaginary part of self energy which is evaluated in terms of the screened interaction and the allowed final states for the decay process as function of the binding energy. By fitting the

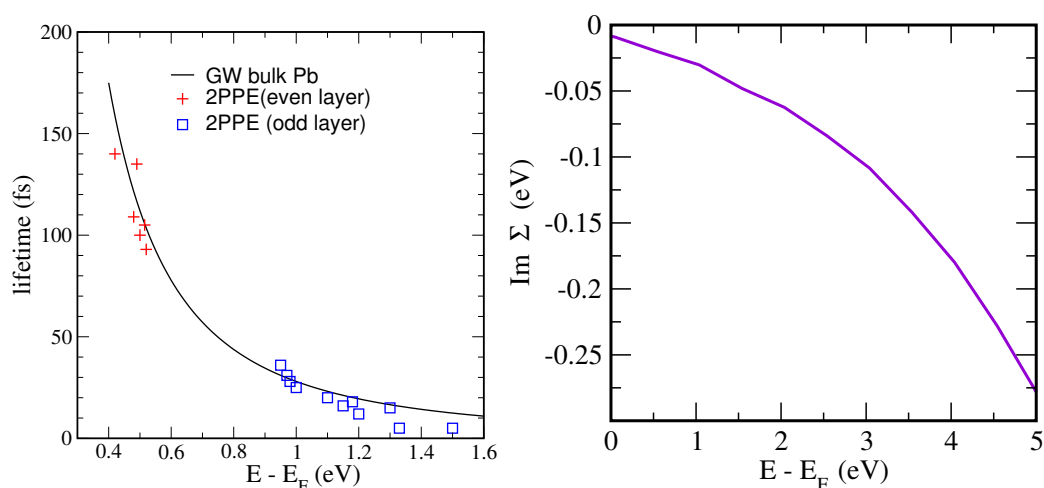


Figure 5.7: **left side:** Analysis of the quasiparticle lifetimes of the luQWS as a function of binding energy. red star and blue square are related to 2PPE for even and odd layer, respectively [61]. The black line is GW [23] calculation. **right side:** imaginary part of self energy as function of the binding energy for bulk Pb from our calculation.

data we get the eq. (5.6).

$$\text{Im}\Sigma(E) = -\frac{0.011}{\text{eV}}(E - E_F)^2 \quad (5.5)$$

$$\frac{1}{\tau} = -\frac{2}{\hbar}\text{Im}\Sigma(E) = \frac{(E - E_F)^2}{30\text{fs}(\text{eV})^2} \quad (5.6)$$

So the 30 fs comes from this calculation. This matches with the 2PPE data for even and odd layers Pb on Si(111). For estimating the life time of the electron-electron scattering we have already calculated the imaginary part of the self energy, specifying the first term in (5.7).

$$\frac{1}{\tau_{tot}} = \frac{1}{\tau_{e-e}} + \frac{1}{\tau_{e-ph}} \quad (5.7)$$

So now the question arises what is the electron-phonon contribution to the lifetime in the QW state? The goal of this chapter is to answer this question from theory side of view.

5.4 Details of DFT calculations

In this project, all calculations were performed in the framework of Kohn-Sham density functional theory using the projector augmented-wave method and the software package Vienna Ab initio Simulation Package VASP [63, 65], which is a computer program for atomic scale materials modelling, e.g. electronic structure calculations and quantum-mechanical molecular dynamics, from first principles. The Perdew, Burke, and Ernzerhof (PBE) formulation of

the generalized gradient approximation (GGA) functional was used in this work. While it is well known that the band gap of the Si substrate comes out too small in GGA calculations, our interest is in the electronic and vibrational structure of the Pb layers: topics that are sufficiently well described by our choice of the functional. The results shown below were obtained with a description of the Pb atoms using the $6s$ and $6p$ electrons as valence states as well as neglecting spin-orbit coupling. The results were tested against the use of a larger set of valence states of Pb, including the fully occupied $5d$ shell as valence electrons, and taking spin-orbit coupling into account. A slab of ten layers of Si atoms was used to model the silicon substrate. The Si dangling bonds on the rear side of the slab were saturated by hydrogen atoms while varying amounts of Pb were placed on the front surface. For the lateral periodicity, we used a (2×2) supercell with the lattice constant of bulk Pb, which was obtained as 4.09 \AA in our PBE-GGA calculations. Including the $5d$ electrons and spin-orbit coupling results in a slightly larger lattice constant of Pb of 4.11 \AA . This Pb supercell is matched with a $(\sqrt{3} \times \sqrt{3})$ supercell of the Si substrate. While the two lateral periodicities of Pb and Si match closely, the remaining mismatch of 5.7% is accommodated (in our calculations) within the silicon substrate. I have chosen this strategy for setting up the geometry because we aim to model experimental Pb films that are laterally fully relaxed (as observed, e.g., in the striped incommensurate phase) and because we want to make contact with previous calculations of freestanding Pb films that also employed the Pb lattice constant. The calculations have been carried out using a plane-wave basis set up to the energy cutoff of 300 eV . In order to sample the Brillouin zone of the $(\sqrt{3} \times \sqrt{3})$ unit cell, we used a $4 \times 4 \times 1$ Monkhorst-Pack [24] k-point mesh. The positions of all Pb atoms, as well as of the Si atoms in the first eight layers, were relaxed, while the terminating hydrogen atoms and the lowest two layers of Si were held fixed. The phonons were calculated using the program package PHONOPY [25] in conjunction with the VASP code. After the atomic positions within the supercell were carefully relaxed, a larger supercell was constructed by doubling the size in both lateral directions to study finite atomic displacements. Atomic forces were obtained from VASP for 168 and 192 displaced configurations for the 4 and 5 ML Pb films, respectively. From these forces, the force constants and dynamical matrix were obtained with the help of PHONOPY, and phonon modes as well as the corresponding eigenvectors of atomic displacements were obtained.

5.4.1 Atomic structure

Now it is turn to investigate the position of QWSs in different layers of lead on the Si(111) substrate. In the literature, mostly free-standing Pb films have been studied using a (1×1) lateral periodicity [124]. These films allow for a simple interpretation of their electronic structure but cannot be compared directly to experiment since they do not take into account the effects of the Si substrate. In experimental film preparation, first a single layer of Pb is grown on Si(111) which displays the $\sqrt{3} \times \sqrt{3}$ structure that has been studied in great detail [20, 94, 99, 105]. Subsequently, an arbitrary number of Pb layers may be grown on this wetting layer by low-temperature deposition [57]. The additional layers inherit the periodicity imposed by the first Pb layer. For this wetting layer, we assume the T4 structure described previously: it consists of four Pb atoms, one in the T4 position while the other three Pb atoms are close to on-top positions with respect to the Si(111) surface atoms. In building up thicker films, we assume that the Pb atoms in the next layer fill the hollow

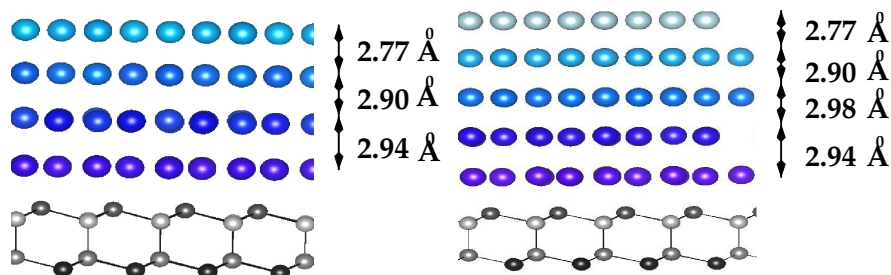


Figure 5.8: Side view of 4 ML Pb/Si(111) (left) and 5 ML Pb/Si(111) (right)

positions of the previous layer, thereby following an fcc stacking sequence. After relaxing the atomic positions, a structure with planar Pb layers is obtained. The relaxed 4 ML and 5 ML Pb films on Si are shown in side view in Fig. 5.8. We find that the distance between the Pb surface and subsurface layer is reduced to 2.77 Å compared to the layer distance of 2.89 Å in Pb bulk. Such a contraction is to be expected, since the surface Pb atoms have only nine nearest neighbors, compared to 12 nearest neighbors in bulk Pb. The surface Pb atoms attempt to compensate for the reduced embedding charge density delivered by the neighbor atoms by moving closer to the Pb atoms in the subsurface layer.

5.4.2 Electronic structure and quantum well states from free-standing to $\sqrt{3} \times \sqrt{3}$

The electronic states around the Fermi energy in bulk Pb are formed by highly dispersive bands originating from the $6p$ orbitals of Pb. In the thin films, the dispersion in the film plane persists and is apparent in the steep bands crossing the Fermi level and reaching their minima close to the K and M points of the Brillouin zone. The bands formed from the $6p_z$ orbitals in bulk Pb transform to quantum confined states. The energy band observed in bulk Pb is broken up into regularly spaced states appearing over an energy interval of several eV. These states, clearly visible in particular near the Γ point, are called quantum well (QW) states. In those areas where they cross with the highly dispersive in-plane bands, the $6p_z$ states hybridize with the $6p_x$ and $6p_y$ states, but near the edges of the Brillouin zone, near the K and M points, states with clear $6p_z$ character can again be distinguished.

Here, we aim at an investigation of the influence of the Si substrate on the electronic structure and the QW states of the Pb films. Generally speaking, one can distinguish between structural effects, e.g. different relaxation of the Pb layers resulting from their enforced match with the atomic corrugation of the Si(111) and chemical effects caused by the bonding of the Pb atoms to the top-most Si layers. To be able to trace these effects, we start with calculations of the well-known model system of a free-standing Pb film with (1×1) unit cell. In a second step, we study the electronic band structure of the full system using the $(\sqrt{3} \times \sqrt{3})$ unit cell of Si(111) and a substrate modelled by five bilayers of Si.

For the (1×1) model systems, the results for one even layered (4 ML) and one odd-layered (5 ML) film are displayed in Fig. 5.9. In the vicinity of the Γ point, one can clearly identify quantum well states, as reported previously from calculations of free-standing Pb films [124]. The energy level scheme shown in Ref. [124] is used to label the states by QW_n where n is the number of the QW state counting from lower to higher energies. In particular, one can

notice that the 5 ML film has an occupied state labelled QW3 located at 0.4 eV below the Fermi level E_F , which is expected to lie inside the band gap of Si if the substrate would be present, and an additional state QW4 at 1.7 eV. This is in contrast to the 4ML film where the region around E_F at the Γ point is free of states and hence one would not expect states in the Si band gap in the presence of the substrate. However, unoccupied QW states are observed at 0.5 eV and 2.7 eV, labelled QW3 and QW4, respectively.

After crossing the steep $6p_{x,y}$ bands, the $6p_z$ -like bands re-appear near the Brillouin zone edge and can be labelled according to the corresponding QW bands originating from the Γ point. The Brillouin zone, corresponding to the larger ($\sqrt{3} \times \sqrt{3}$) unit cell which we will consider below, is reduced in size, and the M point of the (1×1) Brillouin zone will be folded back onto the Γ point of the new, smaller Brillouin zone. (Note that the enlarged real-space unit cell is actually (2×2) when referring to the Pb layer, but we keep the more common notation ($\sqrt{3} \times \sqrt{3}$) referring to the Si lattice.) Because of the backfolding of the band structure, we have labelled the QW states near M as QW2b, QW3b, QW4b and so on, where the "b" is meant to be reminiscent of backfolding. In separate calculations including spin-orbit coupling (not shown), we found its effect on the QW states to be small. Since inversion symmetry is retained in the free-standing films, the electronic structure is described by states with two-fold degeneracy even in the presence of spin-orbit coupling. The most pronounced effects of spin-orbit coupling are notable in the $6p_{x,z}$ derived bands near the K point.

For the realistic Pb films with ($\sqrt{3} \times \sqrt{3}$) unit cell, the electronic band structure is shown in Fig. 5.11 for 4 ML and in Fig. 5.12 for 5 ML of Pb. The complexity of the electronic structure is best analyzed by taking into account the backfolding of the bands of the (1×1) unit cell.

In agreement with the expectations from the free-standing films, we observe that the gap at the Γ point is free of states in the 4 ML Pb film on Si(111). However, there are also important features *not* captured in the (1×1) model. In films with an odd number of layers (3 and 5 ML), the third quantum well state of the Pb film, QW3, is energetically placed near the valence band of silicon. The interaction of Pb with Si(111) thus transforms QW3 into an occupied quantum well resonance (QWR) that is energetically located in the lower part of the Si band gap. As can be seen from plots of the charge density pertaining to this state (Fig. 5.14, left), it extends several layers into the Si substrate.

Similarly, in the even-layered films (4 ML and 6 ML), the state QW3 is transformed by the interaction with the substrate. Since QW3 in even-layered films had a positive energy and hence falls into the conduction band states of Si, it is transformed into an unoccupied QWR above the Fermi energy E_F at 0.45 and 0.39 eV (4 ML and 6 ML) respectively. Moreover, both the even and odd-numbered films display an occupied interface state (IS) in the range of -0.9 to -0.7 eV. The wavefunctions of these states have maximum amplitude at a bonding orbital between the surface Si atoms and the lowest Pb layer of the film. This IS state is supported by experimental spectra [96], where a rather broad feature has been observed at this energy. In the experimental work [96], this feature is named a quantum well resonance. Notwithstanding this experimental assignment, we prefer to classify it as an interface state based on the inspection of the wavefunction. However, it should not to be confused with another interface state at -1.5 eV observed in this experimental work [96].

In the range between E_F and 3 eV above E_F , several states with strong Pb $6p_z$ orbital character can be identified and assigned by comparison to the (1×1) model. The dispersive

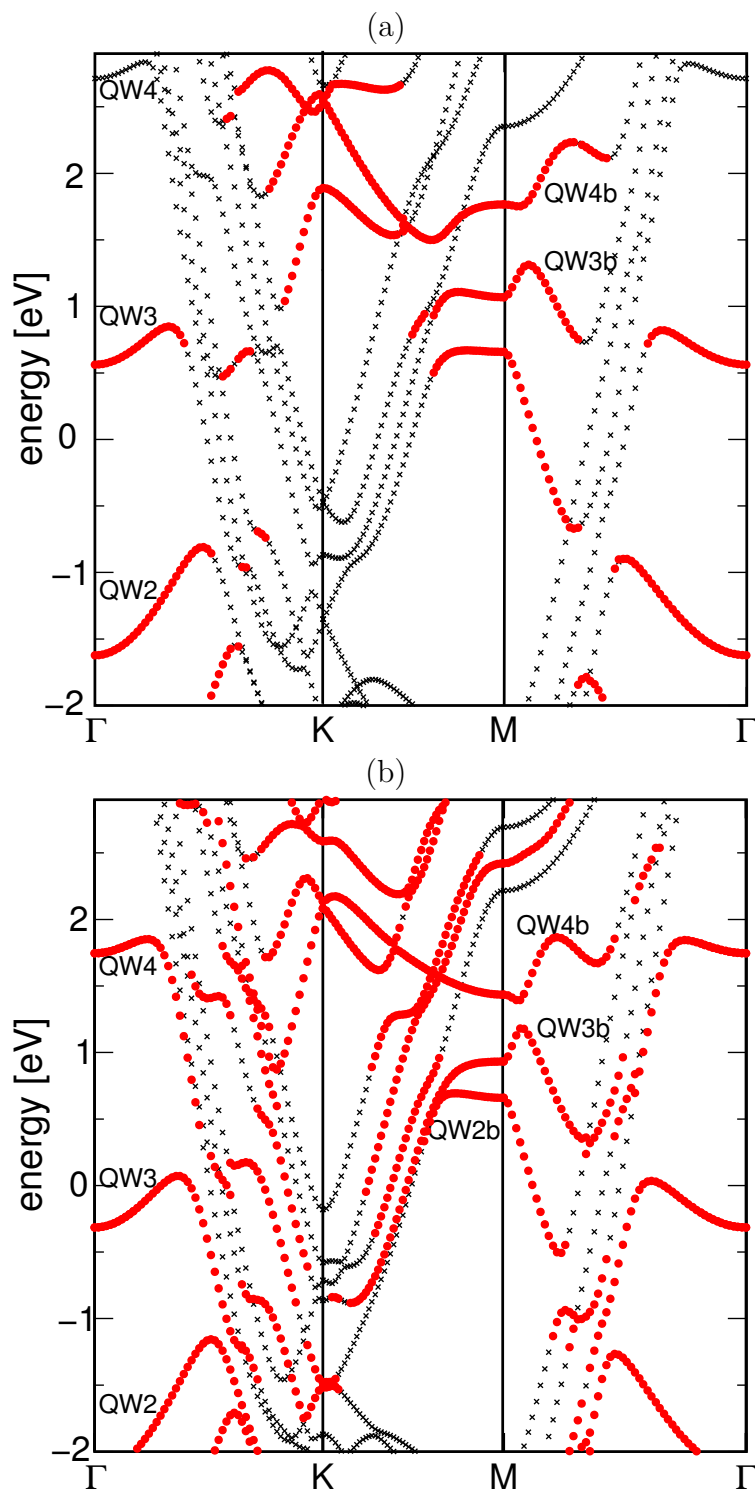


Figure 5.9: Electronic bands structure for a model system of a free-standing (1×1) Pb film for (a) 4ML (b) 5 ML of Pb. The red symbols indicate the $6p_z$ -character of the states to be identified with the quantum well states

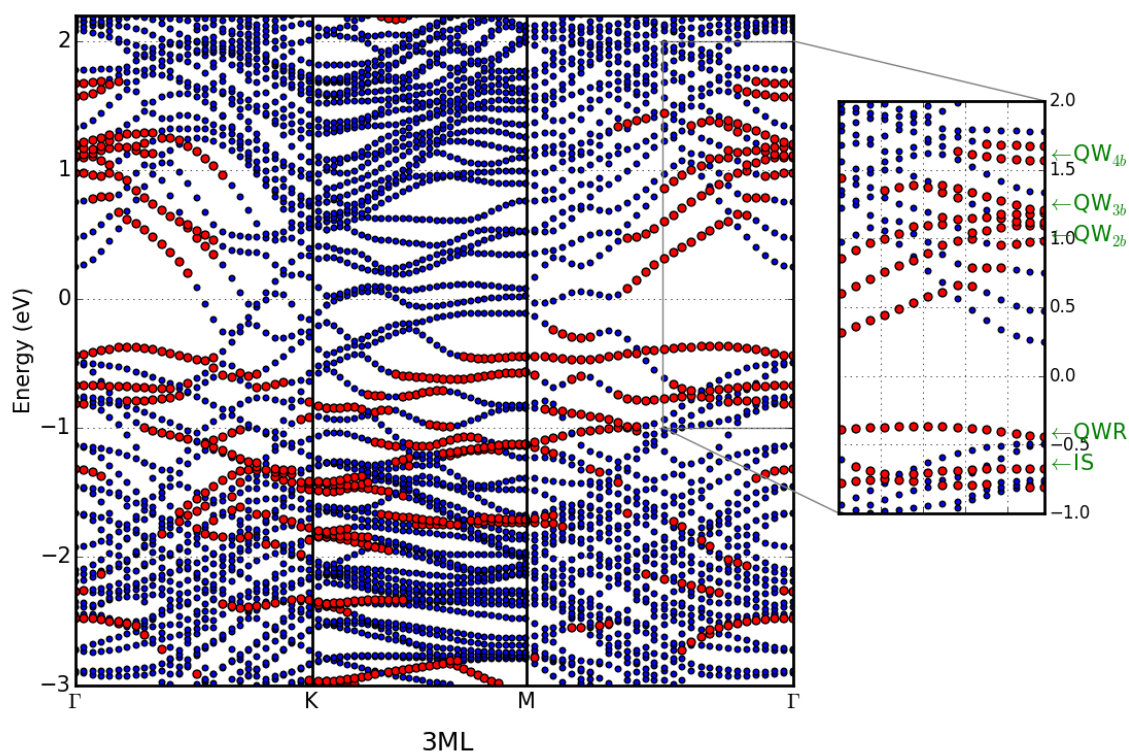


Figure 5.10: Electronic band structure of 3 ML Pb/Si(111) ($\sqrt{3} \times \sqrt{3}$). The red symbols mark bands with distinct Pb $6p_z$ character indicative of quantum well states. The arrows at the margins mark the position of the quantum well resonance (QWR), the backfolded part of the QW states (QW2b, QW3b and QW4b).

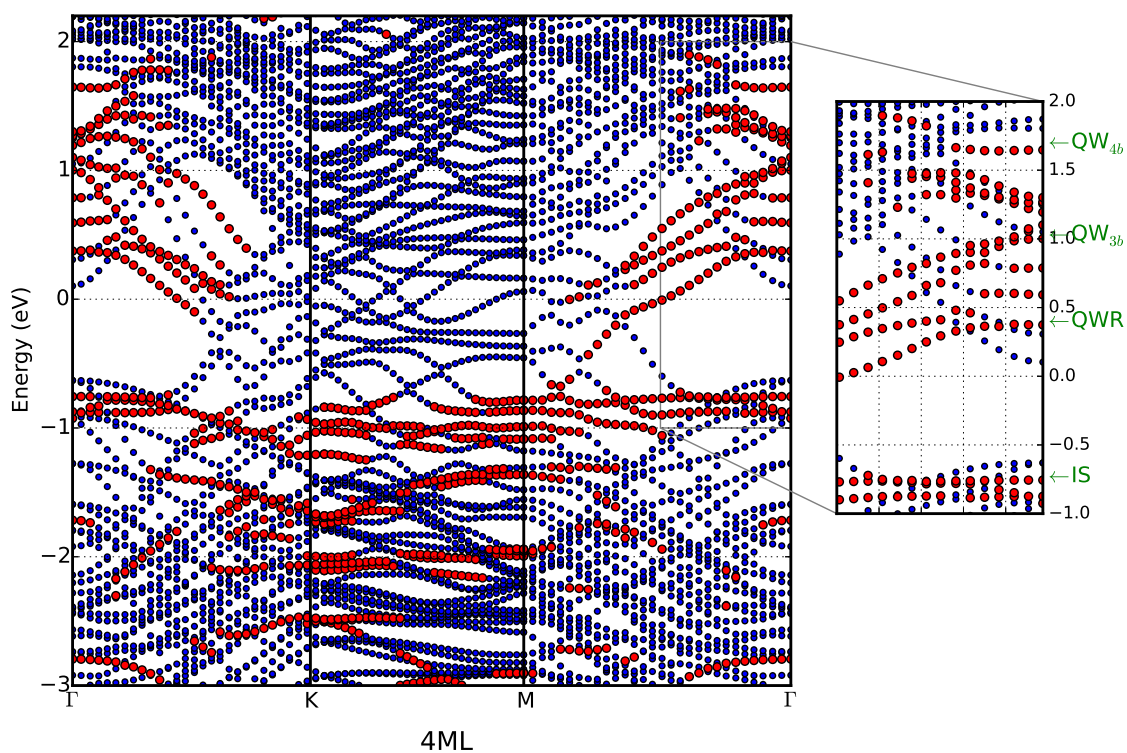


Figure 5.11: Electronic band structure of 4 ML Pb/Si(111) ($\sqrt{3} \times \sqrt{3}$). The red symbols mark bands with distinct Pb $6p_z$ character indicative of quantum well states. The arrows at the margins mark the position of the quantum well resonance (QWR), the backfolded part of the QW states (QW3b and QW4b). Also, an interface state (IS) is indicated at Γ .

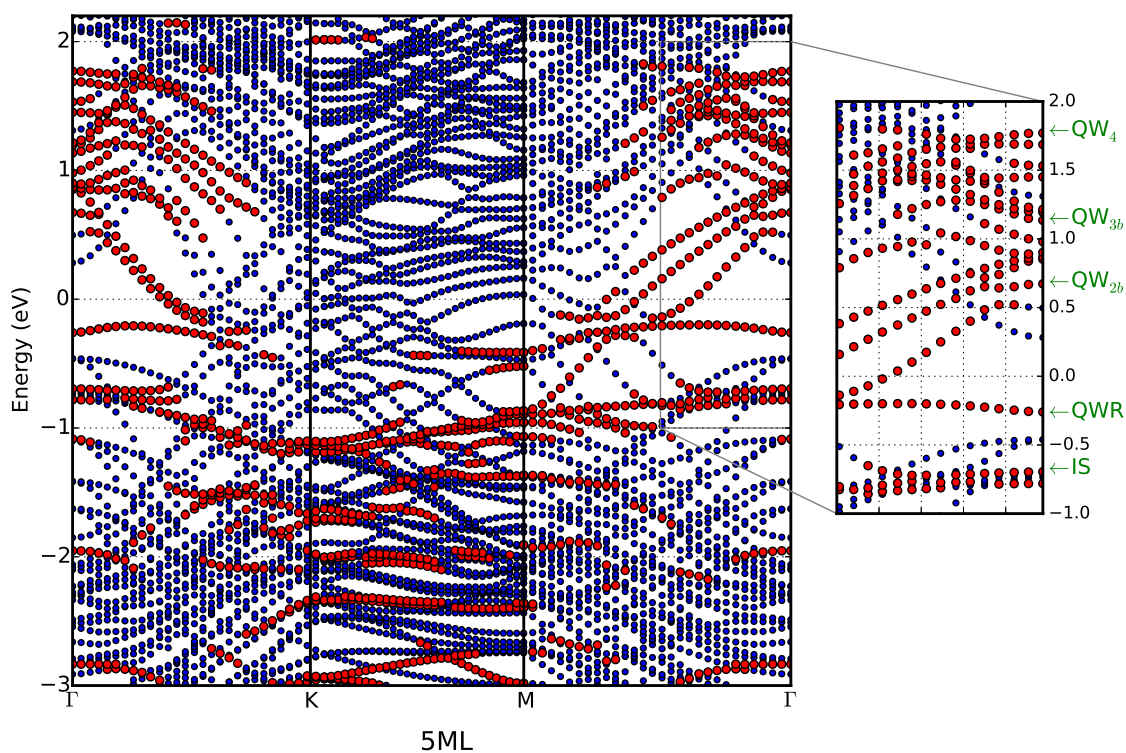


Figure 5.12: Electronic band structure of 5 ML Pb/Si(111) ($\sqrt{3} \times \sqrt{3}$). The red symbols mark bands with distinct Pb $6p_z$ character indicative of quantum well states. The arrows at the margins mark the position of the quantum well resonance (QWR), the QW4 and the backfolded part of the QW states (QW2b and QW3b). Also, an interface state (IS) is indicated at Γ .

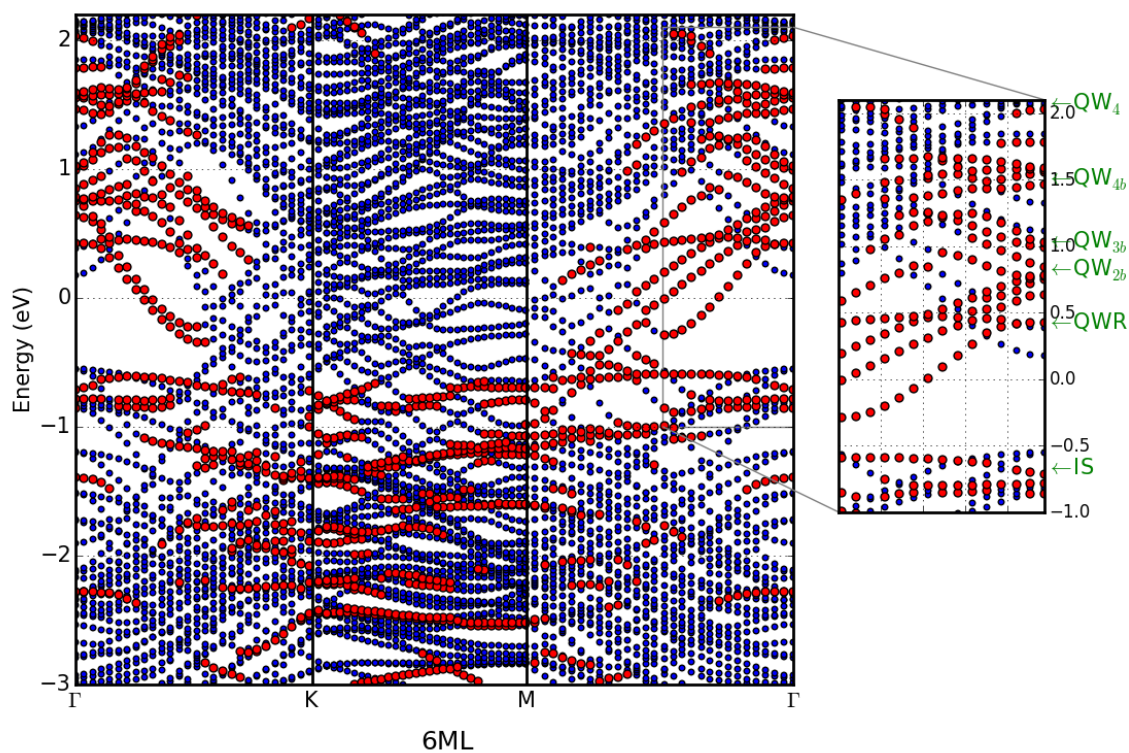


Figure 5.13: Electronic band structure of 6 ML Pb/Si(111) ($\sqrt{3} \times \sqrt{3}$). The red symbols mark bands with distinct Pb $6p_z$ character indicative of quantum well states. The arrows at the margins mark the position of the quantum well resonance (QWR), the QW4 and the backfolded part of the QW states (QW2b, QW3b and QW4b). Also, an interface state (IS) is indicated at Γ .

branch of the band structure of the (1×1) films, originating from the third quantum well state, is backfolded from the M point to the Γ point in the $\sqrt{3} \times \sqrt{3}$ structures. This leads to a feature labelled QW3b in the band structure near Γ occurring at 1.17 eV in the 4 ML film and at 1.2 eV in the 5 ML film. A similar observation can be made for the state QW4b at the M point of the (1×1) Brillouin zone, which reappears after backfolding at the Γ point at 1.63 eV and 1.78 eV in the 4 ML and 5 ML Pb films on Si(111), respectively. In

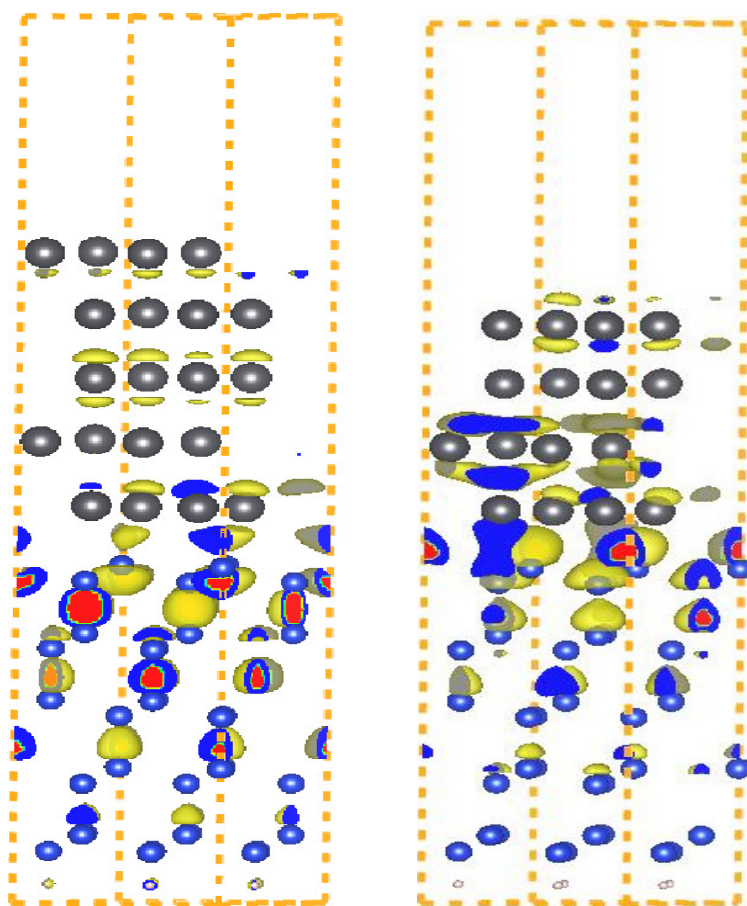


Figure 5.14: Wavefunction of the QWR of 5 ML and 4 ML (left and right, respectively) Pb on Si(111) ($\sqrt{3} \times \sqrt{3}$). The Si atoms are indicated by the blue and the Pb atoms by the grey spheres. Red to yellow color corresponds to high to low charge density.

the latter case, it is energetically very close to the state QW4. The energetic positions of all characteristic features are summarized in Table 5.1. In addition to the 4 ML and 5 ML systems, band structure calculations have been performed also for 3 ML and 6 ML (shown in Fig 5.10 and 5.13) and the corresponding features have been extracted. It is seen that the occupied QWR occurs in all odd-layered films considered, while the unoccupied QWR occurs in all even-layered films.

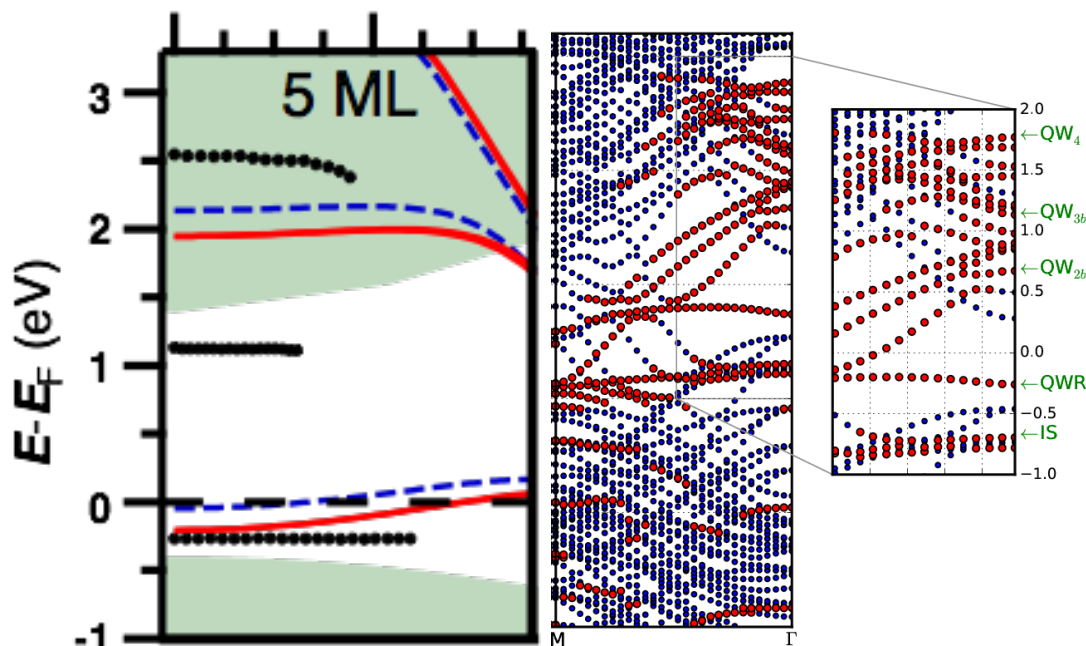


Figure 5.15: Electronic structure below and above E_F for 5 ML Pb/Si(1 1 1) along $\Gamma \rightarrow M$. The left fig shows experimental plot [100], whereas the right one is our data of 5ML coverage. In the left fig : the black points denote experimental data, the different lines indicate free and fixed DFT calculations. The shaded areas highlight the Si projected bulk bands taken from literature. The long dashed line at $E_F = 0$ eV marks the Fermi energy. The QWR with very small dispersion for both left and right (experiment and our calculation), remains below the Fermi energy E_F .

Table 5.1: Features of the electronic structure of Pb films on Si(111) ($\sqrt{3} \times \sqrt{3}$) in dependence on the film thickness. The numbers (given in eV) have been taken at the Γ point. The experiment [61] observes features in 2PPE at 0.6 eV for all even-layered films and at 1.3 eV in the 3 ML film and 1.2 eV for the 5 ML film. In the 5 ML film according to Ref. [100], the QW states are at -0.25 eV, 1.1 eV and 2.5 eV.

	3 ML	4 ML	5 ML	6 ML
IS	-0.68	-0.77	-0.85	-0.71
QWR	-0.45	0.36	-0.25	0.39
QW2b	0.98	-	0.85	0.78
QW3b	1.20	1.17	1.20	0.99
QW4b	1.56	1.63	-	1.46
QW4	-	-	1.78	2.03

5.5 Comparison the position of QWSs to the experiment

Our findings for the $\sqrt{3} \times \sqrt{3}$ films are in much better agreement with photoemission spectroscopy [61, 100] than previous calculations, Fig. (5.15). In particular, we identify the feature observed in Ref. [61] at 0.6 eV above E_F with the unoccupied QWR of the even-layered films, whereas the observed feature at 1.2 eV is assigned to the QW3b state. While the simple (1×1) model predicts an upward dispersion of the QW states near the Γ point, the QW states in the $(\sqrt{3} \times \sqrt{3})$ films show less dispersion. The latter finding is in much better agreement with spectroscopic data [100] (Fig. (5.15) left side), indicating an almost dispersionless state. Such an almost dispersionless feature just below E_F , observed already many years ago [27], had puzzled experimentalists for a long time. When the $(\sqrt{3} \times \sqrt{3})$ reconstruction of the interface is taken into account, as in our calculations, the QWR in the odd-layered films provides a natural explanation for this spectroscopic feature.

5.6 Phonon dispersion

Here, the goal of our work is to address possible differences between phonons in very thin films as compared to bulk phonons. In bulk Pb with the face-centred cubic structure, the acoustic phonon branch reaches a maximum of 2.19 THz. This is observed in neutron diffraction experiments [12] and reproduced in DFT calculations. To study phonon modes in the Pb/Si(111) $(\sqrt{3} \times \sqrt{3})$ films, we use the frozen-phonon method in a $(2\sqrt{3} \times 2\sqrt{3})$ supercell. All Pb layers plus two Si bilayers have been considered as mobile atoms, while the three lowest bilayers of the Si substrate have been held fixed. From the obtained phonon spectra, which have a maximum of 13.1 THz, only the low-frequency branches are displayed in Fig. 5.16. Most of them correspond to vibrations with a large amplitude on the Pb atoms: In the 4 ML slab, the 16 Pb atoms contribute 48 degrees of freedom that are supplanted by two modes with Si substrate character. In the 5 ML slab, the 20 Pb atoms contribute 60 degrees of freedom. Both for the 4 ML and the 5 ML Pb films, the maximum of the optical Pb modes at the Γ point is found to be higher than the maximum phonon frequency of bulk Pb. This tendency has also been found experimentally [11] for thin Pb films on Cu(111). In the 4 ML slab, the maximum at 2.45 THz is even somewhat higher than in the 5 ML slab at 2.30 THz. In both cases, the stiffening of the phonon spectrum compared to bulk can be traced back to the strengthening of the bonds between the topmost two Pb layers. This strengthening can be inferred from the shortening of the distance between these layers to 2.77 Å; see Fig. 5.8.

Eigenvectors of atomic displacements for 4 ML Pb/Si(111) are shown in Fig. 5.17 for selected phonon modes at the Γ point. The arrows at the Pb and Si atoms are proportional to the displacements of each atom in the given vibrational excitation. The lowest optical Pb phonons are mostly parallel to the surface, especially in mode 4 (0.39 THz) and mode 6 (0.75 THz). The optical phonons at higher energies are mixed vertical and parallel excitations, e.g. mode 44 (2.08 THz) and mode 46 (2.18 THz). The phonon bands highest in energy, e.g. mode 47 (2.26 THz) and mode 49 (2.42 THz) correspond to Pb atoms in the surface and subsurface layers oscillating with opposite phase.

The obtained spectra can be compared to calculations of phonon spectra of free-standing Pb films with (1×1) unit cell [107, 120]. Also in these films, a stiffening of the surface modes

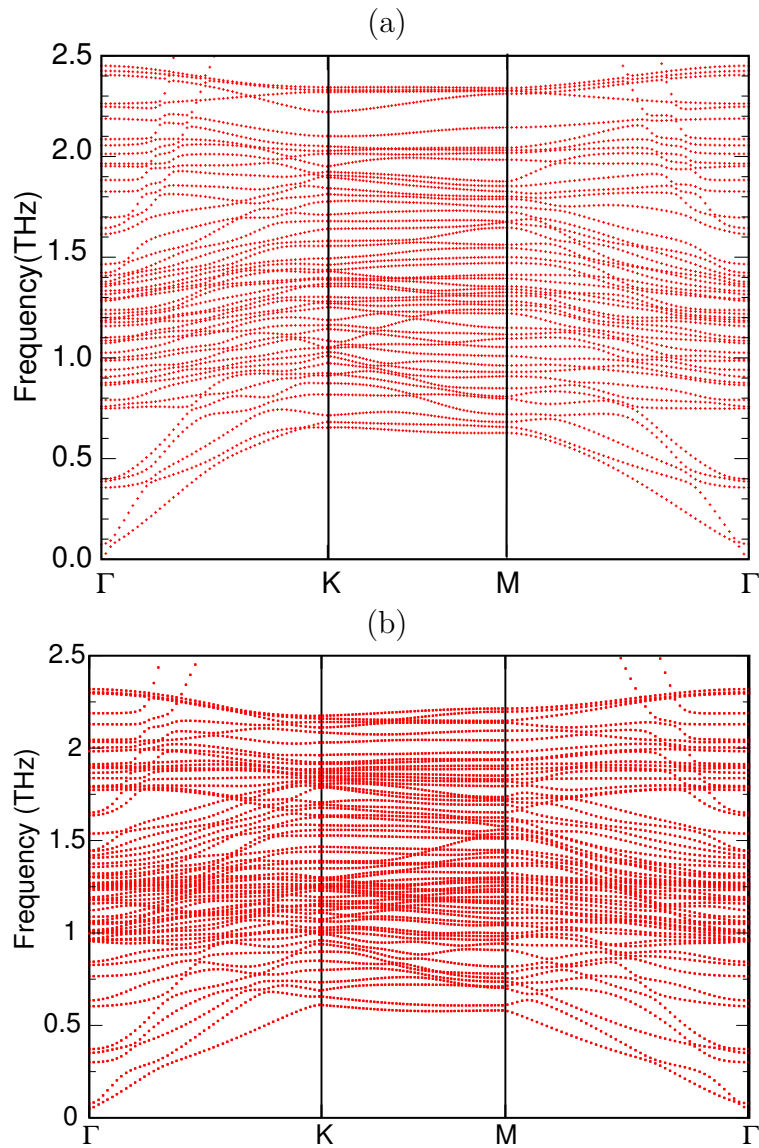


Figure 5.16: Phonon spectrum of Pb/Si(111) ($\sqrt{3} \times \sqrt{3}$) for (a) 4 ML (b) 5 ML of Pb.

is found in the calculations. However, in the free-standing films, the maximum Pb phonon frequency is found in films with an odd number of layers. This is in contrast to our finding of the 4 ML Pb film having a higher surface phonon mode than the 5 ML film. The difference in the eigenmodes of a film on a substrate and a free-standing film can be understood as a consequence of different boundary conditions. For the highest-lying optical phonon modes, the Si substrate acts effectively as a fixed boundary (in Fig. 5.17, the motions of the atoms in the lowest Pb layer are almost invisible). In contrast, in a free-standing film, a layer at rest occurs only in the central layer of a film with an odd number of layers in case of a mode with odd symmetry. Hence it is not surprising that our results differ from the previous studies using free-standing films.

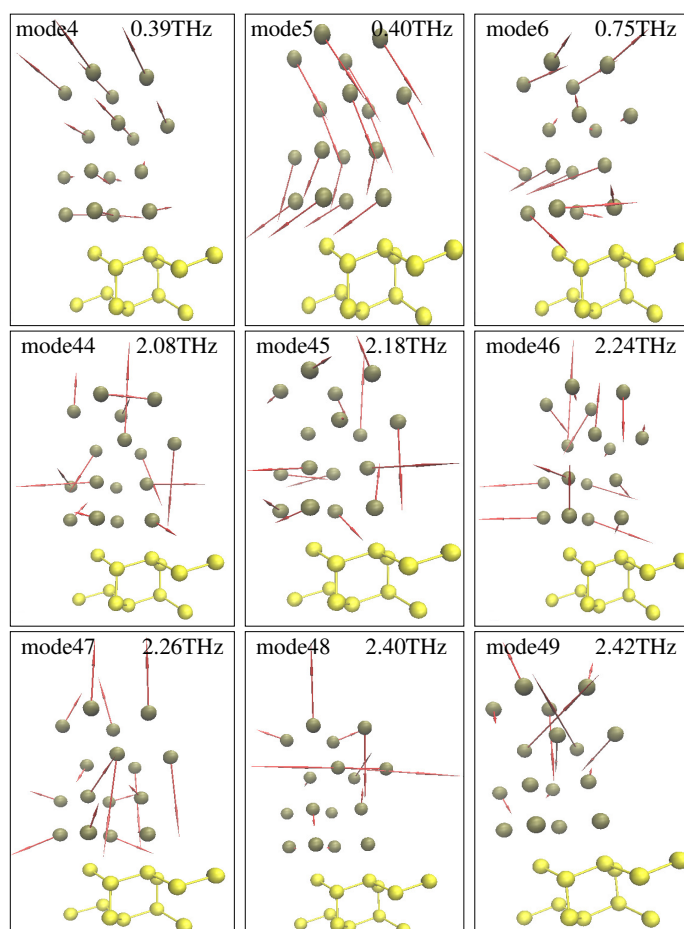


Figure 5.17: Side view of 4 ML Pb (black spheres) on Si(111) (yellow spheres). Atomic displacements for selected phonon modes of Pb/Si(111) ($\sqrt{3} \times \sqrt{3}$) are indicated by the arrows. The displacement of the Si atoms can not be seen in the Figure due to its small size.

For the effect of spin-orbit coupling on the phonon frequencies, we refer to the literature, Ref. [107]. There it has been shown that, for free-standing Pb films, inclusion of spin-orbit coupling results in a slightly larger lattice constant of Pb and leads to slightly softer phonon

modes but little changes in the overall features of the phonon spectrum.

5.7 Electron-Phonon matrix element and deformation potential

In this chapter, main interest in the Pb films stems from experiments addressing the unoccupied electronic states and their dynamics [61]. In this context, the question arises what is the role played by electron-phonon scattering, in addition to electron-electron scattering, in the relaxation of hot photo-excited carriers. In the literature, a considerable number of theoretical studies addressing electron-phonon coupling in thin Pb films near the Fermi energy [14, 75, 101] can be found. However, these studies, motivated by the possibility of phonon-induced superconductivity in Pb films, do not provide information about the electron-phonon coupling in the quantum well states that are typically 0.5 eV to 1.3 eV above E_F . Since these states are unoccupied in thermal equilibrium, only specially designed pump-probe experiments are able to populate them and thus can teach us about their dynamical properties. From the theoretical side, calculations addressing the electron-phonon coupling in these high-lying electronic states are elusive.

I calculate the electron-phonon coupling for the QW states in Pb films for the acoustic and for selected optical phonon modes. Since the QW states form discrete levels similar to those encountered in semiconductor quantum well structures, deformation potential theory, as widely-used in semiconductor physics, may be applied. According to the deformation-potential theorem [95], the deformation potential in a given electronic state can be obtained by evaluating the shift of its electronic eigenenergy under a perturbation of the atomic positions. The atomic displacements belonging to the optical phonon modes are taken from the eigenvectors of the dynamical matrix as provided by the PHONOPY program package.

The ionic displacements can be defined with in a frozen-phonon with momentum \mathbf{q} as:

$$u_{lj,\alpha} = u_{j,\alpha}(\mathbf{q})e^{i\mathbf{q}\cdot\mathbf{R}_{lj}} \quad (5.8)$$

where l, j and α are the lattice indexes, different atoms in the unit cell, and Cartesian index, respectively. In DFT point of view, the variation of the Kohn-Sham potential, δV_{KS} , can be defined up to linear order of atomic displacement in the α direction of atom at \mathbf{R}_{lj} , while keeping all other atoms fixed as :

$$\delta V_{KS}(\mathbf{r}) = \sum_{lj} u_{lj,\alpha} v_{j,\alpha}(\mathbf{r} - \mathbf{R}_{lj}) \quad (5.9)$$

Therefore, electron-phonon matrix element belonging to the same band can be defined as :

$$\begin{aligned} \langle \mathbf{k} + \mathbf{q} | \delta V_{KS} | \mathbf{k} \rangle &= \sum_{lj} u_{lj,\alpha} \langle \mathbf{k} + \mathbf{q} | v_{j,\alpha}(\mathbf{r} - \mathbf{R}_{lj}) | \mathbf{k} \rangle \\ &= \frac{1}{\Omega} \int_{cell} d\mathbf{r} \varphi_{\mathbf{k}+\mathbf{q}}^*(\mathbf{r}) \varphi_{\mathbf{k}}(\mathbf{r}) \sum_{lj} u_{j,\alpha}(\mathbf{q}) \\ &\quad e^{-i\mathbf{q}(\mathbf{r}-\mathbf{R}_{lj})} v_{j,\alpha}(\mathbf{r} - \mathbf{R}_{lj}) \end{aligned} \quad (5.10)$$

$\varphi_{\mathbf{k}}^*$ is periodic part of the Bloch KS orbitals and Ω is cell volume.

The displacement $u_{j,\alpha}(\mathbf{q})$ of atom j for a mode with wave vector \mathbf{q} can be decomposed

according to

$$u_{j,\alpha}(\mathbf{q}) = u_\alpha(\mathbf{q}) + \delta_{j,\alpha}(\mathbf{q}) \quad (5.11)$$

into a long-ranged acoustic part $u_\alpha(\mathbf{q})$ that is accompanied by a deformation of the unit cell and a relative displacement $\delta_{j,\alpha}(\mathbf{q})$. The index α refers to the Cartesian components of the displacement vectors. After rescaling by atomic mass factors, these displacements, with either positive or negative sign, are applied to the atomic positions in the ground state, and a new electronic structure is calculated for these fixed positions of the atoms. In this way, we perform a series of frozen-phonon calculations, similar to the work of Yndurain and Jigato for thicker films [128].

In the deformation potential approach, the electronic eigenvalues experience a shift that is linear in the strain in case of acoustic phonons and linear in the mode amplitude δ_j for optical phonons. To account for these effects in a model, one would add the terms $H' = \Xi \cdot \epsilon$ and $H'' = D_j \delta_j$ to the Hamilton operator. Here for long-wavelength acoustic phonons, the perturbation is locally equivalent to a compression or a shear deformation of the unit cell described by the elements of the elastic strain tensor $\epsilon_{\alpha\beta}$, and Ξ is the tensor of the acoustic deformation potential. In the present case of a hexagonal surface lattice, it is sufficient to distinguish between isotropic in-plane strain due to longitudinal acoustic (LA) phonons and shear strain ϵ_{xy} due to transversal acoustic (TA) phonons. Thus, the acoustic deformation potential Hamiltonian reads $H' = \Xi_{LA} \frac{1}{2}(\epsilon_{xx} + \epsilon_{yy}) + \Xi_{TA} \epsilon_{xy}$. The deformation potential Ξ_{LA} has been extracted from the shifts of the DFT eigenvalues in a unit cell with $\pm 2\%$ strain applied. In the VASP code (as in any plane-wave DFT code), it is required to define a unique reference point to compare the energy eigenvalues in calculations performed with different unit cells. We use the electrostatic potential in the vacuum between the slabs as such a reference point. For calculating the deformation potential Ξ_{TA} , we use strained unit cells where the angle ϕ between the basis vectors in the xy -plane, $\phi_0 = 60^\circ$ has been changed to $\phi = \phi_0 + \Delta\phi$ while the area of the unit cell is preserved. The resulting pure shear strain is given by

$$\epsilon_{xy} = \frac{1}{2} \left(\sqrt{3} + \frac{1}{\sqrt{3}} \right) (\cos \Delta\phi - 1), \quad \epsilon_{xx} = \epsilon_{yy} = 0$$

In the calculations, we use $\Delta\phi = \pm 3^\circ$ and perform a linear fit to the shifted DFT eigenvalues in order to extract Ξ_{TA} . We note that, besides the linear shifts, contributions to second order in ϵ_{xy} are noticeable. Using second quantization for the phonons, the contributions of electron-phonon coupling to the Hamiltonian can be written

$$H' = \Xi_{\alpha\beta} \sqrt{\frac{\hbar}{2M\omega_j}} e_{j,\alpha} i q_{j,\beta} \left(a_j e^{i\mathbf{q}_j \mathbf{r}} - a_j^\dagger e^{-i\mathbf{q}_j \mathbf{r}} \right) \quad (5.12)$$

$$H'' = D_k \sqrt{\frac{\hbar}{2M\omega_k}} \left(a_k e^{i\mathbf{q}_k \mathbf{r}} - a_k^\dagger e^{-i\mathbf{q}_k \mathbf{r}} \right) \quad (5.13)$$

Here, a and a^\dagger are the annihilation and creation operators of the phonons of mode j or k (acoustic or optical) with wave vector \mathbf{q} . The \mathbf{q} -dependent phonon frequencies of these branches are ω_j or ω_k , respectively, and \mathbf{e}_j is the polarization unit vector of the acoustic phonon. α and β are Cartesian indices, and M is the atomic mass of Pb.

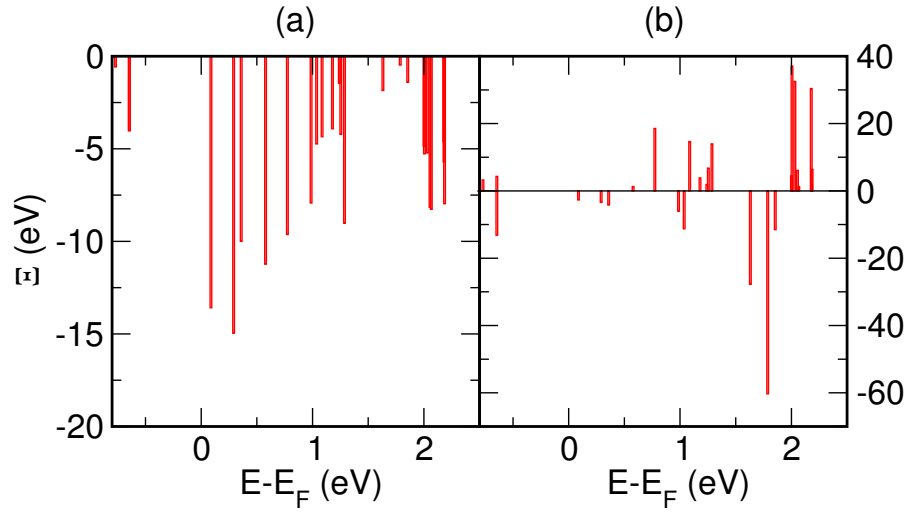


Figure 5.18: Deformation potentials Ξ_{LA} and Ξ_{TA} for electron-phonon coupling to acoustic phonons in a 4 ML Pb/Si(111) film. Results for electronic bands at the Γ point are shown for electrons in an energy range between $E_F - 1\text{eV}$ and $E_F + 2.5\text{eV}$. The gap below E_F is reminiscent of the energy gap in bulk silicon: the metallic states introduced by the Pb film are absent at the Γ point at E_F .

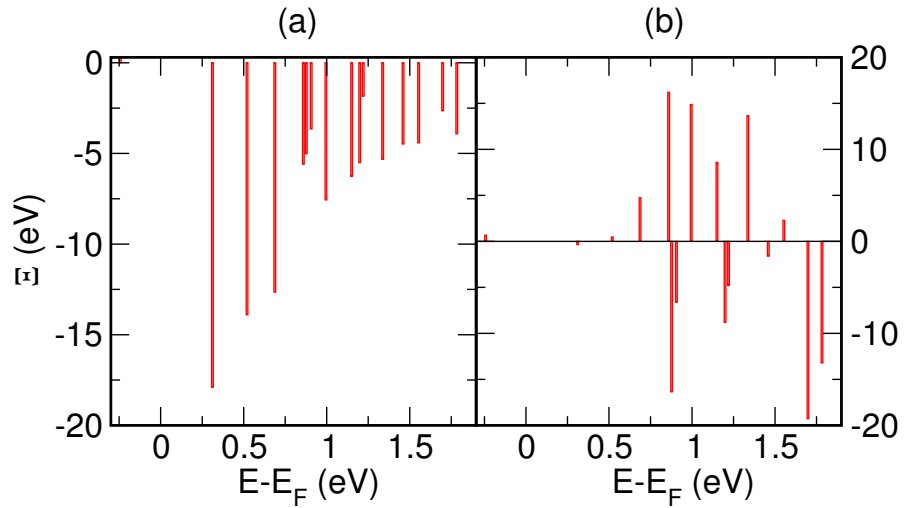


Figure 5.19: Deformation potentials Ξ_{LA} and Ξ_{TA} for electron-phonon coupling to acoustic phonons in a 5 ML Pb/Si(111) film. Results for electronic bands at the Γ point are shown for electrons in an energy range between $E_F - 0.5\text{eV}$ and $E_F + 2\text{eV}$.

Table 5.2: Deformation potentials for the states QWR, QW3b, QW4 and, QW4b (see Table 5.1) for the 4 ML and 5 ML Pb film. The acoustic deformation potentials Ξ_{LA} and Ξ_{TA} are given in eV.

		QWR	QW2b	QW3b	QW4b	QW4
4 ML	Ξ_{LA}	-10	-	-4.0	-1.9	-
4 ML	$ \Xi_{TA} $	4.20	-	3.87	28	-
5 ML	Ξ_{LA}	0.29	-5.6	-7.6	-	-3.9
5 ML	$ \Xi_{TA} $	0.66	16.2	8.6	-	19.3

The results of scalar-relativistic calculations for the energy shifts of electronic bands at the Γ point are displayed in Figures 5.18 to 5.21. Results of calculations including spin-orbit interaction are presented in Fig. 5.24. Apart from the band splitting due to the spin-orbit interaction, the magnitude of the deformation potentials is found to be similar to the scalar-relativistic case. We start with a discussion of the effect of acoustic phonons (Fig. 5.18 and 5.19). It is observed that the hydrostatic deformation potential (Fig. 5.18a and 5.19a) Ξ_{LA} is negative in all states. This means that a lateral compression of the Pb film lowers the energy of the unoccupied electronic states. This finding can be rationalized in the following way: The lateral compression of the atoms is accompanied by an expansion along the surface normal, as required by Poisson's ratio. Hence, the confining potential in z direction, perpendicular to the film, is widened, and the electronic states in this potential move down in energy. For pure shear strain, both positive and negative shifts are observed (Figs 5.18b and 5.19b), i.e. Ξ_{TA} may have either sign. The numerical values are collected in Table 5.2. Qualitative conclusions can be drawn by comparing these values with deformation potentials of known materials. The shear deformation potential Ξ_{TA} in the conduction band minima of Si is known [123] to be 8.7 eV, which is comparable in magnitude to the values we obtain for Pb QW states. For Si, a characteristic time scale for the relaxation of hot electrons due to electron-phonon scattering of 1.5 ps has been reported [125]. Thus, we expect a similar time scale for the relaxation of hot electrons in Pb film. This expectation is in accord with the typical time of 2 ps for which a temperature rise of lattice vibrations is experimentally observed in Pb films[134].

For optical modes, the response of the electronic states strongly depends on the type of mode. Results for the 4 ML Pb film for the phonon modes 46, 47, and 48, whose displacement patterns are displayed in Fig. 5.17, are shown in Fig. 5.20.

The interface state (labelled IS) displays strong positive deformation potentials D_{46} and D_{47} . This is in line with the observation that the modes 46 and 47 display sizeable displacements (Fig. 5.17) of the Pb atoms in the interface layer which affect the bond distances between Pb and Si. The deformation potential of the unoccupied QWR is found to be small compared to IS but may show either sign. This difference in the coupling strength to phonons may explain why the spectral feature assigned to QWR is considerably sharper than the spectral feature of IS (centred at -0.9 eV) in Ref. [96]. For the several degenerate states belonging to QW3b, the optical phonons lift the degeneracy and lead to a splitting of the states. Therefore, the deformation potential in the energy range above 1 eV is large

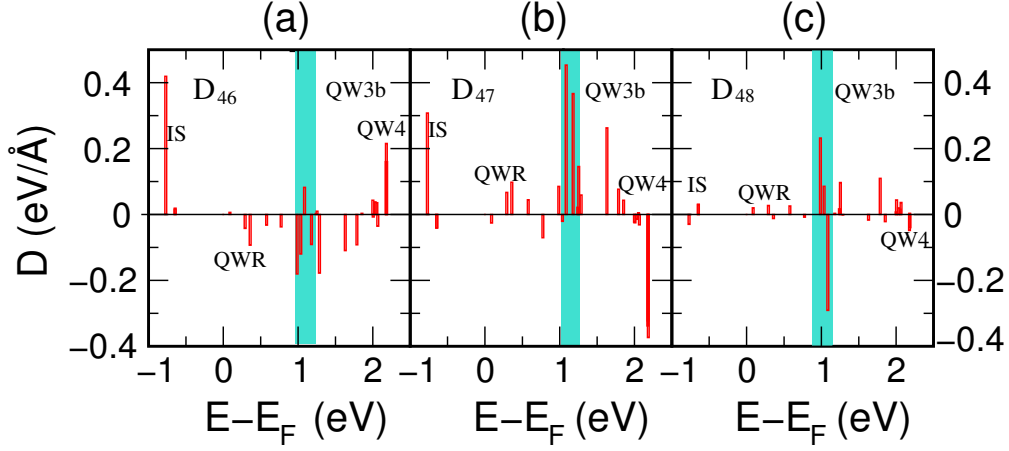


Figure 5.20: Deformation potentials D_{46} , D_{47} , and D_{48} for electron-phonon coupling to the three highest-lying Pb optical phonons in a 4 ML Pb/Si(111) film. Results for electronic bands at the Γ point are shown for electrons in an energy range between $E_F - 1\text{eV}$ and $E_F + 2\text{eV}$. The energy range of the quantum well state QW3b has been shaded for clarity.

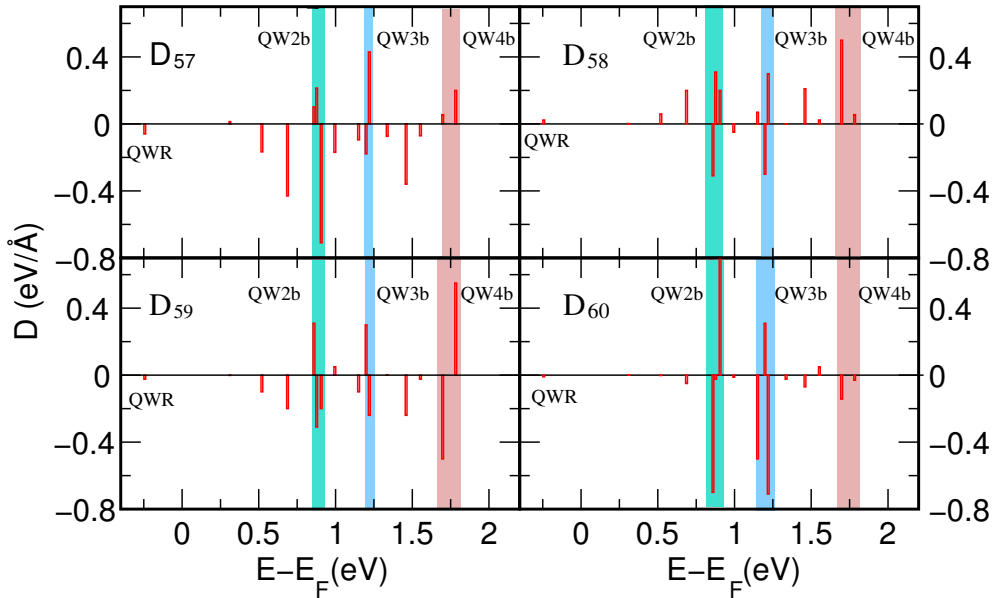


Figure 5.21: Deformation potentials D_{57} , D_{58} , D_{59} , and D_{60} for electron-phonon coupling to the three highest-lying Pb optical phonons in a 5 ML Pb/Si(111) film. Results for electronic bands at the Γ point are shown for electrons in an energy range between $E_F - 0.5\text{eV}$ and $E_F + 2.5\text{eV}$. The energy ranges of the quantum well states QW2b, QW3b and QW4b have been shaded for clarity.

in absolute terms but shows opposite sign for adjacent states belonging to the same group of QW3b. For the determination of phonon-induced lifetimes of electronic excitations, total rates integrated over all phonon branches and phonon wavevectors are required. Motivated by this, we have performed additional test calculations for a number of optical phonon modes. The results Fig.5.25 indicate that the sensitivity of specific quantum well states to deformation potential scattering for low-lying optical phonons follows the same trend as for the high-lying modes 46, 47 and 48.

For 5 ML of Pb, the acoustic deformation potentials (Fig. 5.19) are qualitatively similar to the 4 ML case, but there are some quantitative differences. We observe that the filled QWR is rather insensitive to phonons and thus shows small Ξ_{LA} and Ξ_{TA} . Also for the optical modes (Fig. 5.21), the QWR displays only small deformation potentials. The relative insensitivity of the QWR to displacements of the Pb atoms is attributed to the finding that only part of the QWR electronic wavefunction (cf. Fig. 5.14, left) is located within the Pb layers, while the major part, extending into the Si substrate, is hardly affected by the displacements of the Pb atoms. For the higher-lying quantum well states QW2b, QW3b, and QW4b, we again observe a splitting of degenerate states in the presence of a phonon (Fig. 5.21), and hence deformation potentials D_{57} , D_{58} , D_{59} , and D_{60} may have positive or negative sign. Comparing the results for 4 ML and 5 ML Pb, we find that the optical deformation potentials are generally somewhat larger for the 4 ML film. This is in qualitative agreement with previous theoretical studies [128], in which an oscillation of the electron-phonon coupling of QW states between films with even and odd number of layers had been observed with the stronger coupling in even-layered films. Thus, our calculations indicate that the oscillatory behavior characteristic of the electronic structure of Pb films is reflected in the strength of the electron-phonon coupling, too.

Earlier theoretical studies addressing the Eliashberg function in thin Pb films [73, 101, 107] have found oscillations of the electron-phonon coupling as well. In addition, the oscillatory behavior of the Eliashberg function is supported by experiments measuring the peak broadening in photoemission spectra of even-layered and odd-layered Pb films [132]. However, in these studies the interest was on the states at the Fermi surface which are formed by highly dispersive $6p_{x,y}$ bands, whereas our interest is in QW states at the Γ -point formed by $6p_z$ states. Thus, the previous results are not directly comparable to ours. In addition to the high-lying optical modes whose deformation potentials are presented above, we show in Fig. (5.22) the deformation potential of some low-lying modes, mode 4 to mode 7, at 0.4 THz. It is found that the sensitivity pattern of the quantum well states is similar for both high-lying and low-lying optical modes. Again, the electronic eigenvalues belonging to the quantum well state QWR3 show the highest sensitivity to optical phonons. However, the deformation potential of the interface state IS (which is an occupied electronic state at -0.9 eV) is smaller in case of the low-lying optical modes as compared to the high-lying ones. When calculating total electron-phonon scattering rates for electronically excited states, only the unoccupied states are of interest. Thus, to a good approximation, the same values of D may be used for all phonon modes within the range of optical frequencies.

It is noteworthy that the oscillations between even-layered and odd-layered films observed in the Eliashberg function are mainly caused by modulations of the *electronic* density of states with the number of layers, whereas our present study addresses oscillations in the matrix element of electron-phonon coupling. Moreover, the previously reported oscillations had opposite phases to ours, with the odd-layered films displaying the higher electron-phonon

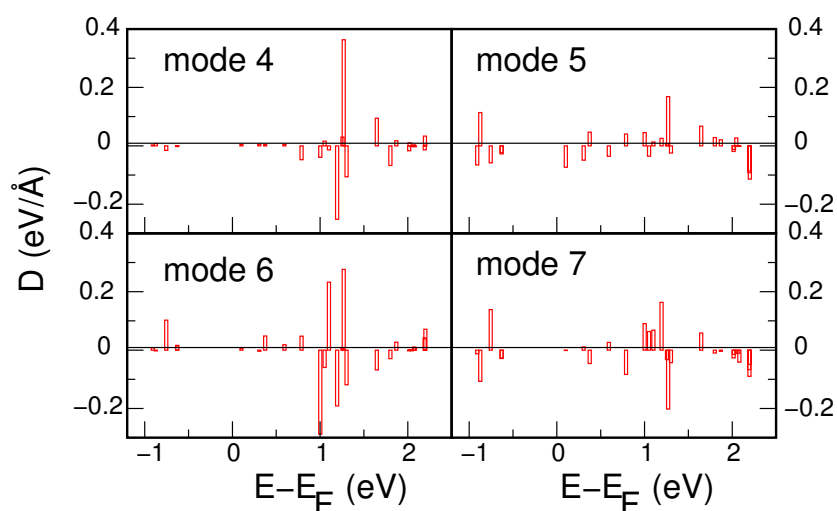


Figure 5.22: Deformation potentials D_4 , D_5 , D_6 and D_7 for electron-phonon coupling to four low-lying Pb optical phonons in a 4 ML Pb/Si(111) film. Results for electronic bands at the Γ point are shown for electrons in an energy range between $E_F - 1$ eV and $E_F + 2.2$ eV.

coupling [101], whereas we find larger deformation potentials in the even-layered films.

5.8 Spin-orbit coupling

Spin-orbit coupling one of the most important mechanisms which couples the spin of an electron to its orbital motion. In following I will show you the effect of spin-orbit coupling (SOC) in the phonon dispersion and electron-phonon coupling of thin layers Pb films on the Si substrate in 4ML and 5ML.

5.8.1 Effect of spin-orbit coupling on electronic band structure

When spin-orbit coupling is included in the calculations of the Pb films on Si(111), the lack of inversion symmetry, due to the presence of the substrate, results in a splitting of bands. In accord with Rashba physics, the splitting vanishes at the Γ point but becomes notable in the interior of the Brillouin zone. For the QWR state in the 4 ML Pb film that shows downward dispersion toward the Brillouin zone center, a maximum splitting of 60 meV is observed. For the QW3b state starting at 1.17 eV and dispersing downward, the splitting becomes as large as 100 meV. In the 5 ML Pb film (Fig 5.23), the occupied QWR state shows a maximum splitting of 50 meV. The splittings in the QW2b and QW3b states away from the Γ point are of similar size. In both cases, spin-orbit coupling in the QW states can be considered a small correction to the scalar-relativistic level scheme.

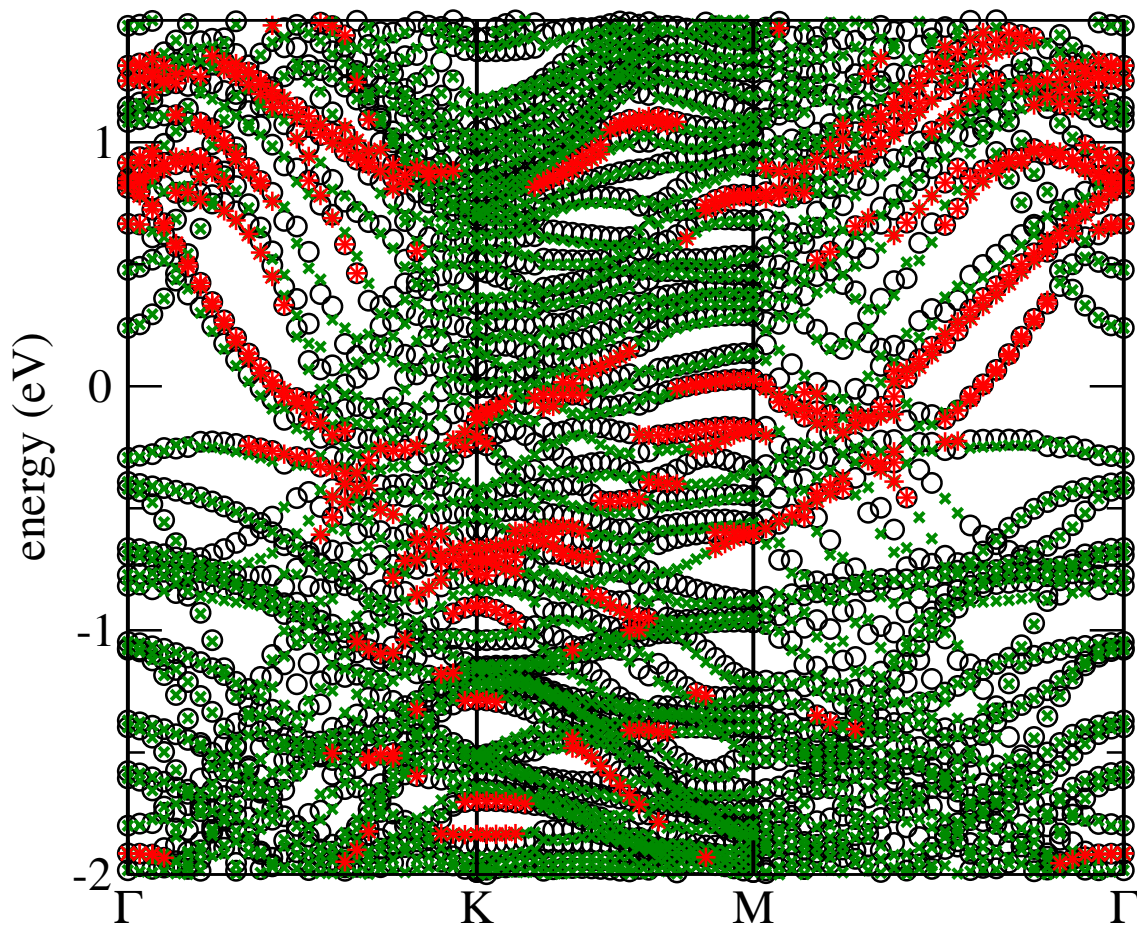


Figure 5.23: Electronic band structure of 5ML Pb:Si(111) in $\sqrt{3} \times \sqrt{3}$. The green cross and the black circle show nearly degenerate eigenstates that approximately correspond to the two spin states. The red symbols mark bands with distinct Pb $6p_z$ character indicative of quantum well states.

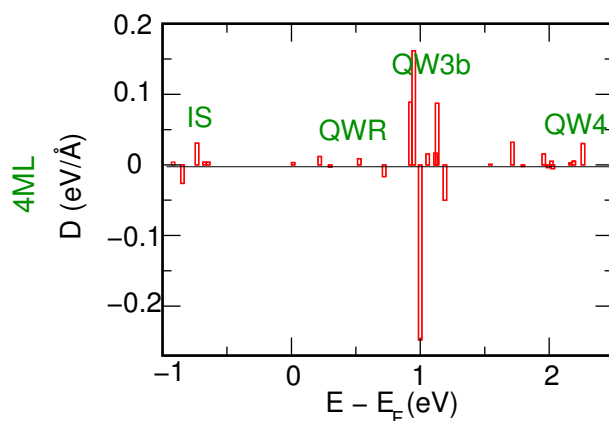


Figure 5.24: Optical deformation potential D_{48} for phonon mode 48 in a 4 ML Pb/Si(111) slab at the electronic Γ point. The figure is analogous to figure 10(c) in the paper, but with spin-orbit coupling included.

5.8.2 Effect of spin-orbit coupling on deformation potentials

Previous calculations [47, 107] demonstrated that the Eliashberg function was strongly enhanced when spin-orbit interaction was included while the density of states at the Fermi level was essentially unaltered. In order to assess the role of the spin-orbit interaction for the strength of electron-phonon coupling, I perform calculations with the software VASP using spinor wavefunctions. The spin-orbit coupling (SOC) is a consequence of relativistic physics and is strongest in the regions close to the nuclei. In VASP the spin-dependence of the electronic potential in these regions is treated within the projector-augmented wave method. For the SOC calculations, a Pb pseudopotential including the occupied $5d$ shell and a plane-wave cut-off of 500 eV to describe the electronic wave functions were employed. I use the bulk lattice constant of Pb, which – with these settings – was obtained as 4.11Å. The atomic positions of all mobile atoms in the Pb film and Si substrate were re-optimized in the presence of the SOC term in the Hamiltonian and using the lattice constant for Pb consistently obtained with SOC. For the optical deformation potential D_{48} shown in Fig. (5.24), the phonon eigenvector obtained from the scalar-relativistic calculations (shown in Fig.(5.8)) was used to define the displacement pattern of the atoms.

As described in chapter II, the lack of inversion symmetry due to the presence of the substrate in combination with the SOC term in the Hamiltonian may result in a splitting of the electronic bands. In case of an approximate description by a Rashba Hamiltonian being valid, one would expect this splitting to vanish at the Γ point. This is indeed what is observed in our DFT calculations of the QW states. For this reason, the effect of SOC is hardly noticeable at the Γ point. In Fig. 5.23, despite the different lattice constant used and differently relaxed atomic positions, both the spectrum of electronic states and the size of the deformation potentials are practically the same as in Fig. 5.18(a). Hence, the effect of SOC does not affect the conclusions drawn about the phonon-induced relaxation of electronically excited quantum well states. In addition, I also considered the possible effect of SOC on the deformation potential of optical phonons. As a representative example, we investigate the case of the optical mode 48 of the 4ML Pb/Si(111) film. The calculated deformation poten-

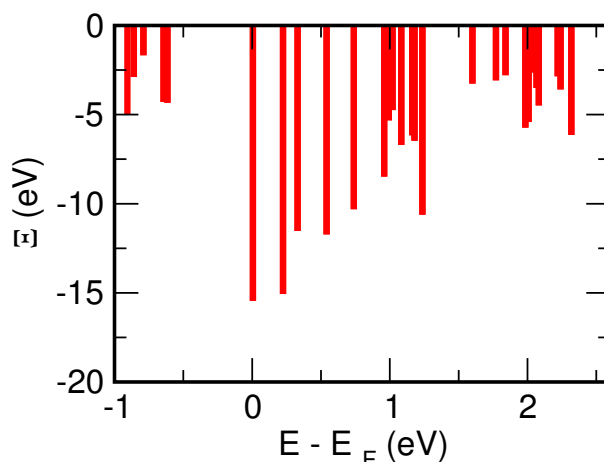


Figure 5.25: Acoustic deformation potential Ξ_{LA} in a 4 ML Pb/Si(111) slab at the electronic Γ point. The figure is analogous to figure 5.8(a), but with spin-orbit coupling included.

tials in the presence of SOC are shown in Fig. 5.24. The behavior in the SOC calculation and the scalar-relativistic calculation is qualitatively similar: The deformation potential D_{48} is largest within the states belonging to QWR3, leading to a splitting of these states under the influence of the optical phonon. Also the magnitude of D_{48} in the individual electronic states is very similar in both the SOC and the scalar-relativistic case. The inclusion of SOC becomes more noticeable when moving away from the electronic Γ point into the interior of the Brillouin zone. Here, some electronic bands show notable splitting due to SOC already in the ground state geometry, as discussed before. For the superconducting properties of Pb films, the effect of electron-phonon coupling on the states close to the Fermi level is of utmost importance. While we do not attempt to study superconducting properties, we can still get a glimpse of the effects to be expected by selecting the \vec{k} -point $\vec{k} = (0, 3/8, 0)$ which is close to a Fermi surface of the 4 ML Pb/Si(111) film. The calculated deformation potentials are shown both in the scalar-relativistic case and in case of SOC in Fig. 5.26. Most notably, the inclusion of SOC has an effect on the density of the electronic energies. When isotropic strain is applied (corresponding to a long-wavelength LA acoustic phonon), *both* the reduced local symmetry around each Pb atom *and* the SOC term in the Hamiltonian contribute to level splitting. As a result, the mean spacing between electronic levels (bands in a 2D representation) is smaller in the SOC case compared to the scalar-relativistic case. At the same time, it is observed that the magnitude of the deformation potentials themselves (i.e., the lengths of the bars in Fig. 5.26) shows only minor changes between the cases with and without SOC. The deformation potentials that I calculate by including spin-orbit coupling in this part are qualitatively and quantitatively *not* very different from those obtained from a scalar-relativistic treatment. One is thus led to the conclusion that the matrix elements at finite momentum transfer to the phonons that contribute to the Eliashberg function are sensitive to spin-orbit interaction whereas the scattering of electrons with vanishingly small momentum transfer studied in our work is rather insensitive. Thus, the electrons in quantum well states around the Γ point appear to be less affected by spin-orbital coupling than the electrons at the Fermi surface of Pb.

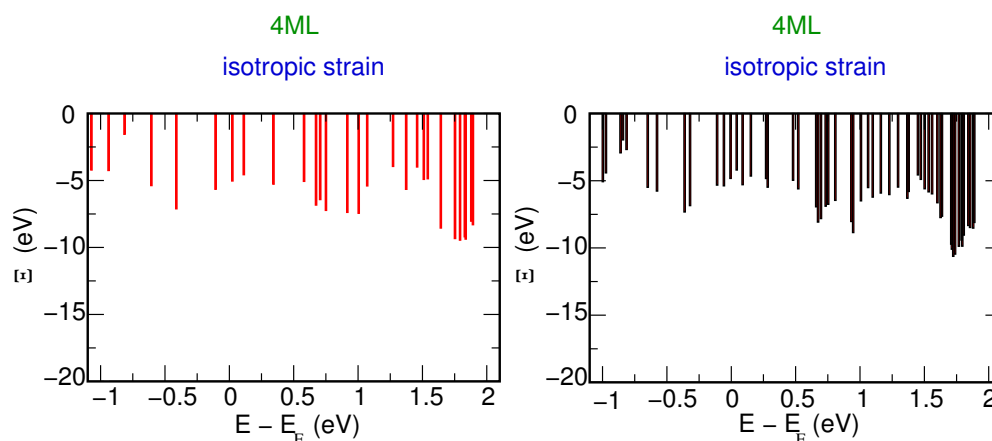


Figure 5.26: Acoustic deformation potential in a 4 ML Pb/Si(111) slab for the electronic states at $\vec{k} = (0, 3/8, 0)$ without spin-orbit coupling (left) and with spin-orbit coupling (right). The splitting of the bands due to SOC is clearly visible, while the overall magnitude of the deformation potentials is less affected by including SOC.

5.9 relaxation time for electron-phonon coupling

The principle idea is simply to combine density matrix dynamics and materials-specific rates from a density functional theory calculation.

As I mentioned in chapter 3, diagonal elements of the density matrix, $f_{n\mathbf{k}} \in [0, 1]$ can show the probability of an electron in state n . To solve our rate equations, we need to compute the quantities $D_{n\mathbf{k}, i\mathbf{Q}}^{n'\mathbf{k}'}$ and $n_{i\mathbf{Q}}(T)$ which enter the decay rates $\Gamma^{(in/out)}$. For the electron-phonon interaction, the couplings are given by

$$|D_{n\mathbf{k}, i\mathbf{Q}}^{n'\mathbf{k}'}|^2 = |D_n|^2 \frac{\hbar}{2\omega_{i\mathbf{Q}} M_{Pb}} \frac{v_{\text{atom}}^{Pb}}{A_{\text{supercell}}} I_{n\mathbf{k}}^{n'\mathbf{k}'} \delta_{\mathbf{k}-\mathbf{k}', \mathbf{Q}},$$

where the *deformation potential* D_n of the n^{th} band is assumed to be independent of the phonon wavevector \mathbf{Q} . The D_n s are obtained from the DFT calculations by evaluating the electronic eigenvalue shift under finite displacements of the atomic positions. So from the deformation potential that I calculated before and phase space, which in mechanics the phase space can be defined as a combination of space position and momentum but here we can explain from fermi golden rule: Fermi's golden rule is an equation for calculating transition rates. The occupation number is the occupation of electrons how fast the electron relaxed and meet the phonon, but it is stimulated in each. Because we have already the phonon then you get two phonons, we get one more phonon. When we have already many phonons it is easier to meet another phonon because the initial has the Bose-Einstein plus one, $n_{\mathbf{Q}} + 1$, It is only the effect of the phonon, it is the phonon temperature, T, and continuously emitted the phonon but if the lattice vibrates already then one phonon more can produce, and this

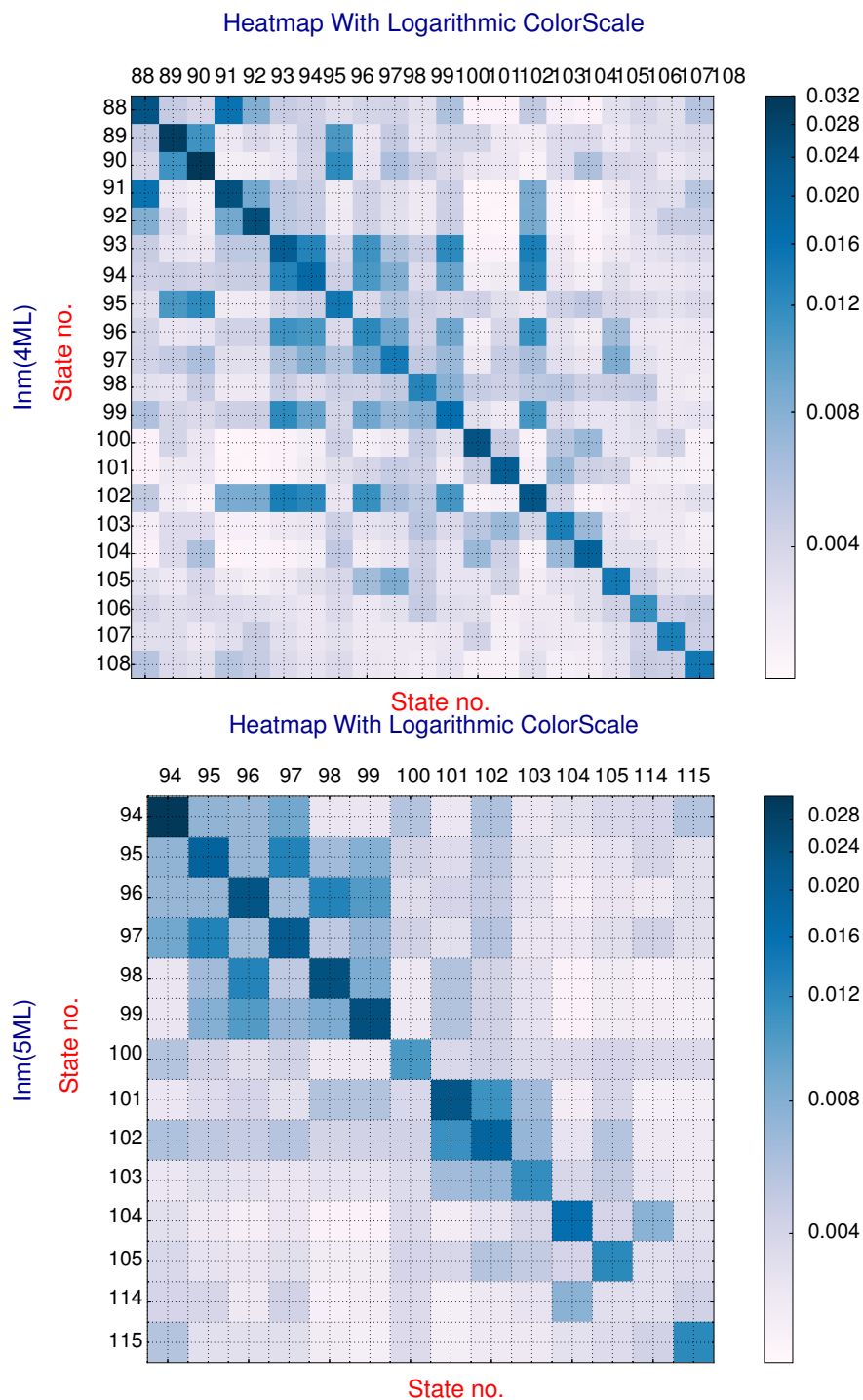


Figure 5.27: I_{nm} represents the overlap integral associated with the electron interaction (electron-phonon wavefunction integral) for 4ML Pb (upper part) and for 5ML Pb films (lower part).

goes with the factor of $n_Q + 1$, and this is shown when the lattice already shake it would be easier to produce another phonon. Within deformation potential theory, we show that the overlap matrix element can be expressed as

$$I_{n\mathbf{k}}^{n'\mathbf{k}'} \approx A_{\text{supercell}}^{-1} \iiint dx dy dz |\Psi_{n'\mathbf{k}'}(x, y, z)|^2 |\Psi_{n\mathbf{k}}(x, y, z)|^2. \quad (5.14)$$

In order to simplify the calculations, we calculate I explicitly only for combinations of two \mathbf{k} vectors, $\mathbf{k}_x = (1/4, 0, 0)$ and $\mathbf{k}_y = (0, 1/4, 0)$. For other combinations of \mathbf{k} values, we use an interpolation technique:

$$\cos \theta = \frac{\mathbf{k}\mathbf{k}'}{kk'}, \quad I_{n\mathbf{k}}^{n'\mathbf{k}'} = \begin{cases} I_{n\mathbf{k}_x}^{n'\mathbf{k}'_x} \cos 2\theta + I_{n\mathbf{k}_x}^{n'\mathbf{k}'_y} \sin 2\theta, & \text{if } \cos 2\theta \geq 0 \\ -I_{n\mathbf{k}_y}^{n'\mathbf{k}'_y} \cos 2\theta + I_{n\mathbf{k}_x}^{n'\mathbf{k}'_x} \sin 2\theta, & \text{if } \cos 2\theta < 0 \end{cases}$$

5.9.1 Coupling to heat bath of phonons and mode conversion

In the harmonic theory that we use for calculation of phonon dispersion, each phonon would stay on its own, but in anharmonic case, the harmonic phonon is no longer an eigenvector and it couples with other phonons. Therefore we have mode conversion; meaning that one phonon can decay into other phonon modes, for example optical modes or acoustic modes. In our simulations, we consider two phonon baths with different temperature, T_1 and T_2 which are related to phonon bath1 and phonon bath2, respectively. It means in reality after some time the modes becomes damped and other modes can start to be excited so for this reason the energy can flow from one bath to other bath.

In the paper by Sakong [99] the it time takes for the in-plane mode to be converted to a mode perpendicular to the surface was calculated as $\tau_2 = 100$ ps. This time scale is the mode conversion between high-lying optical modes in the Pb layer and the acoustic modes. The Bose-Einstein distribution functions $n_{i\mathbf{Q}}(T)$ describe the occupation of phonon mode i with wave vector \mathbf{Q} in a phonon bath at temperature T . In the simulations, we use two phonon baths with different temperature T_1 and T_2 :

- Surface and interface phonons of the Pb layer in the 2.3 to 2.5 THz range (modes 43, 44, 45, 46, 47, 48 in the 4 ML film) are very strongly coupled to the electrons in the quantum well state, therefore, coupling to a separate bath 2 with temperature T_2 .
- All lower-lying Pb phonon modes are coupled to the phonon bath 1 at temperature T_1

For example for the 5ML the surface and interface phonons of lead layer in the 2.1 to 2.3 THz range couple very strongly to the electrons of the QWSs. so the highest lying modes such as modes 57, 58, 59 and 60 are coupled to a separate bath with temperature T_2 . All lower-lying modes coupled with the phonon bath with temperature T_1 . In Fig.(5.28) show the energy per mode as function of time for different modes for both 4ML and 5ML Pb:Si(111). For both 4ML and 5ML the mode with the highest electron-phonon coupling has the highest energy per mode. In this figure we can see clearly differences between modes. τ_2 can define the time scale on which the two phonon baths exchange energy. From Sakong's work we already know that the $\tau_1 = 2000$ ps which is the time it takes to exchange the energy between the acoustic phonons of Si and acoustic phonons of Pb. The hot electrons

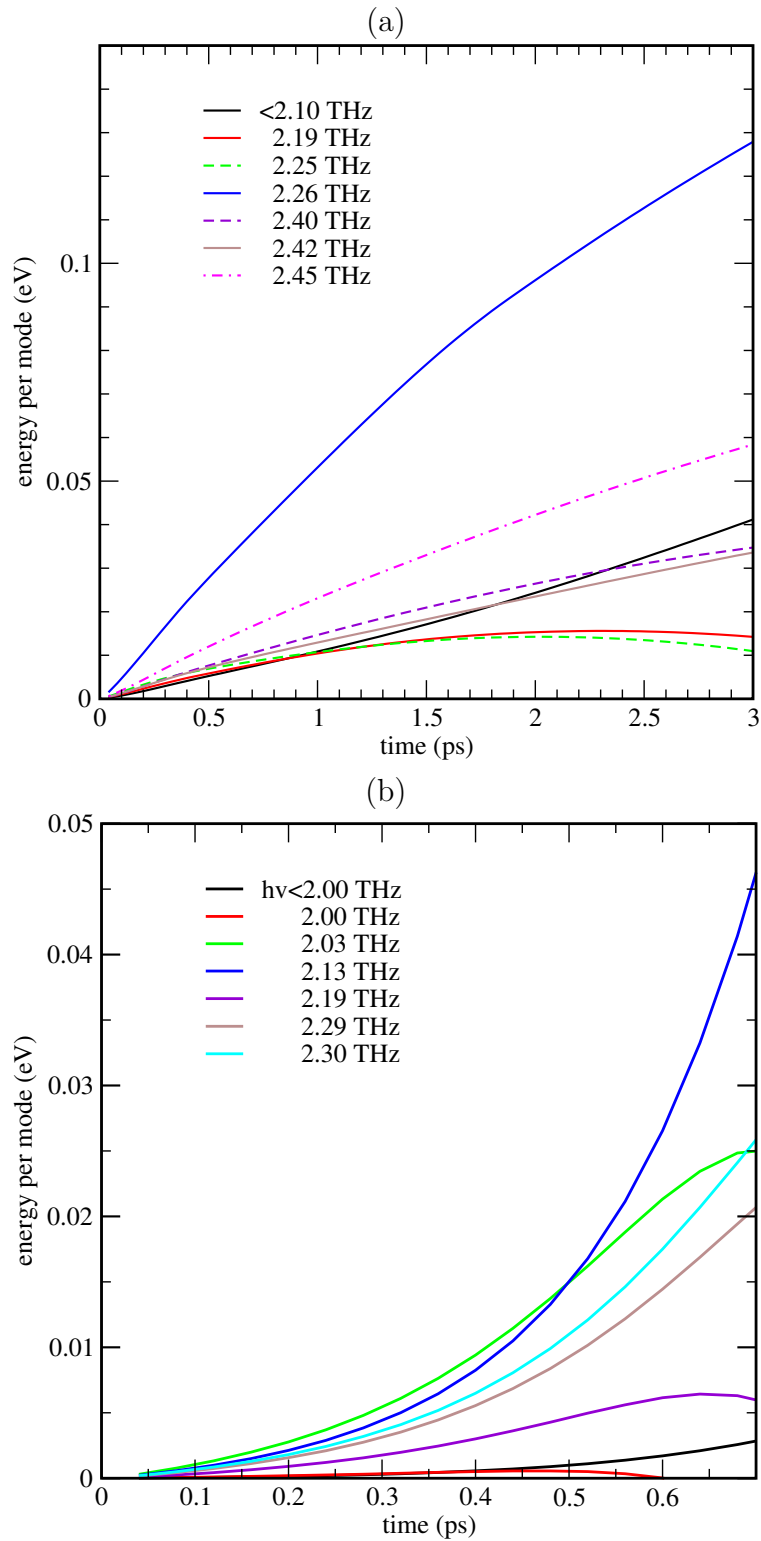


Figure 5.28: (a) and (b) show the energy per phonon mode as function of the time after the electronic excitation for 4ML and 5ML of Pb:Si(111).

mainly give the energy to the phonon bath 2 which are optical modes. This follows from my calculations, because I find that the e_2 is larger than e_1 .

Moreover, the acoustic phonon bath at T_1 may exchange energy with the substrate at constant temperature T_0 , but at a very low rate. The above considerations lead to the following heat bath model

$$\begin{aligned}\frac{dT_2}{dt} &= (T_2 - T_1)/\tau_2 + e_2/c_{V2}, \\ \frac{dT_1}{dt} &= \frac{(T_1 - T_2)c_{V2}}{\tau_2 c_{V1}} + \frac{e_1}{c_{V1}} + \frac{T_1 - T_0}{\tau_1}.\end{aligned}$$

The quantities c_{V1} and c_{V2} denote the heat capacities of phonon bath 1 and 2 which is related to the number of modes in the respective bath. In the classical approximation for the 4 ML slab, we use $c_{V2} = 6k_B$ and $c_{V1} = 42k_B$.

5.9.2 From matrix elements to rate equations

For the numerical simulation of the hot electrons, we consider momentum and energy conservation in such a way that for momentum conservation we have electron with momentum \mathbf{k}' or \mathbf{k} and phonon with the momentum \mathbf{Q} such that

$$\mathbf{k} - \mathbf{k}' = \mathbf{Q} \quad (5.15)$$

As schematically shown in the Fig. (5.29) for the energy conservation, the whole k space is divided into the squares and triangles and electron starts with some energy, ϵ_{ml} and it loses some energy to the phonon, $\hbar\omega$,

$$\epsilon_{ml} - \epsilon_{nk} = \hbar\omega_Q \quad (5.16)$$

so we see there is another energy band, which is final energy, ϵ_{nk} . In other words, the Brillouin zone is divided into some squares and triangles and for some triangles there is an electron dispersion curve that cuts or runs through this triangle. By measuring the length of the path, we apply a certain condition for the energy conservation. As it is shown in the chapter III, the occupation number change and in this formula the δ -function expresses energy conservation in each individual scattering process. They are limited in the available phase space for scattering. There is some factors, δ , in the Eq.3.50 and 3.51 (as I explained before) which measures the phase space for the scattering rate. We need matrix element and another factor which tells us when the particle scatters, how many final states are available for the scattered particle. This information is provided by the phase space. All the electron energies and phonon energies come from my DFT calculations.

The initial condition in our calculation is determined by the optical excitation of the electrons. For estimating that, we calculated the occupation number everywhere. In some places it is stronger than other places. Firstly, we calculated the electronic excitation by means of dipole matrix element; this is done the same way as described by Buecking [16]. Then we have f_{nk} at $t = 0$ for whole $n\mathbf{k}$. We can derive a coupled set of differential equations and cast it into the form of *rate equations* (cf.[103]). The associated decay constants are made up of an electronic and a phononic contribution each, i.e. $\Gamma_{n\mathbf{k}} = \Gamma_{n\mathbf{k}}^{(ee)} + \Gamma_{n\mathbf{k}}^{(ep)}$:

$$\frac{d}{dt}f_{n\mathbf{k}} = \Gamma_{n\mathbf{k}}^{(\text{in})} (1 - f_{n\mathbf{k}}) - \Gamma_{n\mathbf{k}}^{(\text{out})} f_{n\mathbf{k}}$$

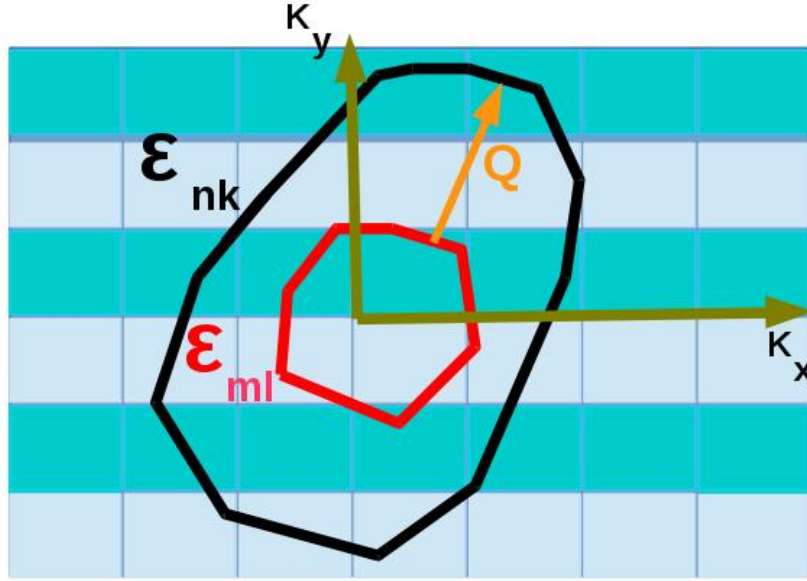


Figure 5.29: Schematic of energy and momentum conservation. Q is phonon vector and ε_{nk} and ε_{ml} are energy of electron in state n and m , respectively.

Γ^{out} terms consist two terms: electron-electron scattering and electron-phonon scattering.

$$\Gamma_{nk}^{out} = \Gamma_{nk}^{out(ee)} + \Gamma_{nk}^{out(ep)} \quad (5.17)$$

$$\Gamma_{nk}^{(in,ep)} = \frac{2\pi}{\hbar} \sum_{\substack{m,i, \\ \mathbf{Q}, \pm}} \left| \mathbf{D}_{nk,i\mathbf{Q}}^{m,\mathbf{k}-\mathbf{Q}} \right|^2 \left(n_{i\mathbf{Q}} + \frac{1}{2} \pm \frac{1}{2} \right) \delta(\varepsilon_{nk} - \varepsilon_{ml} \pm \hbar\omega_{i\mathbf{Q}}) f_{m,\mathbf{k}-\mathbf{Q}}$$

$$\Gamma_{nk}^{(out,ep)} = \frac{2\pi}{\hbar} \sum_{\substack{m,i, \\ \mathbf{Q}, \pm}} \left| \mathbf{D}_{nk,i\mathbf{Q}}^{m,\mathbf{k}-\mathbf{Q}} \right|^2 \left(n_{i\mathbf{Q}} + \frac{1}{2} \mp \frac{1}{2} \right) \delta(\varepsilon_{nk} - \varepsilon_{ml} \pm \hbar\omega_{i\mathbf{Q}}) (1 - f_{m,\mathbf{k}-\mathbf{Q}})$$

$$\Gamma_{nk}^{(out,ee)} = -\frac{2}{\hbar} \text{Im}\Sigma(E) = \frac{(E - E_F)^2}{30\text{fs}(\text{eV})^2}$$

$$\Gamma_{nk}^{(in,ee)} = F(\varepsilon_{nk})N$$

$$F(\varepsilon_{nk}) = \frac{1}{\exp\left(\frac{(\varepsilon_{nk} - E_F)}{k_B T_{el}}\right) + 1}$$

$$N = \frac{\sum_{n,k} \Gamma_{nk}^{out} |\varepsilon_{nk} - E_F| f_{nk}}{\int d\varepsilon g(\varepsilon) |F(\varepsilon_{nk}) - \Theta(E_F - \varepsilon_{nk})| |\varepsilon_{nk} - E_F|}$$

$\Gamma_{nk}^{\prime out}$ (as it is shown in the Eq. (5.17)) is electron-electron scattering and after the scattering the secondary electrons and holes are described by some electronic temperature. We take the Fermi Dirac distribution, $F(\varepsilon_{nk})$, with this temperature. When many electrons are scattered the total energy should be conserved. This Fermi Dirac distribution is added to the existing occupation number. $\Gamma_{nk}^{\prime in}$ is basically a Fermi Dirac distribution with some

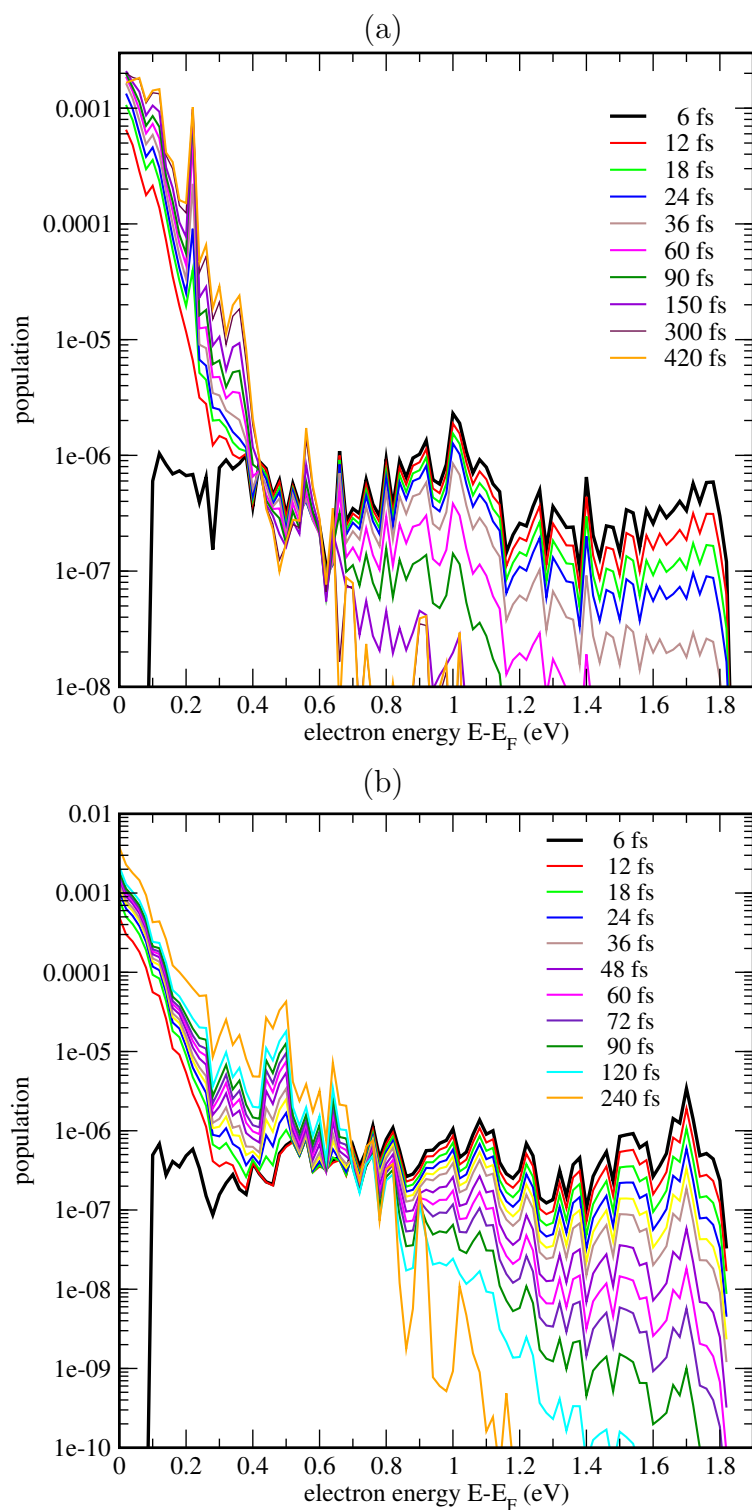


Figure 5.30: (a) and (b) show the population of the electronic states as function of energy (eV) for 4ML and 5ML of Pb:Si(111). The black line shows the initial population generated by a laser pulse with $h\nu = 1.9$ eV. The colorful lines show the relaxed population which results from the numerical solution of the rate equation. $T_{el} = 408$ K.

electronic temperature in it such as 408K, which we use in our calculation.

For the investigation of the ultrafast population dynamics in our system, the quantities which we have to look at are

- $f_{n\mathbf{k}} = \langle \hat{c}_{n\mathbf{k}}^\dagger \hat{c}_{n\mathbf{k}} \rangle$ electronic occupation number
- $n_{i\mathbf{Q}} = \langle \hat{b}_{i\mathbf{Q}}^\dagger \hat{b}_{i\mathbf{Q}} \rangle$ phononic occupation number
- $p_{n\mathbf{k}}^{n'\mathbf{k}'} = \langle \hat{c}_{n\mathbf{k}}^\dagger \hat{c}_{n'\mathbf{k}'} \rangle$ microscopic polarization.

Applying the *Ehrenfest theorem* and invoking the following approximations

- *bath approximation* $\langle \hat{b}_{i\mathbf{Q}}^\dagger \hat{b}_{i\mathbf{Q}} \rangle = n_{i\mathbf{Q}}(\beta) = \frac{1}{e^{\beta\hbar\omega_{i\mathbf{Q}}} - 1}$

At first some bands become occupied when the laser energy is applied. It brings the electron from one band to another. The laser pulse has some photon with the energy such as $\hbar\omega$. The part of energy absorbed with the Pb can be calculated exactly from dielectric function, but here we just make a plausible assumption about the amount of intensity of laser which is absorbed by the Pb layers. In Fig. 5.31 we show the population of electronic states as function of energy (eV) for 4ML and 5ML. First, the dipole transition is calculated, then we do a little electron-electron scattering, but only for 6-fs then we have got some background for the electronic temperature. In the Fig. (5.30), the black line is the earliest time when the rate equation is running, and every 40-fs the output is plotted which is shown in different color and then we get the f_{nk} , the occupation numbers after that time. The electron temperature just gives us the straight line at energies below 0.4 eV because it is a logarithmic figure. In this Fig we can see different peaks, but just two of them in 4ML are decay peaks. When the time advances they go down, but the other ones are growing. Experimentally they do not report that any peaks were growing. One in 1eV and another in 0.66eV for the 4ML Pb: Si (111) come from the dipole excitation. In Fig 5.30 (b) we have more decay peaks at 0.76, 1.08, 1.22, 1.54 and 1.70 eV. Then we extract the data for these decay peaks and plot the population of electronic state as a function of time for both 4ML and 5ML (Fig. 5.31).

Now I discuss the time-dependence of the populations in Fig. 5.31. At energies above 1eV everything is dominated by the electron-electron scattering only to decay here. From the Fig. 5.31, I calculate the role of electron-phonon scattering for the peaks 0.66eV and 1eV for 4ML and the peak at energy 0.76eV for the 5ML Pb:Si(111). The analysis of the data shows me that in 0.66eV the relaxation time for the electron-phonon part is 933 fs and the total relaxation time is 98 fs. For the peak at 1eV, the relaxation time related to the electron-phonon part is 420fs and the total relaxation time, which includes the electron-electron part plus the electron-phonon part, is 47 fs. I calculate the relaxation time in 5ML at the decay peak with energy 0.76eV and the contribution of electron-phonon scattering is 8ps and the total relaxation time is 61fs. As it is clear from the these data, the slope mostly comes from electron-electron scattering and a little comes from electron-phonon scattering. At 0.66 eV one can see better the role of electron-phonon scattering. In the Fig. 5.31 it is clear that the relaxation time for electron-electron scattering is faster than for electron-phonon scattering.

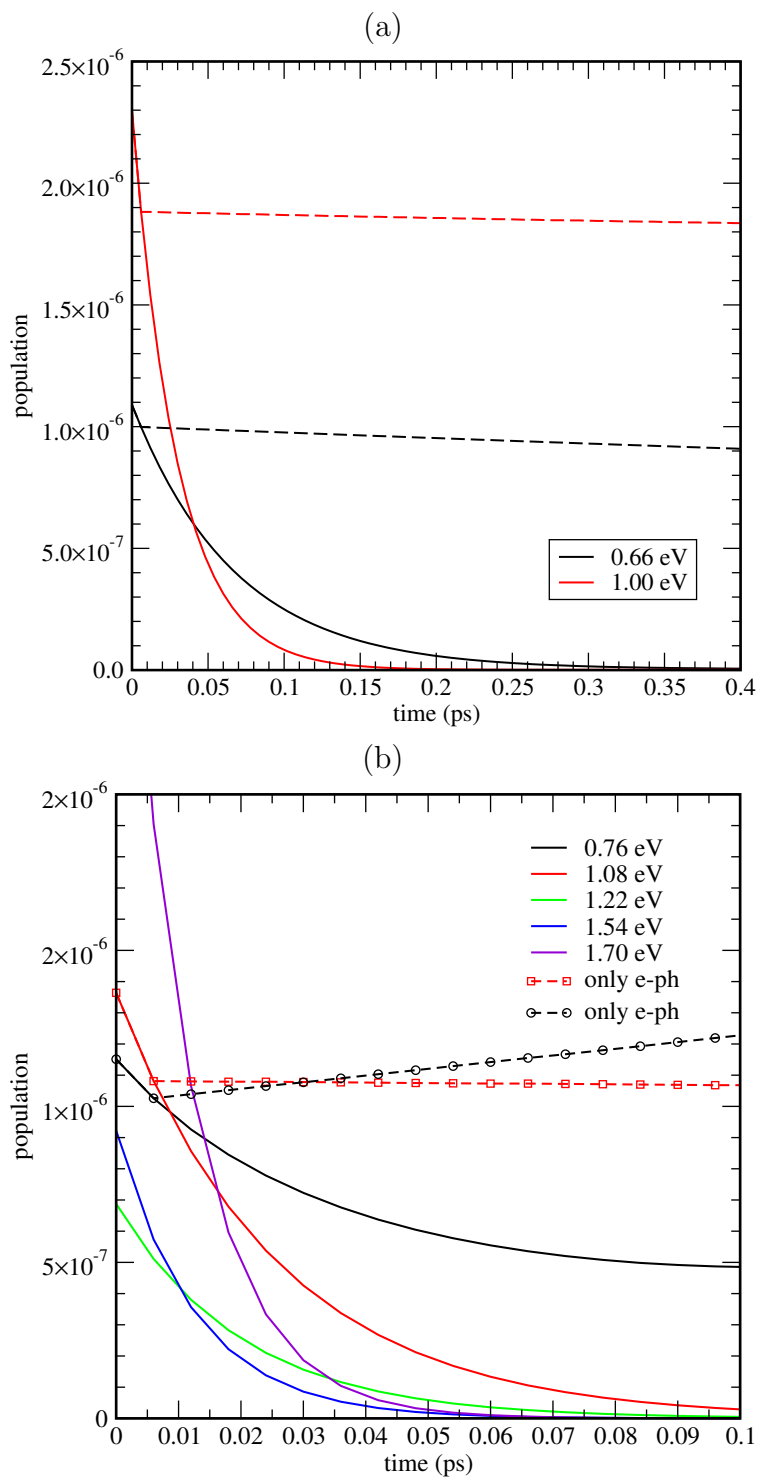
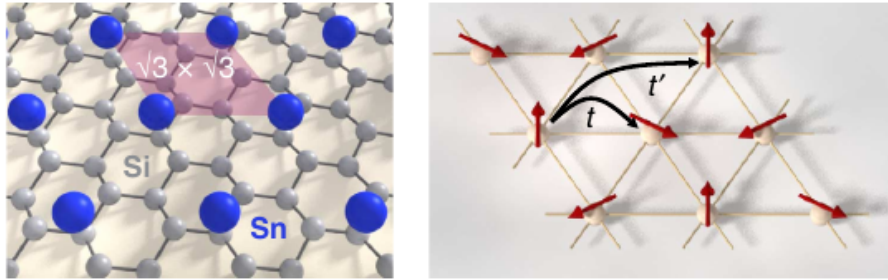


Figure 5.31: (a) and (b) are shown the population of electronic state as time for 4ML and 5ML of Pb:Si(111).

6 Strongly correlated system



6.1 Introduction

Ordered atomic layers on an insulating surface are often considered as prototypical systems for the study of electronic correlation. For instance, atoms of group-IV form ordered structures on the Si(111) surface at low coverage. The rather large distance between neighboring atoms in the structure (several Angstrom) results in a narrow electronic band inside the principal band gap of silicon formed by dangling bond orbitals of the adatoms. In the last decade the magnetic and electronic properties of narrow band electrons have attracted much interest of physicists. The behavior of half-filled systems including as many electrons as atomic sites is worth a special interest, because such systems may undergo both metal-insulator transitions and antiferromagnetic phase transitions which have been reported not only on some transition metal oxides, but also from electron counting arguments, one would expect this band to be half-filled in case of group-IV adatoms such as Si, Ge or Sn. One question arises: Is it true that the ground state of a half-filled system such as Sn:Si(111) will be antiferromagnetic? For answering this question, there are two complimentary (as we will show below) ways of stabilizing the system that result in a gapped electronic structure: On one hand side, the adatoms may undergo a Jahn-Teller like distortion leading to a superstructure with inequivalent dangling bond orbitals, or in the strongly correlated limit, electrons localize and form localized spins at every lattice site and this localized spins couple with each other by way of virtual hoppings and can be effectively described with a Heisenberg Hamiltonian with antiferromagnetic exchange interactions. On the other hand, Mott-Hubbard physics opens a gap between the filled and the unoccupied part of the electronic structure. Recently, not only the ground state of such systems, but also their dynamics on ultra-short time scales has come into focus of experimental investigations [46, 74]. Therefore, understanding the elementary excitations and their interplay, which determines the lifetime of excited states, has become an issue of current interest. This also includes the phonon excitations of the lattice and their coupling to the electrons. Therefore calculations of the phonon band structure and the electron-phonon coupling will be in the focus of this chapter.

6.2 Models using many-body Hamiltonians

6.2.1 Hubbard model

Independently in 1963 the Hubbard model was introduced by J. Hubbard, J. Kanamori and M.C. Gutzwiller [43, 53, 54, 58]. Originally for describing the ferromagnetism and answering the question : why the system shows insulating behavior with odd number of electrons this model was invented. Some scientists tried to answer this question with the help of band theory, but they failed because from this theory one would expect that such a system with a partly filled conduction band behaves like a metal. For finding the correct solution one had to consider the correlation terms between electrons. The Hubbard model can be written as

$$\begin{aligned}
 H &= H_t + H_U \\
 H_t &= t \sum_{\langle i,j \rangle} (\hat{c}_{i\sigma}^\dagger \hat{c}_{j\sigma} + h.c.) \\
 H_U &= U \sum_i (\hat{n}_{i\uparrow} - 1/2)(\hat{n}_{i\downarrow} - 1/2)
 \end{aligned} \tag{6.1}$$

H_t is the kinetic energy part of the Hubbard Hamiltonian which is describing the electron with the spin σ hopping from one lattice site, i , to another one j and the number of electrons at side i can be described as $\hat{n}_{i\sigma} = \hat{c}_{i\sigma}^\dagger \hat{c}_{i\sigma}$. and $n_i = n_{i\uparrow} + n_{i\downarrow}$. This hopping process can only take place, when site i and site j are nearest neighbors, can only take place. t is the hopping element and related to band width, w , with this formula such as : $w = 2zt$, where z related to coordination number of the considered lattice. For example for one dimension z is 2 and for a two-dimensional square lattice $z = 4$. Often the energies of calculation are given in units of the bandwidth. The repulsion between electrons on the same site can be described as H_U , where U is the energy cost for putting two electrons with opposite spin on one site.

6.2.2 $t - J$ model

Four possible configurations at one site can be mentioned in the Hubbard model : (a) The site may be singly occupied by one electron with spin up or (b) spin down, (c) doubly occupied by two electrons with opposite spin or (d) empty. For describing the interactions between spins on neighboring sites we have an effective model which called is the $t - J$ model and based on the Heisenberg model. Processes in the $t - J$ model to change the number of double occupancies are eliminated but it still contains the spin degrees of freedom of the electrons and the motion and interaction of double occupancies and holes, but it does not contains correlations between two spins with a displacement larger than two and real four spin interaction terms. By considering strong coupling limit for the Hubbard model ($U \gg t$) in the *half-filled* system, which means one electron per site ($\langle n \rangle = 1$), the effective model reduces to the Heisenberg model. In this model the exchange coupling constants given by

$$J = \frac{-4t^2}{U} \tag{6.2}$$

6.3 Investigation of half-filled system Sn:Si(111)

For the system Si(111):Sn($\sqrt{3} \times \sqrt{3}$), the prevailing experimental and theoretical view asserts that Mott-Hubbard physics is responsible for the formation of a gap in the electronic spectrum [45, 71, 85]. This is in contrast to the related system Ge(111):Sn($\sqrt{3} \times \sqrt{3}$) where both experiments and first-principles calculations point to a Jahn-Teller-like mechanism that stabilizes the system in a (3×3) superstructure with Sn adatoms at different adsorption heights. While the Jahn-Teller instability makes itself noticeable in the softening of a corresponding phonon mode, the effect of strong electronic correlations on the phonon spectrum has received little attention so far. I will show from my calculation that electronic correlations in Si(111):Sn ($\sqrt{3} \times \sqrt{3}$) favor a planar geometry and lead to a stiffening of the associated phonon mode.

From theory side of view, structures, the Sn:Ge(111) and Sn:Si(111) systems are studied by Pérez et. al. [90]. They considered two $\sqrt{3} \times \sqrt{3}$ and 3×3 structure and the possibility of transition due to surface phonon mode. From their calculation for the Sn:Ge(111) by mean Jahn-Teller-like distortion, they found the transition from $\sqrt{3} \times \sqrt{3}$ to 3×3 structure which is related to the electronic energy gain associated with the surface band splitting by Jahn-Teller-like mechanism. They showed that in 3×3 phases, from three Sn atoms in the unit cell by moving one Sn atom upward, three Ge atoms follow this motion and are moving toward that. This question was raised for us : is this mechanism possible for Sn on Si(111) surface or not?

For answering this question I start by means of DFT calculation to open the gap of this half-filled band system from the 3×3 structure and move one Sn atom up and two Sn atoms downward (one Sn atom upward and two other one in equivalent position). Then I allowed the system to be relaxed but after relaxation I found the system with three Sn atoms in the same height. This calculation show me that the Jahn-Teller distortion does not open the gap for the Sn:Si(111) system and after relaxation I found again $\sqrt{3} \times \sqrt{3}$ stable structure.

Combining experimental and theoretical investigations on 2D surface such as Sn on Si(111) for searching for the Mott-insulating state have pursued by Profeta and Tosatti [91]. They reported the magnetic Mott-Hubbard ground state by using the local spin density (LSDA) and on-site Coulomb repulsion, U , within a single-band Hubbard model. They observed the band splitting in the 4d core levels of Sn atoms in the Sn:Si(111) system. We tried to repeat their work by using the LDA + U method. Beginning with an undistorted geometry which is $\sqrt{3} \times \sqrt{3}$ unit cell (one Sn atom per unit), as it is shown in Fig.6.1, and then increasing the U value from zero to 4eV on the two electrons in $5p_z$ orbital of Sn atom. In Contrast with Ref. [91] result, by increasing the U value the system always is metallic while Ref. [91] showed the insulating gap reaches 0.3eV with $U \approx 4\text{eV}$.

A detailed understanding of the electronic structure of correlated systems requires special methods, as applied for instance in Ref. [71]. However, these methods, as well as the calculation of phonon spectra, rely on input from density functional theory (DFT). If applied with care, DFT calculations can already reveal salient features and allow us to address the various energy scales in the problem. While local or semi-local density functionals find the Si(111):Sn($\sqrt{3} \times \sqrt{3}$) to be metallic, the HSE hybrid functional [26, 48, 49] correctly reproduces the insulating ground state [68]. Technically speaking, electronic correlations are treated in the HSE functional as part of the (screened) electronic exchange. Therefore,

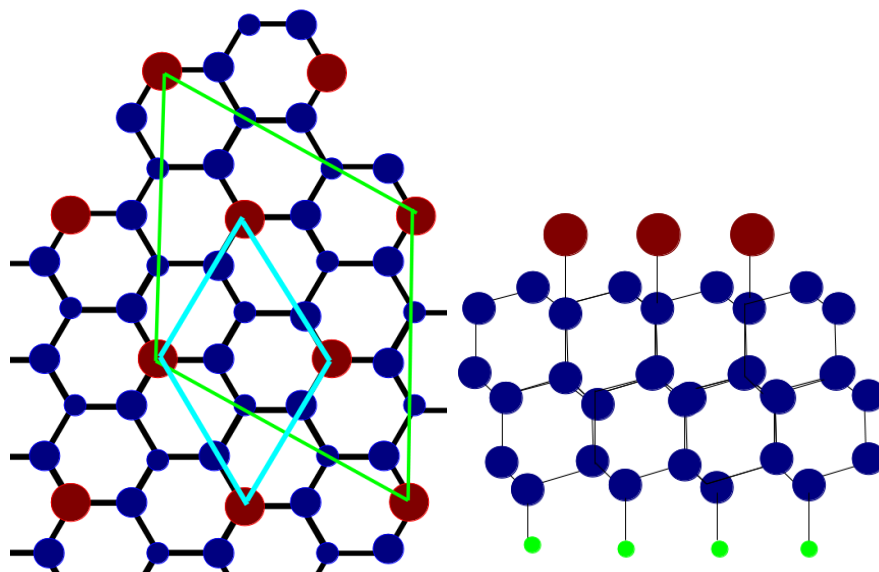


Figure 6.1: left: Top view of 3×3 (green unit cell) and $\sqrt{3} \times \sqrt{3}$ (turquoise unit cell). Sn atoms are red and Si atoms are blue. In the right panel is the side view of the slab geometry for the Sn:Si(111) surface.

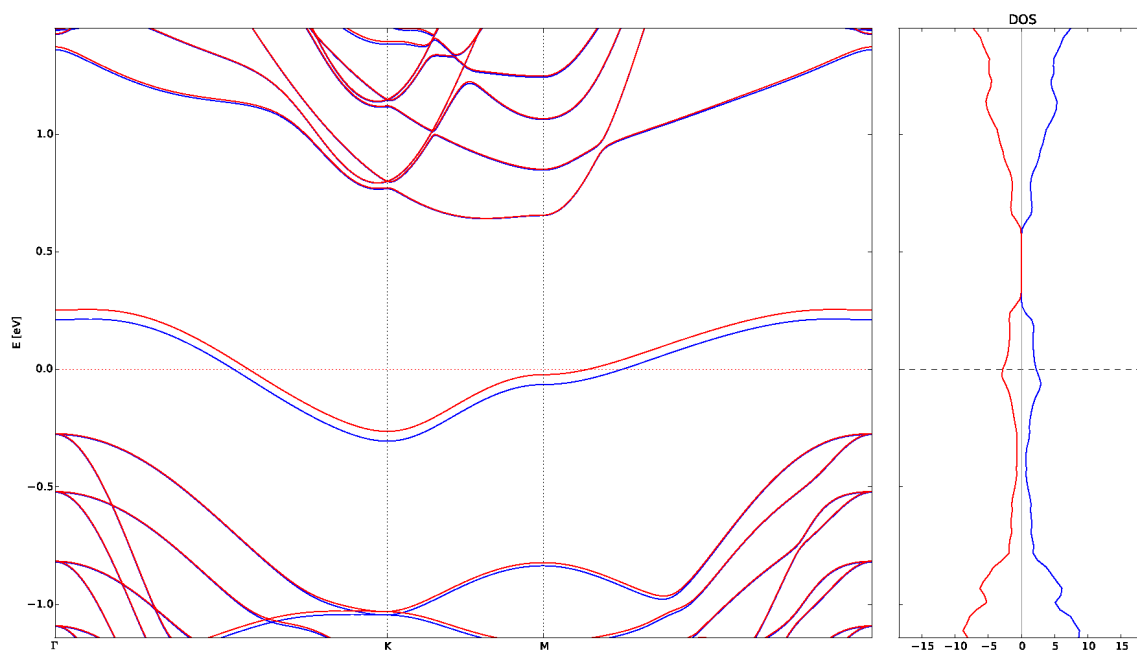


Figure 6.2: Band structure of $\sqrt{3} \times \sqrt{3}$ unit cell with spin-orbit coupling (red and blue color). As it is clear this system is half-filled band with LDA + U.

HSE calculations are unable to yield the proper electronic excitation spectrum, but they can be used to estimate the basic parameters (on-site Coulomb repulsion, exchange coupling parameters) that enter into model Hamiltonians employed to describe the dynamics of excitations[69].

6.4 Summary of previous experimental results

Experiments using scanning tunneling spectroscopy (STS) indicate that the Si(111):Sn($\sqrt{3} \times \sqrt{3}$) system undergoes a metal-to-insulator transition below ~ 30 K. Below this temperature, the pseudo-gap near the Fermi energy develops into a sharp gap [79] whose width is reported to be 35 meV according to recent measurements [85]. Below and above the Fermi energy E_F , experiments using angle-resolved photoemission (ARPES) [79] or inverse photoemission (KIRPES) [22] show pronounced quasiparticle peaks below and above E_F , respectively. These peaks have an estimated separation on the energy scale of roughly 200 meV (see also the discussion in Ref. [71]). According to recent studies, the most likely candidate for the spin ordering on the Si(111):Sn($\sqrt{3} \times \sqrt{3}$) surface is a row-wise antiferromagnetic structure [68, 71] in a ($2\sqrt{3} \times \sqrt{3}$) supercell.

6.5 Results

6.5.1 Electronic structure of AFM order

For calculating the electronic band structure, density functional theory calculations were performed by using the FHI-AIMS [93] code, which is an accurate all-electron full-potential electronic structure package based on numeric atom-centered orbitals, with "tight" computational settings. Both Perdew, Burke, and Ernzerhof (PBE) [88] formulation of the generalized gradient approximation (GGA) function and the screened hybrid functional, HSE with the mixing factor $\alpha = 0.25$ and screening parameter $\omega = 0.11$ bohr $^{-1}$ were used for exchange-correlation energy. The HSE functional addresses the effect of the short and long range potential by applying the screened Coulomb potential to the exchange interaction in order to screen the long range part of the Hartree-Fock exchange (see chapter 2).

$$E_{xc}^{\text{HSE}}(\omega) = aE_x^{\text{exact,SR}}(\omega) + (1 - a)E_x^{\text{PBE,SR}}(\omega) + E_x^{\text{PBE,LR}}(\omega) + E_c^{\text{PBE}} \quad (6.3)$$

In order to sample the Brillouin zone of the $\sqrt{3} \times \sqrt{3}$ and $2\sqrt{3} \times \sqrt{3}$ unit cells, we used a $8 \times 8 \times 1$ and $4 \times 8 \times 1$ Monkhorst-Pack[80] k-point mesh, respectively. The Si dangling bonds on the rear side of the slab were saturated by hydrogen atoms while one Sn atom in $\sqrt{3} \times \sqrt{3}$ and two tin atoms in $2\sqrt{3} \times \sqrt{3}$ were placed on the front surface. The position of Sn atoms, as well as of the Si atoms in the first eight layers, were relaxed, while the two layers of Si atoms at the side of hydrogen, are fixed together with the hydrogen atoms. The residual force components were less than 0.01 eV/Å.

Calculation of phonons and electron-phonon coupling of this system are interesting for us, so the Phonopy [118] package in conjunction with the VASP[63, 65] code was used for calculating the phonon band dispersion. Finite atomic displacements were used for a large supercell, which requires doubling size in both lateral directions, to obtain atomic forces for 48 displaced configurations. The Si lattice constant $a_0 = 5.445$ (5.468) Å for the HSE (PBE)

calculation was used, and the supercell was built with the 10 Å of vacuum in between the slabs.

Density functional theory (DFT) has been used for analysis the surface of Sn/Si(111) in 3×3 , $\sqrt{3} \times \sqrt{3}$ and $2\sqrt{3} \times \sqrt{3}$ in NM (nonmagnet), FM (ferromagnet) and AFM (antiferromagnet) orders. For 3×3 we consider the same situation as Ge/Si(111) that the three Sn atoms are not equivalent; one Sn atom is considered up (higher) than the other two Sn atoms, with forcing one Sn atom perpendicular to the surface. After relaxation all three Sn atoms come back in the same equivalent height and show us that the most favorable structure is $\sqrt{3} \times \sqrt{3}$ for this system, in the line with [90, 104]. Our calculation, unlike the semilocal calculation with the PBE functional, predict that the insulating antiferromagnetic structure is the ground state. Our result in line with [68, 71] studies, in which it is demonstrated that the insulating phase can be characterized as a Slater-type insulator via band magnetism due to strong hybridization of the dangling-bond (DB) electrons of Sn, between $5p_z$ Sn and $3p_z$ Si. In our result the AFM is more stable than the FM and NM structure by 49 and 63 meV. After applying the HSE both with spin-orbit coupling (SOC) and without SOC for the AFM system we got the band gap ≈ 530 meV and ≈ 348 meV. This value is in the line with the theoretical work [68] with the gap ≈ 328 meV but is much larger than the experimental value obtained from STS [79] which is ~ 40 meV, but closer to the value obtained from ARPES [71] with the gap ~ 200 meV.

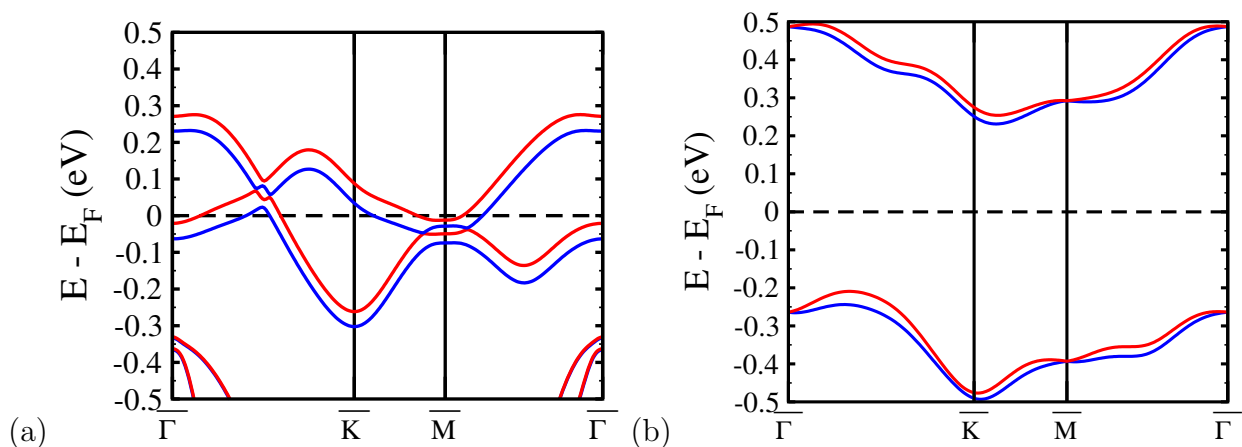


Figure 6.3: The electronic band structure of AFM order (a) with the PBE functional and (b) with the HSE06 functional. Two Sn atom per unit cell. The red and blue are related to the two spin channels.

6.5.2 Phonon band structure and electron-phonon coupling

We confirm previous calculations showing that a non-spin-polarized PBE calculation of the Si(111):Sn($\sqrt{3} \times \sqrt{3}$) leads to a metallic surface band. For the PBE ground state, phonon spectra were computed with the finite-displacement method and are presented in Fig (6.4). The phonon modes related to Sn appear in two groups: There is a mode in which both the Sn atom and the top-most layer of Si atoms move in phase (4 THz). Lower-lying modes involve out-of-phase motions of the Sn atom and the neighboring Si atoms. These comprise

Table 6.1: The total energy (in meV per unit cell $\sqrt{3} \times \sqrt{3}$) calculated for the AFM, FM and NM structures using the HSE and PBE functionals. The AFM with the HSE functional is the most stable structure.

	AFM	FM	NM
PBE	-407451952.07	-407451941.70	-407451940.51
HSE	-407483668.94	-407483619.12	—

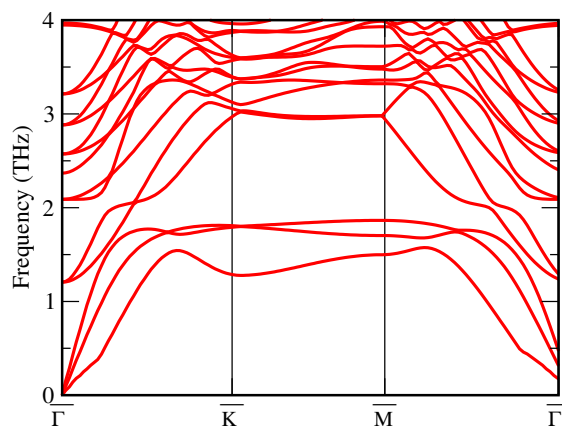


Figure 6.4: Phonon dispersion for $\sqrt{3} \times \sqrt{3}$ Sn:Si(111) obtained with the PBE functional in the non-magnetic state.

motions of the Sn atom in the surface plane, leading to bands with small dispersion (1.75 THz in NM calculation) and a dispersive band corresponding to a vertical motion of the Sn atom relative to the Si atoms (1.3 THz in NM calculation). The latter mode shows a slight softening at the edge of the Brillouin zone (point K). In agreement with previous studies [90], we interpret this observation as a first indication of a possible instability of the (metallic) PBE band structure with respect to Jahn-Teller distortions. However, this finding is not confirmed by the hybrid functional calculations.

Next, I repeated the calculations of phonon frequencies, now taking the AFM order of the spins into account. The $2\sqrt{3} \times \sqrt{3}$ unit cell with 2 Sn atoms is used for these calculations, but I restrict myself to phonons with crystal momentum $q = 0$ (Γ -point phonons). It is found that for the calculations with the hybrid functional HSE, a larger ($2\sqrt{3} \times \sqrt{3}$) unit cell with two Sn atoms was used. The ground state is found to be a spin-polarized state in which the magnetic moments at the two Sn atoms are pointing in opposite direction, i.e they show row-wise antiferromagnetic (AFM) ordering. The electronic structure shows a band gap. The width of the occupied (unoccupied) band along $\bar{\Gamma}\bar{M}$ is $w = 140$ meV ($w = 200$ meV); i.e. smaller than in the PBE ground state. The ferromagnetic solution is 25 meV per Sn atom higher than the AFM ground state. Calculations including the spin-orbit interaction show a splitting of the occupied surface band being largest at the K point (22 meV).

In order to investigate to which extent the AFM spin ordering can already account for the correlated electronic features, we performed PBE calculations with the ($2\sqrt{3} \times \sqrt{3}$) unit

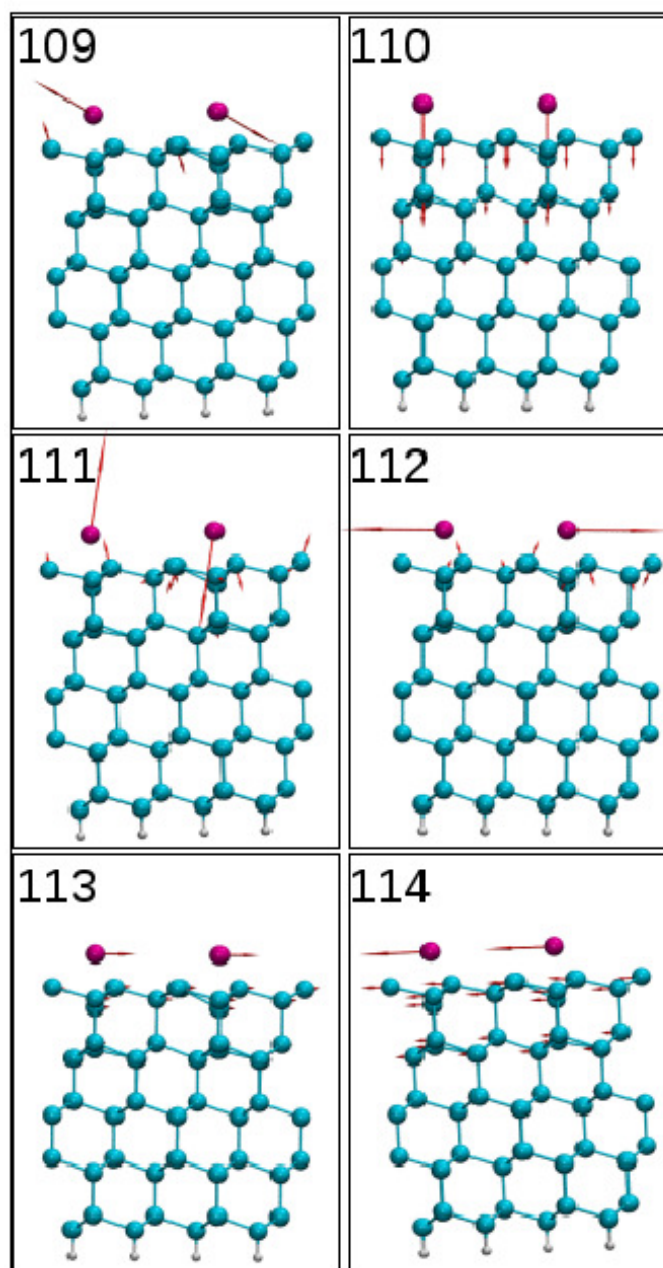


Figure 6.5: Side view of Sn (pink spheres) on Si(111) (blue spheres). Atomic displacements for selected phonon modes with $q = 0$ of Sn/Si(111) ($2\sqrt{3} \times \sqrt{3}$) are indicated by the arrows. Calculations are performed with PBE for the AFM state.

cell where the magnetic moments were 'frozen' in the AFM state. In these calculations, the occupied and the unoccupied surface states still overlap in energy, yielding a metallic surface. However, the band width of 275 meV of the unoccupied band along $\bar{\Gamma}\bar{M}$ is reduced relative to the non-spin-polarized PBE calculation.

For the low-lying phonon mode in which both Sn atoms move with opposite phase, shown as mode 111 in Fig. 6.5, we performed total-energy calculations with finite displacements

of both the Sn and Si atoms along the mode eigenvectors. The results for displacements of varying magnitude are shown in Fig (6.6). By fitting the data the phonon energy $\hbar\omega = 11$ meV is obtained. A considerable stiffening of this phonon mode is observed both in the HSE and spin-polarized PBE calculations in the AFM state. Thus, the geometrical structure in the AFM state is no longer prone to Jahn-Teller instability. Stabilization by spin-ordering and displacive rearrangements of the atoms must be considered as competing stabilization mechanisms excluding each other. For future studies of electronic dynamics, it is helpful to cast the electronic structure problem in the form of an effective Mott-Hubbard (MH) Hamiltonian. The hopping matrix element t can be estimated from the band width of the DFT calculations, yielding $t = w/8 = 25$ meV. This is in good agreement with previous estimates of the hopping matrix element [71]. We stress that the on-site repulsion U does not allow for a simple interpretation as repulsion between two electrons in the Sn p_z orbital. Both our HSE calculations and previous work [68] shows that the electrons occupying the lower surface band are still localized, but extend over both the Sn and its Si neighbors. With this caveat, the MH Hamiltonian can be used to study the excitation spectrum. Low-lying excitations are given by AFM spin waves. At half filling system every site is already occupied by one electron, and the MH Hamiltonian can be approximately transformed onto a antiferromagnetic Heisenberg model:

$$H = -J \sum_{\langle ij \rangle} \vec{S}_i \cdot \vec{S}_j$$

with the exchange coupling constants given by $J = -4t^2/U$. The energy differences between the FM and AFM state is given by $6J - (-2J) = 8J$. The presence of spin-orbit interaction requires the generalization to an anisotropic Heisenberg model. In such a 2D anisotropy model, the excitation of spin waves requires a minimum energy. The charged excitations are given by the addition or removal of one electron. In the hybrid functional approach, the band gap can be taken as a first approximation of the typical energy of such an excitation. In the MH Hamiltonian, the lower and upper Hubbard band can be approximated by

$$\varepsilon_{\pm}(k) = \frac{1}{2} \left(\varepsilon(k) + U \pm \sqrt{\varepsilon^2(k) + U^2} \right)$$

Thus, the energy of a charged excitation is of the order of U . in a first estimate, we can identify U with the gap between the two surface bands in the HSE calculation. From Fig. 6.3, this yields $U \approx 0.75$ eV. On the other hand, the total energy difference between the FM and the AFM (Table 6.1) can be used to obtain an estimate for $J = 3.1$ meV, and hence, within the large- U limit of the Hubbard model, also for U . Combining the data from the band structure and from $E_{\text{AFM}} - E_{\text{FM}} = 8J$, we conclude that $U \approx 0.75$ eV is indeed a reasonable estimate.

6.5.3 Relaxation of electronic excitation

Optical excitation of the surface will generate electron-hole pairs. If we disregard the Coulomb interaction between electron and hole, assuming that it is screened, the energy scale is the same as the energy for charged excitations, i.e. of the order of a few tenth of eV. In principle, these excitation can decay by dissipating their energy to spin waves or to phonons. The relative importance of these processes depends on the spin structure of the

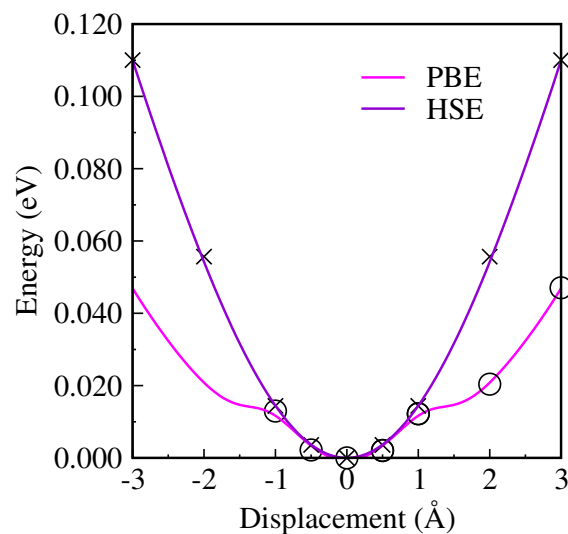


Figure 6.6: Energy as function of displacement along mode 111 at $q = 0$ for $(2\sqrt{3} \times \sqrt{3})$ with the AFM ordering of the electron spins taken into account.

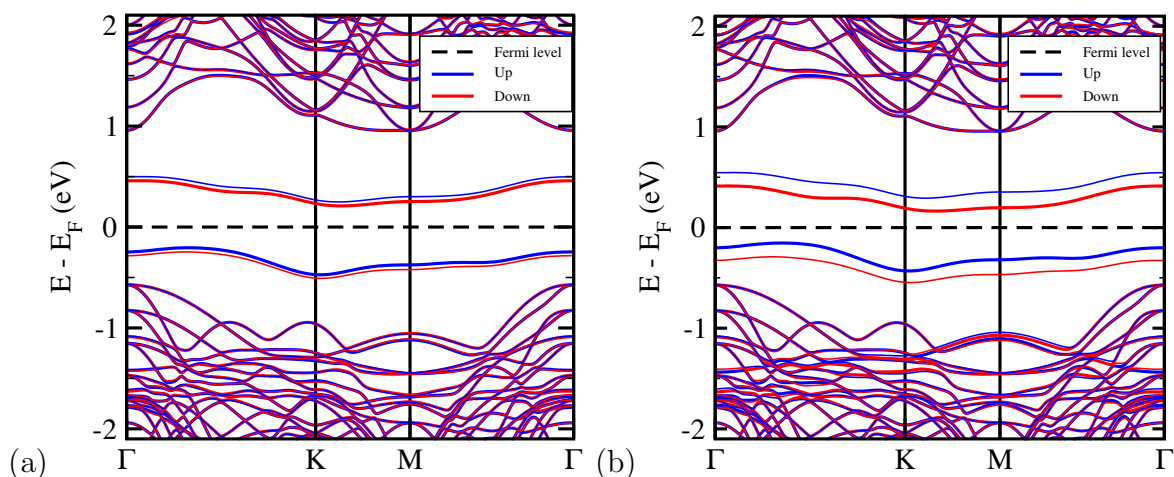


Figure 6.7: Electronic band structure of $\text{Sn}:(2\sqrt{3} \times \sqrt{3})\text{Si}(111)$ calculated with the HSE functional for displaced structures. The displacements are taken from (a) Fig. 6.5 mode 109 and (b) Fig. 6.5 mode 111. By comparing the band positions to the undistorted structure, Fig. 6.3 (b), the electron-phonon coupling parameter can be extracted.

excited many-particle states and has been discussed previously [70]. Since the excitation energy is sizable, several magnons or phonons need to be generated simultaneously in a highly non-linear process. If decay into phonons is the dominating process, the electron-phonon coupling, expressed by the deformation potential, is the decisive parameter. From our HSE calculations with frozen phonons, we are in position to obtain the deformation potential from the shift of the surface bands associated with the atomic displacements. Lenarčič and co-workers [69] have presented a MH model coupled to a phononic Hamiltonian that allows

them to estimate the lifetime of the exciton due to decay into phonons by a Zener-type expression. The decisive parameters are the order of the process, given by $n = U/(\hbar\omega_{ph})$, and the electron-phonon coupling parameter. From our calculations, we can give a rough estimate for the phonon-related exciton lifetime. Typical values for the parameters are e.g. $n = U/(\hbar\omega_{ph}) = 68$.

$$\begin{aligned}\Gamma &= \sqrt{2\pi} \frac{4t^2}{\omega} \left(\frac{1}{2} - \frac{2t^2}{V^2} \right) \cdot \frac{1}{\sqrt{n}} \exp(-n(\ln \frac{n}{2\xi} - 1)) \cdot (1 - \frac{1}{2^n}) \\ &= \Gamma_0 \frac{1}{\sqrt{n}} \exp(-n(\ln \frac{n}{2\xi} - 1))\end{aligned}\tag{6.4}$$

Where the $\xi = (\frac{\lambda}{\hbar\omega})$ and λ is the electron-phonon coupling constant. For calculating the λ I use the same method as in chapter 5 for Pb : Si(111). In this calculation I just consider two modes which are related to Sn atoms where they are moving in the opposite direction. As I show in the Fig. (6.5) these two modes are mode number 111 (where two Sn atoms are moving in opposite out of plane direction) and mode number 109 (where two Sn atoms are moving in opposite in-plane direction). In the Fig.(6.7) (a) and Fig. (6.7) (b), I show the electron-phonon coupling for mode number 109 and 111, respectively. From my calculation, I assume that the electron-phonon coupling for $2\sqrt{3} \times \sqrt{3}$ is average of mode 111 and mode 109 and find that λ is equal to 0.05 eV. Then the $\frac{1}{\sqrt{n}} \exp(-n(\ln \frac{n}{2\xi} - 1)) \approx 1.5 \times 10^{-7}$ and $\frac{1}{\Gamma_0} = 10\text{fs}$. By using the Eq. (6.4) and using the numbers that I got for n and λ , we obtain a lifetime, $\frac{1}{\Gamma}$, as large as $100ns$.

7 Conclusion

In Chapter 4, the vibrational properties of the SIC phase of Pb on Si(111) ($\sqrt{3} \times \sqrt{3}$) have been determined. Raman spectroscopy is used to detect surface vibrational Pb/Si interface modes representing unique experimental fingerprints of the atomic structure and chemical bonding. An overall assignment to microscopic surface modes has been achieved by comparison to respective first-principles calculations of the H3 and T4 adsorption geometries. The high similarity of surface phonons obtained in calculations for T4 and H3 atomic structures confirms a comparably high degree of decoupling of the Pb film in respect to the Si substrate. Pb-Pb interactions seem to play a more important role than Pb-Si bonds for structure formation of the Pb layer. From our Raman calculation we can not find any difference between T4 and H3 structures. By comparing our result with the experimental result we conclude that the $\sqrt{3} \times \sqrt{3}$ has enough accuracy for the H3 and T4 pattern to continue with this pattern for the next Chapter.

In Chapter 5, the electronic as well as phononic band structures and electron-phonon coupling strength have been calculated for Pb/Si(111) films using a Si(111)($\sqrt{3} \times \sqrt{3}$) structural model. The energetic positions of the quantum well (QW) states are found to be in much better agreement with photoemission spectroscopy [61, 100] than previous calculations. While simple (1×1) models of the Pb films predict an upward dispersion of the QW states near the Γ point, the QW states in the ($\sqrt{3} \times \sqrt{3}$) films show much less dispersion near Γ , in line with experiments. Moreover, the calculation of electronic wavefunctions puts us in position to assign the quantum-confined state closest to the band gap of silicon (this is an occupied state in films with an odd number of layers, and an unoccupied state in a film with an even number of layers) to a quantum well resonance (QWR). This means that a major part of the wavefunction extends into the Si substrate. This identification of the occupied QWR in the 5 ML Pb film not only solves the long-standing puzzle about the absent dispersion of this state [27] but also explains why its broadening due to coupling to phonons is much weaker than expected from previous theoretical models [73]. The phonon band structures calculated with inclusion of Si substrate layers display stiff optical modes pertinent to vibrations localized at the surface and subsurface layer of Pb. In contrast to free-standing films, the maximum Pb phonon frequency of 2.45 THz is found in the films with an even number of layers. This could be explained by inspection of the phonon eigenvectors. The computational results for the deformation potential of the quantum well states provide access to the role of electron-phonon coupling in the relaxation of photo-excited electrons in the Pb films. We find that the acoustic deformation potentials of the unoccupied states are negative and decrease in absolute magnitude with increasing energy of the electronic bands. Sizeable shear deformation potentials in the QW states are observed. The optical deformation potentials are strongly dependent on both the QW state and the phonon mode considered. The highest-lying optical phonon modes give rise to a splitting of degenerate QW states. Comparing the results for 4 ML and 5 ML Pb, we find that the optical deformation potentials are generally larger for the 4 ML film, in qualitative agreement with previous theoretical studies [128]. Thus our

results helped us for a detailed analysis of the relaxation dynamics of e-ph in Pb QW states. We found that the relaxation time for e-ph coupling is in the range of some picosecond while for the e-e scattering it is in the range of ten femtoseconds as we saw in Chapter 5.

In contrast to relaxation in metallic bands, we investigate the Sn:Si(111) surface with 1/3 ML coverage, and we found with help of hybrid functional (HSE06) that this surface is an insulating surface with Mott-Hubbard bands inside the substrate band gap. The deformation potential for e-ph coupling in the AFM structure was calculated in Chapter 6. From our calculations the Mott-Hubbard gap is found to be much larger than the typical phononic quanta; the relaxation of hot carriers into the ground state is possible only by a multi-phonon process. This gives rise to a very long lifetime of the excitations which I estimate in Chapter 6 from my calculation.

Bibliography

- [1] M. Amini. “First-Principles study of defects in transparent conducting oxide materials”. PhD thesis. Universiteit Antwerpen (Belgium), 2014.
- [2] A. Barfuss et al. “Elemental Topological Insulator with Tunable Fermi Level: Strained α -Sn on InSb(001)”. In: *Phys. Rev. Lett.* 111 (2013), p. 157205. DOI: 10.1103/PhysRevLett.111.157205.
- [3] S. Baroni, P. Giannozzi, and A. Testa. “Green’s-function approach to linear response in solids”. In: *Phys. Rev. Lett.* 58 (1987), pp. 1861–1864. DOI: 10.1103/PhysRevLett.58.1861.
- [4] S. Baroni et al. “Phonons and related crystal properties from density-functional perturbation theory”. In: *Rev. Mod. Phys.* 73 (2001), pp. 515–562. DOI: 10.1103/RevModPhys.73.515.
- [5] F. Bechstedt. *Many-Body Approach to Electronic Excitations*. Springer, Berlin, Heidelberg, 2015.
- [6] A. D. Becke. “Density functional calculations of molecular bond energies”. In: *The Journal of Chemical Physics* 84 (1986), p. 4524. DOI: 10.1063/1.450025.
- [7] A. D. Becke and M. R. Roussel. “Exchange holes in inhomogeneous systems: A coordinate-space model”. In: *Phys. Rev. A* 39 (1989), pp. 3761–3767. DOI: 10.1103/PhysRevA.39.3761.
- [8] A.D. Becke. “A new mixing of Hartree-Fock and local density-functional theories”. In: *The Journal of Chemical Physics* 98 (1993), p. 1372. DOI: 10.1063/1.464304.
- [9] G. Bihlmayer. “Topological Matter-Topological Insulators, Skyrmions and Majoranas, ”Band structure from first-principles and relativistic effects””. In: *Forschungszentrum Jülich* (2015).
- [10] P. E. Blöchl. “Projector augmented-wave method”. In: *Phys. Rev. B.* 50 (1994), pp. 17953–17979. DOI: 10.1103/PhysRevB.50.17953.
- [11] J. Braun et al. “Surface phonon dispersion curves of thin Pb films on Cu(111)”. In: *Phys. Rev. B.* 79 (2009), p. 205423. DOI: 10.1103/PhysRevB.79.205423.
- [12] B. N. Brockhouse et al. “Crystal Dynamics of Lead. I. Dispersion Curves at 100K”. In: *Phys. Rev.* 128 (1962), pp. 1099–1111. DOI: 10.1103/PhysRev.128.1099.
- [13] P. Bruesch. *Phonons: Theory and Experiments II*. Vol. 65. Springer, Berlin, Heidelberg, 1986.
- [14] C. Brun et al. “Reduction of the superconducting gap of ultrathin Pb islands grown on Si(111)”. In: *Phys. Rev. Lett.* 102 (2008), p. 207002.
- [15] C. Brun et al. “Remarkable effects of disorder on superconductivity of single atomic layers of lead on silicon”. In: *Nature Physics* 10 (2014), pp. 444–450.

- [16] N. Bücking et al. “Linking density functional and density-matrix theory: Picosecond electron relaxation at the Si(100) surface”. In: *Phys. Rev. B* 77 (2008), p. 233305. DOI: 10.1103/PhysRevB.77.233305.
- [17] Y.A. Bychkov and E.I. Rashba. “Oscillatory effects and the magnetic susceptibility of carriers in inversion layers”. In: *Journal of Physics C Solid State Physics* 17 (1984), pp. 6039–6045. DOI: 10.1088/0022-3719/17/33/015.
- [18] J. M. Carpinelli et al. “Direct observation of a surface charge density wave”. In: *Nature* 381 (1996), 398400. DOI: 10.1038/381398a0.
- [19] D. M. Ceperley and B. J. Alder. “Ground State of the Electron Gas by a Stochastic Method”. In: *Phys. Rev. Lett.* 45 (1980), pp. 566–569. DOI: 10.1103/PhysRevLett.45.566.
- [20] T.L. Chan et al. “First-principles studies of structures and stabilities of Pb/Si(111)”. In: *Phys. Rev. B.* 68 (2003), p. 045410. DOI: 10.1103/PhysRevB.68.045410.
- [21] L. Chaput et al. “Phonon-phonon interactions in transition metals”. In: *Phys. Rev. B* 84 (2011), p. 094302. DOI: 10.1103/PhysRevB.84.094302.
- [22] A. Charrier et al. “Contrasted electronic properties of Sn-adatom-based ($\sqrt{3}\times\sqrt{3}$)R30° reconstructions on Si(111)”. In: *Phys. Rev. B* 64 (2001), p. 115407. DOI: 10.1103/PhysRevB.64.115407.
- [23] E. V. Chulkov et al. “Electronic Excitations in Metals and at Metal Surfaces”. In: *Chemical Reviews* 106.10 (2006), pp. 4160–4206. DOI: 10.1021/cr050166o.
- [24] S. J. Clark and J. Robertson. “Screened exchange density functional applied to solids”. In: *Phys. Rev. B* 82 (2010), p. 085208. DOI: 10.1103/PhysRevB.82.085208.
- [25] Morrel H. Cohen. “Theory of Superconductivity. J. R. Schrieffer. Benjamin, New York, 1964. xiv + 282 pp. Illus. 10”. In: *Science* 148.3675 (1965), pp. 1318–1318. ISSN: 0036-8075. DOI: 10.1126/science.148.3675.1318.
- [26] P. Deák et al. “Accurate defect levels obtained from the HSE06 range-separated hybrid functional”. In: *Phys. Rev. B* 81 (2010), p. 153203. DOI: 10.1103/PhysRevB.81.153203.
- [27] J.H. Dil et al. “Electron Localization in metallic quantum wells: Pb versus In on Si(111)”. In: *Phys. Rev. B.* 73 (2006), 161308(R).
- [28] J.H. Dil et al. “Rashba-Type Spin-Orbit Splitting of Quantum Well States in Ultrathin Pb Films”. In: *Phys. Rev. Lett.* 101 (2008), p. 266802. DOI: 10.1103/PhysRevLett.101.266802.
- [29] P. A. M. Dirac. “Note on Exchange Phenomena in the Thomas Atom”. In: *Mathematical Proceedings of the Cambridge Philosophical Society* 26.3 (1930), pp. 376–385. DOI: 10.1017/S0305004100016108.
- [30] J. P. Dombroski, S. W. Taylor, and P. M. W. Gill. “KWIK: Coulomb Energies in O(N) Work”. In: *The Journal of Physical Chemistry* 100.15 (1996), pp. 6272–6276. DOI: 10.1021/jp952841b.
- [31] G. Dresselhaus. “Spin-Orbit Coupling Effects in Zinc Blende Structures”. In: *Phys. Rev.* 100 (1955), pp. 580–586. DOI: 10.1103/PhysRev.100.580.

- [32] P.M. Echenique et al. “Decay of electronic excitations at metal surfaces”. In: *Surface Science Reports* 52.7 (2004), pp. 219–317. ISSN: 0167-5729. DOI: <https://doi.org/10.1016/j.surfrep.2004.02.002>.
- [33] D. Eom et al. “Persistent Superconductivity in Ultrathin Pb Films: A Scanning Tunneling Spectroscopy Study”. In: *Phys. Rev. Lett.* 96 (2006), p. 027005. DOI: 10.1103/PhysRevLett.96.027005.
- [34] N. Esser. “Analysis of semiconductor surface phonons by Raman spectroscopy”. In: *Applied Physics A* 69 (1999), pp. 507–518. DOI: 10.1007/s003390051455.
- [35] K. Fleischer et al. “Phonon and polarized reflectance spectra from Si(111) – (4 × 1)In : Evidence for a charge-density-wave driven phase transition”. In: *Phys. Rev. B.* 67 (2003), p. 235318. DOI: 10.1103/PhysRevB.67.235318.
- [36] K. Fleischer et al. “Surface phonons of the Si(111) : In – (4 × 1) and (8 × 2) phases”. In: *Phys. Rev. B.* 76 (2007), p. 205406. DOI: 10.1103/PhysRevB.76.205406.
- [37] E. Ganz et al. “Growth and morphology of Pb on Si(111)”. In: *Surface Science* 257 (1991), pp. 259–273. DOI: [https://doi.org/10.1016/0039-6028\(91\)90797-V](https://doi.org/10.1016/0039-6028(91)90797-V).
- [38] A. K. Geim and K. S. Novoselov. “The rise of graphene”. In: *Nature Materials* 6 (2007), pp. 183–191. DOI: 10.1038/nmat1849.
- [39] P. Giannozzi et al. “Ab initio calculation of phonon dispersions in semiconductors”. In: *Phys. Rev. B* 43 (1991), pp. 7231–7242. DOI: 10.1103/PhysRevB.43.7231.
- [40] M. Glukhovtsev. “Recent Developments and Applications of Modern Density Functional Theory. Theoretical and Computational Chemistry”. In: *Journal of Chemical Information and Computer Sciences* 37.6 (1997), pp. 1206–1206. DOI: 10.1021/ci970402z.
- [41] X. Gonze, D.C. Allan, and M.P. Teter. “Dielectric tensor, effective charges, and phonons in α -quartz by variational density-functional perturbation theory”. In: *Phys. Rev. Lett.* 68 (1992), pp. 3603–3606. DOI: 10.1103/PhysRevLett.68.3603.
- [42] X. Gonze and C. Lee. “Dynamical matrices, Born effective charges, dielectric permittivity tensors, and interatomic force constants from density-functional perturbation theory”. In: *Phys. Rev. B* 55 (1997), pp. 10355–10368. DOI: 10.1103/PhysRevB.55.10355.
- [43] M. C. Gutzwiller. “Effect of Correlation on the Ferromagnetism of Transition Metals”. In: *Phys. Rev. Lett.* 10 (1963), pp. 159–162. DOI: 10.1103/PhysRevLett.10.159.
- [44] R.A. Halvorson and P.J. Vikesland. “Surface-Enhanced Raman Spectroscopy (SERS) for Environmental Analyses”. In: *Environmental Science and Technology* 44.20 (2010), pp. 7749–7755. DOI: 10.1021/es101228z.
- [45] P. Hansmann et al. “Long-Range Coulomb Interactions in Surface Systems: A First-Principles Description within Self-Consistently Combined GW and Dynamical Mean-Field Theory”. In: *Phys. Rev. Lett.* 110 (2013), p. 166401. DOI: 10.1103/PhysRevLett.110.166401.
- [46] P. Hansmann et al. “Uncertainty principle for experimental measurements: Fast versus slow probes”. In: *Sci. Rep.* 6 (2016), p. 19728. DOI: 10.1038/srep19728.

- [47] R. Heid et al. “Effect of spin-orbit coupling on the electron-phonon interaction of the superconductors Pb and Tl”. In: *Phys. Rev. B.* 81 (2010), p. 174527.
- [48] J. Heyd and G. E. Scuseria. “Efficient hybrid density functional calculations in solids: Assessment of the Heyd-Scuseria-Ernzerhof screened Coulomb hybrid functional”. In: *The Journal of Chemical Physics* 121 (2004), p. 1187. DOI: 10.1063/1.1760074.
- [49] J. Heyd, G. E. Scuseria, and M. Ernzerhof. “Hybrid functionals based on a screened Coulomb potential”. In: *Journal of Chemical Physics* 118 (2003), p. 8207. DOI: 10.1063/1.1564060.
- [50] P. Hohenberg and W. Kohn. “Inhomogeneous Electron Gas”. In: *Phys. Rev.* 136 (1964), B864–B871. DOI: 10.1103/PhysRev.136.B864.
- [51] I-Po Hong et al. “Decay mechanisms of excited electrons in quantum-well states of ultrathin Pb islands grown on Si(111): Scanning tunneling spectroscopy and theory”. In: *Phys. Rev. B.* 80 (2009), 081409(R).
- [52] G.Q. Huang. “Surface lattice vibration and electron-phonon interaction in Pb(111) ultrathin superconducting films from first principles: both with and without Si substrate”. In: *New Journal of Physics* 13.9 (2011), p. 093023.
- [53] J. Hubbard and B.H. Flowers. “Electron correlations in narrow energy bands”. In: *Proceedings of the Royal Society of London. Series A. Mathematical and Physical Sciences* 276 (1963).
- [54] J. Hubbard and B.H. Flowers. “Electron correlations in narrow energy bands III. An improved solution”. In: *Proceedings of the Royal Society of London. Series A. Mathematical and Physical Sciences* 281 (1964).
- [55] E. Igumbor, K. Obodo, and W. E. Meyer. *Ab Initio Study of MgSe Self-Interstitial (Mg_i and Se_i)*. Vol. 242. Solid State Phenomena. Trans Tech Publications, Feb. 2016, pp. 440–446. DOI: 10.4028/www.scientific.net/SSP.242.440.
- [56] H. Iikura et al. “A long-range correction scheme for generalized-gradient-approximation exchange functionals”. In: *Journal of Chemical Physics* 115 (2001), p. 3540. DOI: 10.1063/1.1383587.
- [57] M. Jalochocki and E. Bauer. “Reflection highenergy electron diffraction intensity oscillations during the growth of Pb on Si(111)”. In: *Journal of Applied Physics* 63 (1988), p. 4501. DOI: 10.1063/1.340145.
- [58] J. Kanamori. “Electron Correlation and Ferromagnetism of Transition Metals”. In: *Progress of Theoretical Physics* 30.3 (1963), pp. 275–289. DOI: 10.1143/PTP.30.275.
- [59] D. Karhánek, T. Bu, and J. Hafner. “A density-functional study of the adsorption of methane-thiol on the (111) surfaces of the Ni-group metals: II. Vibrational spectroscopy”. In: *Journal of Physics: Condensed Matter* 22.26 (2010), p. 265006.
- [60] P. S. Kirchmann and U. Bovensiepen. “Ultrafast electron dynamics in Pb/Si(111) investigated by two-photon photoemission”. In: *Phys. Rev. B.* 78 (2008), p. 035437.
- [61] P.S. Kirchmann et al. “Quasiparticle lifetimes in metallic quantum-well nanostructures”. In: *Nature Physics* 6 (2010), pp. 782–785. DOI: 10.1038/nphys1735.

- [62] W. Kohn and L. J. Sham. “Self-Consistent Equations Including Exchange and Correlation Effects”. In: *Phys. Rev.* 140 (1965), A1133–A1138. DOI: 10.1103/PhysRev.140.A1133.
- [63] G. Kresse and J. Furthmüller. “Efficient iterative schemes for ab initio total-energy calculations using a plane-wave basis set”. In: *Phys. Rev. B.* 54 (1996), pp. 11169–11186. DOI: 10.1103/PhysRevB.54.11169.
- [64] G. Kresse, J. Furthmüller, and J. Hafner. “Ab initio Force Constant Approach to Phonon Dispersion Relations of Diamond and Graphite”. In: *EPL* 32.9 (1995), p. 729.
- [65] G. Kresse and D. Joubert. “From ultrasoft pseudopotentials to the projector augmented-wave method”. In: *Phys. Rev. B* 59 (1999), pp. 1758–1775. DOI: 10.1103/PhysRevB.59.1758.
- [66] C. Kumpf et al. “Structural study of the commensurate-incommensurate low-temperature phase transition of Pb on Si(111)”. In: *Surface Science* 448.2 (2000), pp. L213–L219. DOI: [https://doi.org/10.1016/S0039-6028\(99\)01224-8](https://doi.org/10.1016/S0039-6028(99)01224-8).
- [67] K. Kunc and R.M. Martin. “Ab Initio Force Constants of GaAs: A New Approach to Calculation of Phonons and Dielectric Properties”. In: *Phys. Rev. Lett.* 48 (1982), pp. 406–409. DOI: 10.1103/PhysRevLett.48.406.
- [68] J.H. Lee et al. “Antiferromagnetic superexchange mediated by a resonant surface state in Sn/Si(111)”. In: *Phys. Rev. B.* 90 (2014), p. 125439. DOI: 10.1103/PhysRevB.90.125439.
- [69] Z. Lenarčič, M. Eckstein, and P. Prelovšek. “Exciton recombination in one-dimensional organic Mott insulators”. In: *Phys. Rev. B* 92 (2015), 201104(R). DOI: 10.1103/PhysRevB.92.201104.
- [70] Z. Lenarčič and P. Prelovšek. “Ultrafast charge recombination in a photoexcited Mott-Hubbard insulator”. In: *Phys. Rev. Lett.* 111 (2013), p. 016401. DOI: 10.1103/PhysRevLett.111.016401.
- [71] G. Li et al. “Magnetic order in a frustrated two-dimensional atom lattice at a semiconductor surface”. In: *Nature Communications* 4 (2013), p. 1620. DOI: 10.1038/ncomms2617.
- [72] M. Liebhaber et al. “Surface phonons of the Si(111)-(7 × 7) reconstruction observed by Raman spectroscopy”. In: *Phys. Rev. B.* 89 (2014), p. 045313. DOI: 10.1103/PhysRevB.89.045313.
- [73] M. Ligges et al. “Electron-phonon coupling in quantum-well states of the Pb/Si(111) system”. In: *J. Phys.: Condens. Matter* 26 (2014), p. 352001. DOI: 10.1088/0953-8984/26/35/352001.
- [74] M. Ligges et al. “Ultrafast Doublon Dynamics in Photoexcited 1T - TaS₂”. In: *Phys. Rev. Lett.* 120 (2018), p. 166401. DOI: 10.1103/PhysRevLett.120.166401.
- [75] A. Linscheid, A. Sanna, and E. K. U. Gross. “Ab-initio calculation of a Pb single layer on a Si substrate: two-dimensionality and superconductivity”. In: *arXiv:1503.00977* (2015). URL: [arXiv:1503:00977v1](https://arxiv.org/abs/1503.00977v1).

- [76] A. Manchon et al. “New perspectives for Rashba spinorbit coupling”. In: *Nature Materials* 14 (2015), p. 871.
- [77] A. Mans et al. “Quantum electronic stability and spectroscopy of ultrathin Pb films on Si(111) 7×7 ”. In: *Phys. Rev. B.* 66 (2002), p. 195410.
- [78] B. Mihailova. “Raman and IR spectroscopy in materials science. Symmetry analysis of normal phonon modes”. In: *International Union of Crystallography Commission on Mathematical and Theoretical Crystallography* (Lekeitio, Spain, 21-27 June 2009).
- [79] S. Modesti et al. “Insulating Ground State of Sn/Si(111) $-(\sqrt{3} \times \sqrt{3})R30^\circ$ ”. In: *Phys. Rev. Lett.* 98 (2007), p. 126401. DOI: 10.1103/PhysRevLett.98.126401.
- [80] H. J. Monkhorst and J. D. Pack. “Special points for Brillouin-zone integrations”. In: *Phys. Rev. B.* 13 (1976), pp. 5188–5192. DOI: 10.1103/PhysRevB.13.5188.
- [81] S. V. Morozov et al. “Giant Intrinsic Carrier Mobilities in Graphene and Its Bilayer”. In: *Phys. Rev. Lett.* 100 (2008), p. 016602. DOI: 10.1103/PhysRevLett.100.016602.
- [82] H. Nakano et al. *Recent advances in ab initio, density functional theory, and relativistic electronic structure theory*. In: *Theory and Applications of Computational Chemistry: The First Forty Years; Dykstra, C. E., Frenking, G., Kim, K. S., and Scuseria, G. E. (eds.)* Elsevier, Amsterdam, 2005, 507557.
- [83] J. Noffsinger and M.L. Cohen. “Superconductivity in monolayer Pb on Si(111) from first principles”. In: *Solid State Communications* 151 (2011), pp. 421–424. DOI: 10.1016/j.ssc.2011.01.006.
- [84] R. W. Nunes and X. Gonze. “Berry-phase treatment of the homogeneous electric field perturbation in insulators”. In: *Phys. Rev. B.* 63 (2001), p. 155107. DOI: 10.1103/PhysRevB.63.155107.
- [85] A. B. Odobescu et al. “Electronic correlation effects and Coulomb gap in the Si(111) $-(\sqrt{3} \times \sqrt{3})$ -Sn surface”. In: *Phys. Rev. B* 95 (2017), p. 195151. DOI: 10.1103/PhysRevB.95.195151.
- [86] K. Parlinski, Z. Q. Li, and Y. Kawazoe. “First-Principles Determination of the Soft Mode in Cubic ZrO₂”. In: *Phys. Rev. Lett.* 78 (1997), pp. 4063–4066. DOI: 10.1103/PhysRevLett.78.4063.
- [87] J. P. Perdew, K. Burke, and M. Ernzerhof. “Generalized Gradient Approximation Made Simple”. In: *Phys. Rev. Lett.* 77 (1996), p. 3865. DOI: 10.1103/PhysRevLett.77.3865.
- [88] J. P. Perdew, K. Burke, and Y. Wang. “Generalized gradient approximation for the exchange-correlation hole of a many-electron system”. In: *Phys. Rev. B* 54 (1996), pp. 16533–16539. DOI: 10.1103/PhysRevB.54.16533.
- [89] J. P. Perdew and K. Schmidt. “Jacob’s ladder of density functional approximations for the exchange-correlation energy”. In: *AIP Conference Proceedings* 577 (2001), pp. 1–20. DOI: 10.1063/1.1390175.
- [90] R. Pérez, J. Ortega, and F. Flores. “Surface Soft Phonon and the $\sqrt{3} \times \sqrt{3} \leftrightarrow 3 \times 3$ Phase Transition in Sn/Ge(111) and Sn/Si(111)”. In: *Phys. Rev. Lett.* 86 (2001), pp. 4891–4894. DOI: 10.1103/PhysRevLett.86.4891.

- [91] G. Profeta and E. Tosatti. “Triangular Mott-Hubbard Insulator Phases of Sn/Si(111) and Sn/Ge(111) Surfaces”. In: *Phys. Rev. Lett.* 98 (2007), p. 086401. DOI: 10.1103/PhysRevLett.98.086401.
- [92] E. I. Rashba and V. I. Sheka. “Symmetry of Energy Bands in Crystals of Wurtzite Type II. Symmetry of Bands with Spin-Orbit Interaction Included”. In: *New. J. Phys.* (1959), pp. 62–76.
- [93] X. Ren et al. “Resolution-of-identity approach to Hartree-Fock, hybrid density functionals, RPA, MP2 and GW with numeric atom-centered orbital basis functions”. In: *New Journal of Physics* 14.5 (2012), p. 053020.
- [94] X.Y. Ren et al. “Spin-orbit coupling effects on the stability of two competing structures in Pb/Si(111) and Pb/Ge(111)”. In: *Phys. Rev. B* 94 (2016), p. 075436. DOI: 10.1103/PhysRevB.94.075436.
- [95] R. Resta. “Deformation-potential theorem in metals and in dielectrics”. In: *Phys. Rev. B* 44 (1991), pp. 11035–11041. DOI: 10.1103/PhysRevB.44.11035.
- [96] L. Rettig, P. S. Kirchmann, and U. Bovensiepen. “Ultrafast dynamics of occupied quantum well states in Pb/Si(111)”. In: *New J. Phys.* 14 (2012), p. 023047. DOI: 10.1088/1367-2630/14/2/023047.
- [97] M. Richter et al. “Theory of Ultrafast Dynamics of Electron-Phonon Interactions in Two Dimensional Electron Gases: Semiconductor Quantum Wells, Surfaces and Graphene”. In: *Advances in Solid State Physics*. Springer Berlin Heidelberg, 2009, pp. 281–292. ISBN: 978-3-540-85859-1. DOI: 10.1007/978-3-540-85859-1_22.
- [98] M. Richter et al. “Two-dimensional electron gases: Theory of ultrafast dynamics of electron-phonon interactions in graphene, surfaces, and quantum wells”. In: *Journal of Applied Physics* 105 (2009), p. 122409. DOI: 10.1063/1.3117236.
- [99] S. Sakong et al. “Mode conversion and long-lived vibrational modes in lead monolayers on silicon (111) after femtosecond laser excitation: A molecular dynamics simulation”. In: *Phys. Rev. B* 88 (2013), p. 115419. DOI: 10.1103/PhysRevB.88.115419.
- [100] M. Sandhofer et al. “Unoccupied electronic structure and relaxation dynamics of Pb/Si(111)”. In: *J. Elec. Spec. Relat. Phen.* 195 (2014), pp. 278–284.
- [101] M. Schackert et al. “Local Measurement of the Eliashberg Function of Pb Islands: Enhancement of Electron-Phonon Coupling by Quantum Well States”. In: *Phys. Rev. Lett.* 114 (2015), p. 047002.
- [102] W. Schäfer and M. Wegener. “Semiconductor Optics and Transport Phenomena”. In: *Measurement Science and Technology* 13.10 (2002), p. 1652.
- [103] E. Schöll, ed. *Theory of transport properties of semiconductor nanostructures*. 1. ed. London: Chapman and Hall, 1998.
- [104] S. Schuwalow, D. Grieger, and F. Lechermann. “Realistic modeling of the electronic structure and the effect of correlations for Sn/Si(111) and Sn/Ge(111) surfaces”. In: *Phys. Rev. B* 82 (2010), p. 035116. DOI: 10.1103/PhysRevB.82.035116.
- [105] L. Seehofer et al. “Structural study of the close-packed two-dimensional phases of Pb on Ge(111) and Si(111)”. In: *Phys. Rev. B*. 51 (1995), pp. 13503–13515. DOI: 10.1103/PhysRevB.51.13503.

- [106] I. Yu. Sklyadneva et al. “Electron-phonon coupling and superconductivity in the (4/3)-monolayer of Pb on Si(111): Role of spin-orbit interaction”. In: *Phys. Rev. B.* 97 (2018), p. 195409. DOI: 10.1103/PhysRevB.97.195409.
- [107] I. Yu. Sklyadneva et al. “Mass enhancement parameter in free-standing ultrathin Pb(111) films: The effect of spin-orbit coupling”. In: *Phys. Rev. B.* 87 (2013), p. 085440. DOI: 10.1103/PhysRevB.87.085440.
- [108] P.C. Snijders and H.H. Weitering. “Colloquium: Electronic instabilities in self-assembled atom wires”. In: *Rev. Mod. Phys.* 82 (2010), pp. 307–329. DOI: 10.1103/RevModPhys.82.307.
- [109] E. Speiser et al. “Surface vibrational Raman modes of In:Si(111)(4 × 1) and (8 × 2) nanowires”. In: *Phys. Rev. B.* 94 (2016), p. 075417. DOI: 10.1103/PhysRevB.94.075417.
- [110] E. Speiser et al. “Surface vibrations in the T₄ and H₃ Pb phases on Si(111)”. In: *Phys. Rev. B.* 98 (2018), p. 195427. DOI: 10.1103/PhysRevB.98.195427.
- [111] National Bureau of Standards and American Society for Metals. *Bulletin of alloy phase diagrams*. English. Periodical; Periodical/Journal, magazine, other. Title from cover. 1980. URL: <http://www.springerlink.com/content/121062>.
- [112] S. Stepanovsky et al. “The dense $\alpha\text{-}\sqrt{3}\times\sqrt{3}$ Pb/Si(111) phase: A comprehensive STM and SPA-LEED study of ordering, phase transitions and interactions”. In: *Surface Science* 600 (2006), pp. 1417–1430. DOI: 10.1016/j.susc.2005.12.041.
- [113] R. M. Sternheimer. “Electronic Polarizabilities of Ions from the Hartree-Fock Wave Functions”. In: *Phys. Rev.* 96 (1954), pp. 951–968. DOI: 10.1103/PhysRev.96.951.
- [114] A. S. Syed et al. “Unoccupied electronic structure and momentum-dependent scattering dynamics in Pb/Si(557) nanowire arrays”. In: *Phys. Rev. B* 92 (2015), p. 134301. DOI: 10.1103/PhysRevB.92.134301.
- [115] C. Tegenkamp et al. “Fermi Nesting between Atomic Wires with Strong Spin-Orbit Coupling”. In: *Phys. Rev. Lett.* 109 (2012), p. 266401. DOI: 10.1103/PhysRevLett.109.266401.
- [116] C. Tegenkamp et al. “Switching Between One and Two Dimensions: Conductivity of Pb-Induced Chain Structures on Si(557)”. In: *Phys. Rev. Lett.* 95 (2005), p. 176804. DOI: 10.1103/PhysRevLett.95.176804.
- [117] L. H. Thomas. “The calculation of atomic fields”. In: *Math. Proc. of the Cambridge Phil. Society* 23.5 (1927), pp. 542–548. DOI: 10.1017/S0305004100011683.
- [118] A. Togo and I. Tanaka. “First principles phonon calculations in materials science”. In: *Scripta Materialia* 108 (2015), pp. 1–5. ISSN: 1359-6462. DOI: <https://doi.org/10.1016/j.scriptamat.2015.07.021>.
- [119] F. Tran and P. Blaha. “Accurate Band Gaps of Semiconductors and Insulators with a Semilocal Exchange-Correlation Potential”. In: *Phys. Rev. Lett.* 102 (2009), p. 226401. DOI: 10.1103/PhysRevLett.102.226401.
- [120] M. J. Verstraete et al. “Density functional perturbation theory with spin-orbit coupling: Phonon band structure of lead”. In: *Phys. Rev. B.* 78 (2008), p. 045119.

- [121] S. H. Vosko, L. Wilk, and M. Nusair. “Accurate spin-dependent electron liquid correlation energies for local spin density calculations: a critical analysis”. In: *Canadian Journal of Physics* 58 (1980), pp. 1200–1211. DOI: 10.1139/p80-159.
- [122] M. Švec, V. Cháb, and M.C. Tringides. “Resolving the coverage puzzle of the Pb/Si(111)-73 phase”. In: *Journal of Applied Physics* 106.5 (2009), p. 053501. DOI: 10.1063/1.3197033.
- [123] C. G. Van de Walle. “Band lineups and deformation potentials in the model-solid theory”. In: *Phys. Rev. B.* 39 (1989), pp. 1871–1883. DOI: 10.1103/PhysRevB.39.1871.
- [124] C. M. Wei and M. Y. Chou. “Theory of quantum size effects in thin Pb(111) films”. In: *Phys. Rev. B* 66 (2002), p. 233408. DOI: 10.1103/PhysRevB.66.233408.
- [125] M. Weinelt et al. “Dynamics of Exciton Formation at the Si(100) $c(4 \times 2)$ Surface”. In: *Phys. Rev. Lett.* 92 (2004), p. 126801. DOI: 10.1103/PhysRevLett.92.126801.
- [126] H. H. Weitering, D. R. Heslinga, and T. Hibma. “Structure and growth of epitaxial Pb on Si(111)”. In: *Phys. Rev. B.* 45 (1992), p. 5991.
- [127] M. Yakes et al. “Self-organization at finite temperatures of the devil’s staircase in Pb/Si(111)”. In: *Phys. Rev. B.* 69 (2004), p. 224103. DOI: 10.1103/PhysRevB.69.224103.
- [128] F. Yndurain and M. Perez-Jigato. “First Principles Calculation of Localized Surface Phonons and Electron-Phonon Interaction at Pb(111) Thin Films”. In: *Phys. Rev. Lett.* 100 (2008), p. 205501.
- [129] M. Zahedifar and P. Kratzer. “Coupling of quantum well states and phonons in thin multilayer Pb films on Si(111)”. In: *Phys. Rev. B.* 96 (2017), p. 115442. DOI: 10.1103/PhysRevB.96.115442.
- [130] N.E. Zein. “Ab initio calculations of phonon dispersion curves. Application to Nb and Mo”. In: *Physics Letters A* 161.6 (1992), pp. 526–530. ISSN: 0375-9601. DOI: [https://doi.org/10.1016/0375-9601\(92\)91086-7](https://doi.org/10.1016/0375-9601(92)91086-7).
- [131] T. Zhang et al. “Superconductivity in one atomic layer metal films grown on Si(111)”. In: *Nature Physics* 6 (Feb. 2010), pp. 104–108. DOI: 10.1038/nphys1499.
- [132] Y.F. Zhang et al. “Band Structure and Oscillatory Electron-Phonon Coupling of Pb Thin Films Determined by Atomic-Layer-Resolved Quantum-Well States”. In: *Phys. Rev. Lett.* 95 (2005), p. 096802. DOI: 10.1103/PhysRevLett.95.096802.
- [133] Z. Zhang, Q. Niu, and C.K. Shih. “Electronic Growth of Metallic Overlayers on Semiconductor Substrates”. In: *Phys. Rev. Lett.* 80 (1998), pp. 5381–5384. DOI: 10.1103/PhysRevLett.80.5381.
- [134] P. Zhou et al. “Ultrafast time resolved reflection high energy electron diffraction with tilted pump pulse fronts”. In: *EPJ Web of Conferences* 41 (2013), p. 10016. DOI: 10.1051/epjconf/20134110016.

DuEPublico

Duisburg-Essen Publications online

UNIVERSITÄT
DUISBURG
ESSEN

Offen im Denken

ub | universitäts
bibliothek

Diese Dissertation wird über DuEPublico, dem Dokumenten- und Publikationsserver der Universität Duisburg-Essen, zur Verfügung gestellt und liegt auch als Print-Version vor.

DOI: 10.17185/duepublico/70155

URN: urn:nbn:de:hbz:464-20190705-080421-3



Dieses Werk kann unter einer Creative Commons Namensnennung - Keine Bearbeitungen 4.0 Lizenz (CC BY-ND 4.0) genutzt werden.